INTEGRATED STEAM REFORMING/CATALYTIC COMBUSTION

ANNULAR MICROCHANNEL REACTOR FOR HYDROGEN PRODUCTION

A Dissertation

by

HOLLY A BUTCHER

Submitted to the Office of Graduate and Professional Studies of
Texas A&M University
in partial fulfillment of the requirements for the degree of

DOCTOR OF PHILOSOPHY

Chair of Committee,	Benjamin A. Wilhite
Committee Members,	Perla Balbuena
	Mahmoud El-Halwagi
	Andrea Strzelec
Head of Department,	M. Nazmul Karim

May 2017

Major Subject: Chemical Engineering

ABSTRACT

The overall goal of this dissertation work is the development of an annular microchannel reactor (AMR) that couples methane steam reforming and catalytic combustion of methane to produce hydrogen and/or synthesis gas achieving breakthroughs in heat transfer rates and methane reforming capacities. This is accomplished through reaction engineering design analysis and CFD models, validated by experimental data provided by our industrial collaborator, Power+Energy, Inc. The initial goal was to produce a CFD model that could verify experimental results provided by Power+Energy, Inc enabling the rapid design of an AMR prototype. Once the CFD model was verified, a manufacturable design produced higher power densities than competitive planar technology and competitive overall thermal efficiencies. The next goal was to establish that catalytic combustion of methane is a viable means of providing the heat duty necessary to sustain isothermal operation of the AMR and to match AMR heat duty profiles, established previously. Catalytic combustion of methane will supply sufficient heat flux to the AMR, but there will be axial mismatch in the heat duty profiles resulting in temperature deviations, investigated later using a coupled geometry. The next goal was to investigate the potential of an unconventional catalyst design space wherein catalyst efficiency is maintained, while thermal efficiency is increased due to the thickening of the catalyst coating. 1-D analysis show that the catalyst coating could be thicker than the catalyst efficiency "rule of thumb," while maintaining high thermal efficiencies for the methane steam reforming conditions used. For the 2-D analysis, the

AMR geometry is used and shows that the catalyst coating could be increased as much as three fold with minimal losses to catalyst efficiency while maintaining high thermal efficiencies. The final goal was to couple the models presented previously using isolated geometries, while including a finite thermally conductive wall. The objective was to show the effects of heat flux mismatch and prove that the temperature deviations seen when comparing the AMR and combustion results, will be less severe than suggested by the 1-D conduction model indicates due to multi-directional heat conduction within the volume-separating wall. Temperature deviations occurring from the heat flux mismatches still occur; however, the previous performance prediction are proven incorrect. The separated models over predict the methane capacity needed for the combustion chamber, subsequently under predicting thermal efficiency and combustion heat utilization. Additionally, the temperature deviations present allow for higher hydrogen yield than originally predicted. An asymmetric design is introduced that attempts to better match the drastic heat flux in the begging of the steam reforming reaction. This asymmetric design allows for high heat flux into the AMR tube, but generates hotspots. These hotspots are then investigated with the intent of mitigation. The objective was to add catalyst to the inner tube of the AMR, which would then act as a reactive heat sink subsequently reducing the magnitude and size of the hotspot. Nine different catalyst additions are investigated in a case study surrounding the lowest flowrate indicates that any catalyst addition will reduce the hotspot to a manageable size and temperature.

ACKNOWLEDGEMENTS

I cannot thank Dr. Benjamin Wilhite enough for all of the guidance and support during these last five years. Without his constant encouragement and suggestions this dissertation would not have been possible. Dr. Wilhite was an endless source of knowledge when I was stuck or the work did not turn out the way I expected and would always offer a different perspective.

I would also like to show my gratitude to Dr. Strzelec, Dr. El-Halwagi and Dr. Balbuena for being part of my committee. I know your time is precious and I really appreciate all of the comments and suggestions for improvement on my work.

Special thanks to John Piatt, Trent Benefield, Lauren McAlexander, and Amandeep Gupta for all of their help with completing work contained in this dissertation and other projects. Being able to mentor these students allowed me to grow as an individual and learn how to mentor students, as well as better communicate to others with various levels of expertise.

Owing to the computational nature of this work, I owe great thanks to Jeff Polasek who managed the purchasing and maintaining of a server where the bulk of this work was completed, maintained my workstation, and assisted in setting up my access to the super computing servers. I would also like to mention Ping Luo for her help with setting up batch files for the super computer.

I would be remiss in forgetting to thank previous and present memebers of Dr. Wilhite's lab group: Srikanth Panyaram, Xiaohong Cui, Elva Lugo, Haomiao Zhang,

Bhanu Kuncharam, and Daejin Kim. The day-to-day interactions with each and every one of these individuals helped shape the person and engineer I am today. It was a wonderful experience to interact and work with these great people.

I also want to thank Dr. Floudas and his students Onur Onel and Alexander Niziolek for their efforts in the collaborative work that we were able to accomplish together.

I would also like to thank Louis Muiz for assisting me with different things in the lab, Towanna Arnold for all of her help with virtually any problem I had over the years and Carol Hamilton for assisting me with travel related paperwork and purchasing.

Jonathan Raftery deserves a special thanks. From the very beginning he was there to help me in any way he could. Without his help, I would have had to take a remedial course due to my lack of transport background.

Lastly, I need to thank my family for believing in me and never letting me quit. Special thanks to my wife and my brother for their constant emotional support. Without being able to lean on them during stressful times, I'm certain this would not have been possible.

CONTRIBUTORS AND FUNDING SOURCES

This work was supervised by a dissertation committee consisting of Professors Benjamin Wilhite, Perla Balbuena, Mahmoud El-Halwagi, and M. Nazmul Karim of the Department of Chemical Engineering and Professor Andrea Strzelec of the Department of Mechanical Engineering. Portions of Section 2 of the dissertation were completed by the student in collaboration with Casey Quenzel, Luis Breziner, Jacques Mettes, and Peter Bossardd of Power and Energy, Inc. Portions of Section 3 of the dissertation were completed by the student in collaboration with John Piatt of the Department of Chemical Engineering.

This work was made possible in part by the National Science Foundation Process and Reaction Engineering Program under Grant Number 1319142. Its contents are solely the responsibility of the authors and do not necessarily represent the official views of the National Science Foundation Process and Reaction Engineering Program. This work was made possible in part Power and Energy, inc under contract N00014-11-C-0194 which was provided to Power & Energy, Inc. by the Office of Naval Research, Washington D.C., Don Hoffman, Naval Surface Warfare Center, Philadelphia, PA. Additional funding was provided by the Artie McFerrin Department of Chemical Engineering.

TABLE OF CONTENTS

Page

LIST OF FIGURES

Page

LIST OF TABLES

Page

1. INTRODUCTION*

1.1 Natural Gas as an Alternative Energy Source

Natural gas, consisting of up to 95% methane, has emerged as a promising alternative to petroleum for the production of energy, fuels and/or commodity petrochemicals [1-7]. Natural gas can be converted into industrial hydrogen or syngas, depending on the needs of the consumer, via catalytic methane steam reforming (MSR). Methane steam reforming is the reaction of CH_4 and H_2O to generate CO, CO_2 and H_2. In order to shift the ratio of CO_2 to H_2 water-gas-shift (WGS) is performed; WGS converts CO and H_2O into H_2 and CO_2[8-10]. A simplified process diagram illustrating the role of MSR in the production of hydrogen or syngas can be found in **Figure 1**.

* Part of this section is reprinted with permission from *Design of an annular microchannel reactor (AMR) for hydrogen and/or syngas production via methane steam reforming* by Butcher, H. et al., 2014.International Journal of Hydrogen Energy, 39, 18046-18057, Copyright 2014 by Hydrogen Energy Publications, LLC.

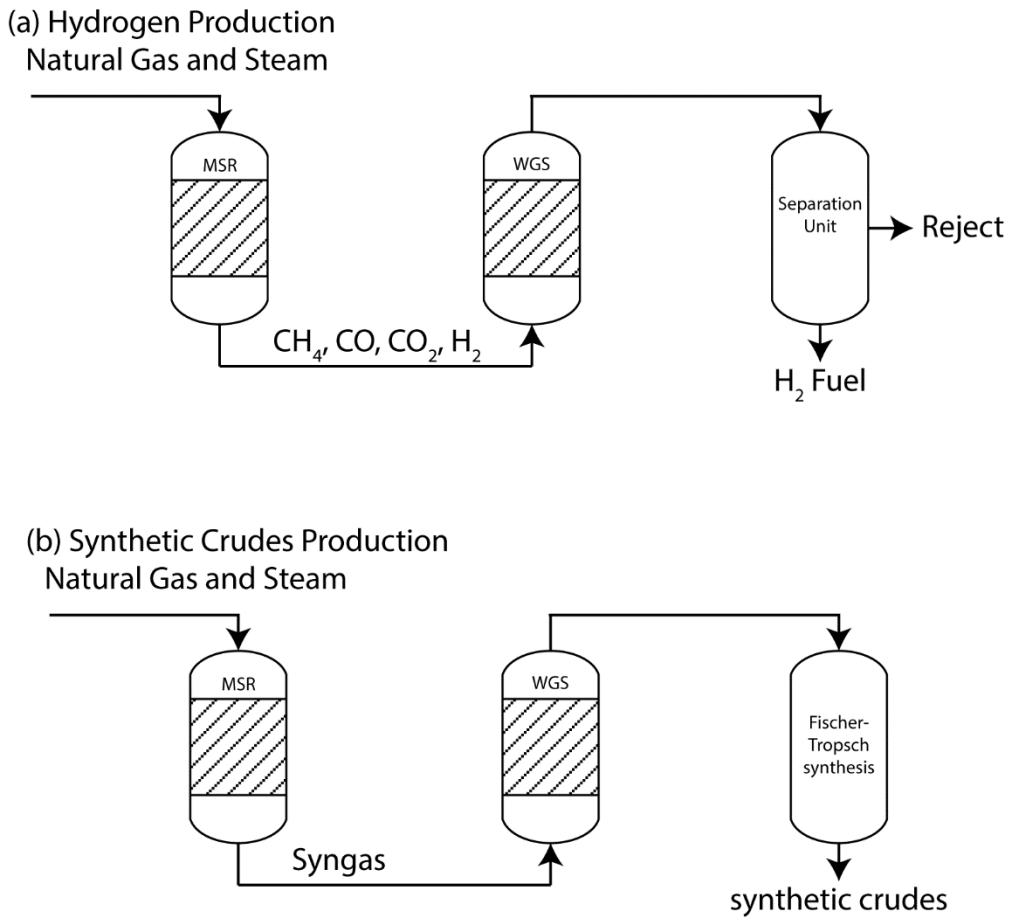

Figure 1. (a) Process diagram for the production of hydrogen through the use of a steam reformer and highly selective palladium membrane for the separation of hydrogen or pressure swing adsorption. (b) Process diagram for the production of synthetic crudes through the use of a steam reformer and Fischer-Tropsch synthesis.

Hydrogen fuel cells have become of great interest in recent years due to their zero-emission capability and high efficiencies[11-15]. Hydrogen fuel cells are a mature technology that is capable of powering a vehicle, which is why all auto manufacturers have prototypes of vehicles using this technology[16-19]. The interest in this technology has increased the demand for hydrogen that was already present in the petroleum

industry. In process (a) from **Figure 1**, hydrogen from methane steam reforming effluent gas can be separated out easily through the use of a palladium membrane[20] or pressure swing adsorption (PSA). By using a highly selective palladium membrane, hydrogen purities up to 99.999%, may be achieved,[21] sufficient for use in PEM fuel cells to power hydrogen vehicles. Thus, the production of hydrogen from natural gas or biogas[22] could be especially useful in diminishing society's dependence on gasoline[23], and reducing GHG emissions in the transportation sector. However, hydrogen currently produced in the United States is in support of oil refining or ammonia synthesis with the majority produced in California, Louisiana, and Texas via the steam reforming of natural gas[21]. The lack of an infrastructure for consumer-end distribution has limited the use of zero emission hydrogen technologies, while, the cost of building a dedicated hydrogen distribution infrastructure remains prohibited. An alternative solution is to leverage the existing natural gas infrastructure by developing a low-cost portable reactor system to interface with the existing natural gas infrastructure to produce H_2 on-site and on-demand[24, 25].

The use of stranded natural gas can enhance domestic fuel production and has the potential to reduce GHG emissions[26-29]. Currently, stranded natural gas is either ignored[30, 31] or flared[32-34] because it would be too costly to connect these small wells to existing pipeline or to liquefy[35-38] the products and ship to them a refinery. If the natural gas was processed on-site[35, 39-42] and turned into an easily transportable liquid, then this natural gas could be utilized[38]. In process (b) from **Figure 1**, the syngas produced from methane steam reforming is subsequently converted to liquids

(i.e. diesel) via Fischer-Tropsch synthesis (FTS) for the monetization of natural gas[43-48]. As before, this process requires a portable, scalable MSR reactor to convert stranded natural gas to olefins, paraffins and/or synthetic crudes [43, 44, 46, 49-52] on-site.

Both of these processes require a compact, portable, and robust MSR reactor, in contrast to existing conventional industrial steam reformer designs. These reactors would need to be standalone units, with low capital cost, and be able to handle varying capacities from day to day as well as being scalable to meet capacities of individual wells or consumers[53]. As will be discussed in Section 1.4, microreactors provide an excellent platform for meeting these challenges.

1.2 Methane Steam Reforming

Methane steam reforming is a highly endothermic process that is usually paired with water gas shift (WGS) to control the ratio of hydrogen to carbon monoxide produced. The chemical equations for MSR and WGS, along with heat of reaction, can be found in **Eqs. 1 and 2**, respectively.

$$\boldsymbol{CH_4 + H_2O \leftrightarrow CO + 3H_2 \quad \Delta H_{Rxn} = 206 \frac{kJ}{mol}} \qquad [1]$$

$$\boldsymbol{CO + H_2O \leftrightarrow H_2 + CO_2 \quad \Delta H_{Rxn} = -41 \frac{kJ}{mol}} \qquad [2]$$

Both of these reactions are reversible, such that both overall methane conversion and hydrogen yield are limited by thermodynamic equilibrium. **Figure 2** presents

equilibrium hydrogen yield and methane conversion over a temperature range of 600°C to 900°C at 11 atm with a S/C ratio of 3, which is the typical operating range of methane steam reformers[21]. These calculations were performed using a Gibbs reactor in Aspen Plus [54].

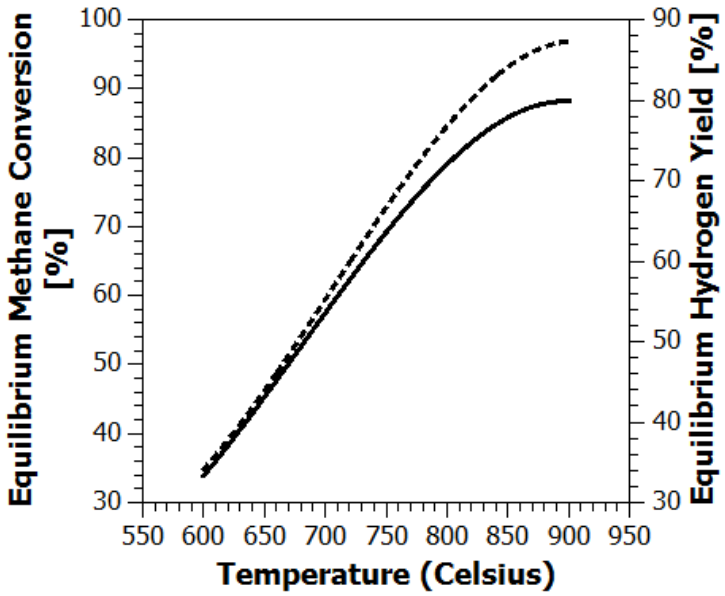

Figure 2. Temperature vs. Equilibrium Methane Conversion (dashed line) and Equilibrium Hydrogen Yield (solid line) for 600-900°C. This reaction was operated at the specified temperature, 11 atm, and S/C of 3.

As shown in **Figure 2**, H_2 yields achieved by MSR are highly sensitive to temperature, making it a critical goal to maintain a constant operating temperature throughout the length of the reactor. In light of the high heat duty of reaction, this

requires high heat transfer rates. In most cases, a portion of the natural gas is burned to supply heat for the MSR reaction[53, 55-61]. However, the challenge still remains of evenly distributing combustion to the reforming volume[11, 62-65].

1.3 Conventional Methane Steam Reformers

Conventional multi-tube packed bed methane steam reformers are operated at temperatures and pressures ranging from 700°C to 850°C and 3-25 atm, respectively[21, 66]. Reaction heat is provided by the combustion of a portion of the inlet natural gas and/or waste gases. The heat is transferred to the reactants by the combustion gas flowing over the catalyst filled pipes as shown in **Figure 3**. The reactors are typically operated at a mass steam to carbon ratio of 3:1 to minimize the risk of coke formation. After the gas passes through the reformer, it is sent to one or more shift reactors to achieve the desired H_2:CO ratio. Water-gas-shift is favorable at temperatures lower than 600°C, with H_2 yields increasing at lower temperatures. In some cases a high (350-475°C) and low (200-250°C) temperature shift reactor are used in series to achieve high conversions and low fractions of CO in the exit gas.

The hydrogen purity of off-gases in a refinery can range from 70%-99% for different processes, but generally higher hydrogen purities are needed for use in the refinery [67]. Purification is needed to reach these higher purities. Depending on the intended use of the hydrogen, it may be purified by PSA[68] or palladium membranes purities of ~95- 99.999% purity, respectively. The latter is required to remove CO to a

level below 10 ppm, the threshold tolerance of PEM or phosphoric acid fuel cells. Alternatively, preferential oxidation of CO (**Eqs. 3 and 4**) may be used to achieve sufficiently low CO levels.

$$\boldsymbol{CO + \frac{1}{2}O_2 \rightarrow CO_2} \quad [3]$$

$$\boldsymbol{CO + H_2 \rightarrow CH_4 + H_2O} \quad [4]$$

Energy conversion efficiency is an important aspect of these systems and is typically determined as the ratio of the higher heating value (HHV) of H_2 produced to the HHV of fuel supplied to the combustor. For these reactors it ranges from 75-80% and with waste heat recovery it can be as high as 85% [21]. The primary challenges to designing MSR reactors are (i) catalyst effectiveness and utilizations[69, 70], (ii) maintenance of uniform reaction temperature and (iii) preventing catalyst deactivation[71-75]. Catalyst effectiveness factors can be as low as 10^{-2}-10^{-3} for larger sized catalyst pellets owing to high rates of catalytic reaction and the endothermic nature of reaction[76, 77]. At moderate temperature, equilibrium conversion of methane is low[78-80] while high temperatures pose the risk of catalyst deactivation through sintering and coking problem[72, 76, 81-87].

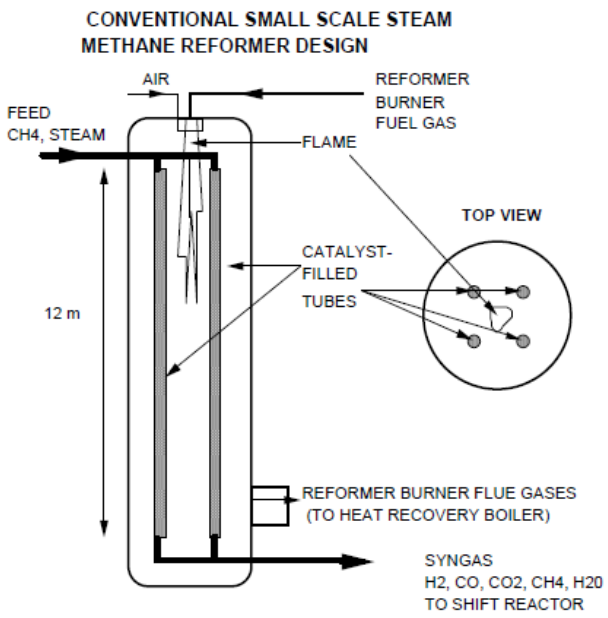

Figure 3. Schematic of a typical industrial steam reformer [21].

1.4 Microchannel Reactors

Microtechnology promises an inherently safer, more portable and efficient alternative to industrial scale reactors[88-91]. By reducing the hydraulic diameter associated with reaction volume, order-of-magnitude improvements in heat and mass transfer rates are achievable. This allows for higher chemical productivity per unit volume at greater power densities, in turn realizing a more compact and portable reactor[88, 89, 92].

1.4.1 Planar Microchannel Reactors

Current microchannel reactors consist of two-dimensional patterns machined or manufactured in individual plates providing a flat, planar reactor design[93-96]. These planar systems can be made using a variety of materials such as Si and SiO using MEMS fabrication techniques[91, 97, 98]; ceramics by the use of molds[99, 100]; and metals that can be stamped or machined [94, 95, 101-103] with the necessary reaction volumes. These planar systems start by producing the reaction volume on one plate and to scale up the reaction volume the number of plates are increased[9, 58, 101]. **Figure 4** shows this system.

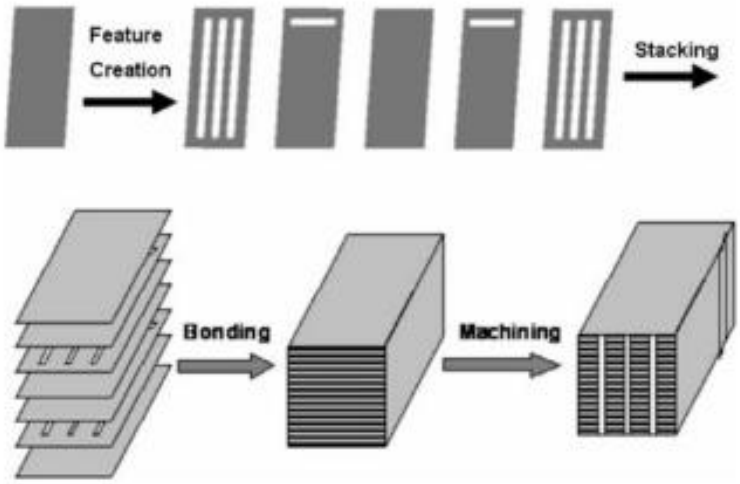

Figure 4. Manufacturing steps to produce planar microchannel reactors [101].

These stacks offer integration of endothermic and exothermic reactions by alternating plates of steam reforming and combustion [104-106], which allows for energy integration via the pairing of exothermic and endothermic reactions in close proximity. This allows for high heat transfer rates, orders of magnitude higher than conventional steam reformers [11, 107, 108]. Being able to machine or stamp these reactor plates allows for better paring of heat transfer profiles to achieve optimum performance from every plate and reaction. However these reactors are not without challenges. These reactors are built up from individual plates that have to be laminated together. With a linear scale up in size comes a linear scale up in sealing area and cost. With each individual plate having its own "bow," when stacked this "bow" accumulates until maintaining a gas-tight seal becomes impossible [90, 109-111]. Additionally, thermal "cross-talk" can happen between the plates, resulting in non-uniform temperature profiles which reduces reactor performance. The large external surface area of laminated stack provides for a direct conductive pathway for heat loss to surroundings, reducing thermal efficiency and creating significant thermal gradients through the stack[112].

1.4.2 Radial Microchannel Reactors

Recently, a theoretical study by Besser [113] illustrated the potential of radial microchannel reactor designs to mitigate the limitations of planar microchannel reactors. The use of cylindrically-symmetrical reactor units possessing axisymmetric heat flux

allows for overcoming excessive heat losses to ambient[97]. The cylindrical design intrinsically allows for a higher surface area of catalyst to fluid volume ratio than in a comparably sized planar reactor, which results in higher power densities. Power & Energy, Inc. has developed a novel manufacturing process for rapidly producing scalable arrays of annular microchannel reactors (AMR) (19-200 per unit)[114-118] that exploit the advantages of cylindrically symmetrical reactor units originally identified by Besser [113]. The heart of this technology is the use of tube-in-tube assemblies to form individual, thermally isolated AMRs (**Figure 5**) which may subsequently be arranged in parallel or series to achieve scale-up. Each AMR channel is formed by the annular gap (0.3 – 0.7mm) between a pair of co-axially aligned tubes; one end of the outer tube is welded closed such that the open end of the inner tube supplies the inlet or exit path for the fluid near the closed end of the outer tube. Manufacturing of an array of identical, parallel AMRs is achieved by laser welding inner- and outer-tubes to separate inlet manifolds (**Figure 6a,b**), such that individual tubes may freely expand to relieve thermal stresses independently of each other. This is accomplished using an in-house automated 200W continuous laser-welding system capable of achieving high-quality seals (more than 300,000 failure-free laser welds in the field since 2006) at a rate of ~3 seconds/tube. Mechanical stabilization is provided at the sealed end of the AMR via insertion through a “slip plate” which minimizes transverse deflection of individual tubes while allowing axial expansion with changing temperature. The resulting AMR design offers several unique advantages over existing planar microchannel reactors, including:

- **Reduced manufacturing costs:** By utilizing mass-produced tubular substrates and conventional (automated laser-welding) sealing technologies, dramatic reduction in cost of scale can be achieved.
- **Increased durability and scalability:** By minimizing the packaging and sealing contact area, device durability is increased by reducing the occurrence of gas leaks, seal failure; likewise, placement of seals is such that each can be inspected and repaired if necessary prior to final reactor assembly.
- **Minimized thermal stress:** By anchoring the tubes that make up the AMR at one end and allowing the other to "float," individual AMRs are capable of absorbing significant thermal gradients without the risk of failure due to thermal strain; likewise, because individual tubes are not sealed directly to each other, differential thermal expansion between the tubes does not compromise seals.
- **Improved power and system density:** By minimizing substrate volumes and the distance between the combustion heat and the reforming reactions and eliminating the direct thermal connections to other AMR channels and the containment vessel through the use of the tube-in-tube architecture, breakthroughs in system density, portability, reliability and construction costs are achieved.

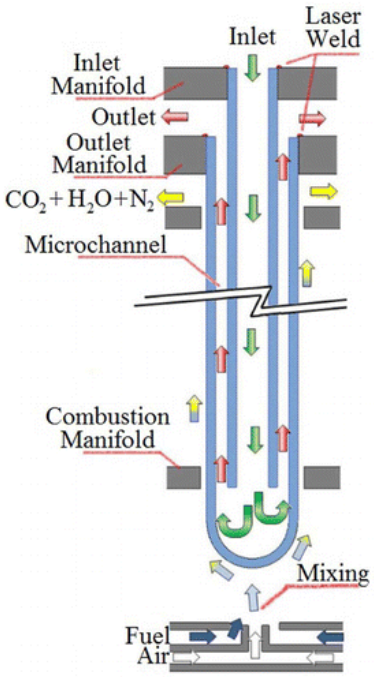

Figure 5. Schematic of a prototype radial microreactor (AMR) subsystem for syngas and hydrogen production from methane[112].

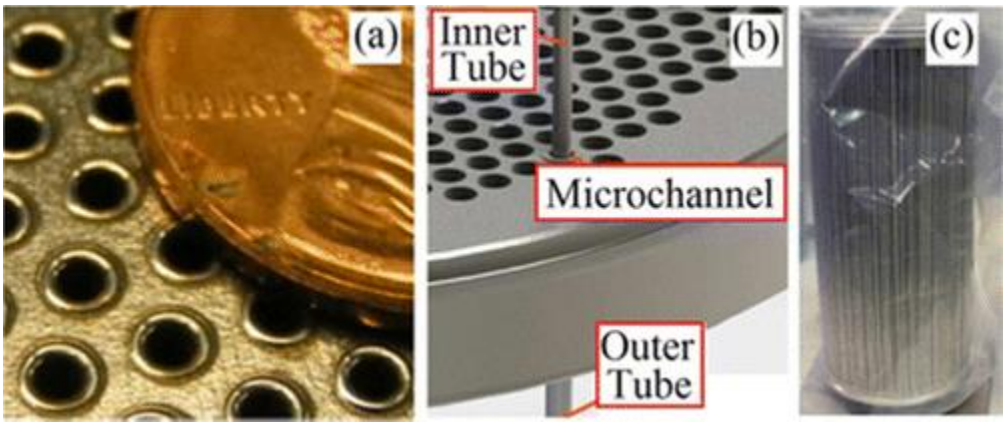

Figure 6. Manufacturing techniques developed by Power & Energy, Inc. for creating large arrays of AMRs: (a) laser welding of individual microtubes to the distributor plate, (b) alignment of the inner microtube to the outer microtube to form a radial microchannel, and (c) tube-in-tube system for hydrogen purification, consisting of 1400 individual radial microchannels capable of purifying 76 N $m^3 h^{-1}$ of H_2 [112].

This manufacturing technology has been demonstrated for creating massively scaled arrays of tube-in-tube inorganic membranes for hydrogen purification, with over 250 purifiers sold by Power & Energy, Inc. since 2007, all using the AMR design. A commercial system comprised of 1,400 parallel AMRs packaged into a 6" OD housing is shown in Figure 6c[119]. In light of the growing demand for efficient, low-cost hydrogen and syn-gas production in the energy and fuels sector, the AMR system is actively being investigated for use in methane or natural gas reforming[112].

The goal of this work is to determine how well this annular microchannel reactor works in comparison to other existing steam reforming technology, and whether this technology can meet the demands of hydrogen production for the monetization of natural gas. Currently, steam reforming and combustion of natural gas have been modeled separately, so the question of whether the independent systems will act similarly when integrated into one system still remains. In Section 2, a detailed description of the steam reforming portion of the AMR is given along with results and projections for a final design, including the heat duty profiles needed to be provided by combustion. In Section 3, a detailed description of the combustion volume is given along with the matchup of heat duty profiles from the steam reformer and combustion volumes. The results given show a temperature gradient exists along the wall of the reactor. However, the inclusion of a separating wall could act to stabilize the system thermally. Section 4 investigates the potential to increase methane reforming capacity by increasing catalyst coating thickness. A 1-D model predicts the presence of a design space outside of convention that could be used to maintain catalyst efficiency and

thermal efficiency. This design space is investigated in 2-D using the AMR reactor as a real world example. This 2-D investigation show that the optimal thickness for the AMR is ~60 microns, a 2 fold increase over the current design. Section 5 combines the steam reforming model (Section 2) and the combustion model (Section 3) into one geometry and model. This integration shows that the separated models over predict the amount of methane needed to power the steam reforming reaction and subsequently under predicts all other performance metrics. An additional geometry design is investigated; a design that asymmetrically pairs the steam reforming and combustion catalyst coatings in an attempt to meet the highly endothermic demands of the steam reforming reaction entrance. However this new geometry results in hotspot formation and is bested by the symmetrical paring of the two catalyst coatings. Section 7 attempts to reduce the hotspot formation produced when asymmetrically pairing the reforming and combustion catalyst coatings. Nine thickness and length variations are tested for their ability to reduce hotspot magnitude and size. A complete study of all nine combinations are tested for the lowest AMR flowrate of 0.25 SLPM dry basis CH_4. All combinations showed a significant change in hotspot magnitude, but diminishing returns are seen at catalyst thicknesses higher than 30 microns.

2. METHANE STEAM REFORMING*

2.1 Overview

This Section details the work performed in the design of the annular microreactor (AMR) described in Section 1.4.2. Previously, simulations have been completed to determine the best annular gap size for heat transfer efficiency[112]. These simulations concluded that a 300 micron gap was the best size in terms of heat transfer performance. Following this determination, Power+Energy produced a bench scale prototype of the device detailed in Section 2.2.1. A two-dimensional CFD model with radial symmetry was prepared to predict the results of this reactor (Section 2.2.2-2.2.6). The resulting data from the simulations using this CFD model predicted the experimental data (Section 2.2.9), so this model was used to predict the performance of a manufacturable device design (Section 2.2.10). From these simulations analysis was conducted on the possibility of coking and active metal oxidation using thermodynamic calculations. A sensitivity study was implemented (Section 2.2.11) to determine performance with varying steam to methane inlet compositions. The main objective of these simulations were to determine the performance of the device at multiple flow rates and determine the necessary heat duty to be provided by the combustion of methane in a separate volume, along with the heat duty profile required for optimum performance of the system.

*Part of this section is reprinted with permission from *Design of an annular microchannel reactor (AMR) for hydrogen and/or syngas production via methane steam reforming* by Butcher, H. et al., 2014.International Journal of Hydrogen Energy, 39, 18046-18057, Copyright 2014 by Hydrogen Energy Publications, LLC.

Analysis of the proposed 19 AMR device was initiated in Section 2.7 predicting the potential of the final device and allowing for comparison with other devices in the literature.

2.2 Steam Reformer

The novel annular (or radial) microreactor (AMR) design consists of an inner open-ended tube nested within an outer close-ended tube, such that the annular space thus formed acts as a radial (as opposed to planar) microchannel (**Figure 5**).[112] The resulting microreactor effectively combines the aforementioned advantages of microchannel reactors with those of traditional macroscale annular reactors, specifically in-situ preheating of feed and greater control over reaction temperature uniformity,[120, 121] while providing additional advantages in operation and manufacturability over existing planar designs. The AMR design presents additional advantages in manufacturability and tolerance to both pressure and thermal stresses over planar designs, as detailed elsewhere.[112] An experimental demonstration of a 0.7 mm annular width prototype AMR for steam reforming of methane at 1023K was presented in [112]. Reaction rates were measured indirectly using a combination of variable and fixed power heating bands, such that the power required to maintain isothermality was used to accurately measure heat duty of reaction; thus experimental data focused upon heat transfer rates achievable by the AMR design. Results confirmed high rates of heat transfer (up to 10 $W \cdot cm^{-2}$ catalyst surface area, or $160 W \cdot cm^{-3}$ of microchannel volume)

corresponding to competitive catalyst power densities (up to 6.7kW·cm^{-3} catalyst at ~48% of maximum hydrogen yield) at a space velocity of 543,000 h^{-1} (<7ms residence time). A two dimensional computational fluid dynamic (CFD) model of the AMR system was shown capable of predicting experimental results, and subsequently employed for investigating the impact of annular spacing upon reactor performance. New experimental data employing a second generation bench scale AMR prototype (three 31.8mm sections of catalyst with 0.3mm annular gap width) for the steam reforming of methane, with a revised bench scale apparatus enabling direct measurement of hydrogen partial pressure. This bench scale system provides a basis for validating the CFD model presented herein. Local temperature, pressure and compositional data provided by CFD simulations are employed to assess the risk of catalyst deactivation via coke formation and active metal oxidation. Results provide the necessary understanding of required heating profiles to ensure stable long-term operation of the AMR. This model is subsequently employed as a basis for a preliminary evaluation of an autothermal 10kW, 19 AMR end user device (under development by Power & Energy, Inc.).

2.2.1 Experimental

A bench-scale AMR prototype was constructed for assessing reactor performance in terms of hydrogen productivity via catalytic methane steam reforming over a range of gas flow rates (**Figure 7**). In order to facilitate isothermal experiments, the prototype

AMR was divided into three separate catalytic segments. Each segment was constructed from a 50.8mm x 30mm OD cylindrical block of FeCrAl alloy (Kanthal, Sandvik AB). A 13.3mm ID hole was machined in each block, and two evenly spaced wells were machined perpendicular to the outer surface at a depth of 7.95mm to allow placement of thermocouples at 2.37mm from the catalyst film. Introduction of a proprietary 1wt% Rh, 15wt% Ni on alumina catalyst (PN#1170) at a uniform coating thickness of 0.03mm and 31.8mm length was provided by Catacel Corp. Individual segments were connected to each other via welding. The inner tube has a 12.7mm OD (ID = 9.40mm) and was placed axially inside the larger bore. The inlet of the inner tube and outlet of the outer tube were welded to separate gas manifolds to complete the assembly. The resulting annular microchannel has a channel width of 0.303mm and is divided into three separate catalytic regions of 31.8mm length each, such that the total annular microchannel volume available for catalytic steam reforming of methane is 1170 mm^3, the total catalyst volume is 119 mm^3 and the surface area available for heat transfer to the catalyst is 19900 mm^2. These values are employed for calculating reactor space velocities from the total gas feed rate (methane and steam) at standard pressure and temperature.

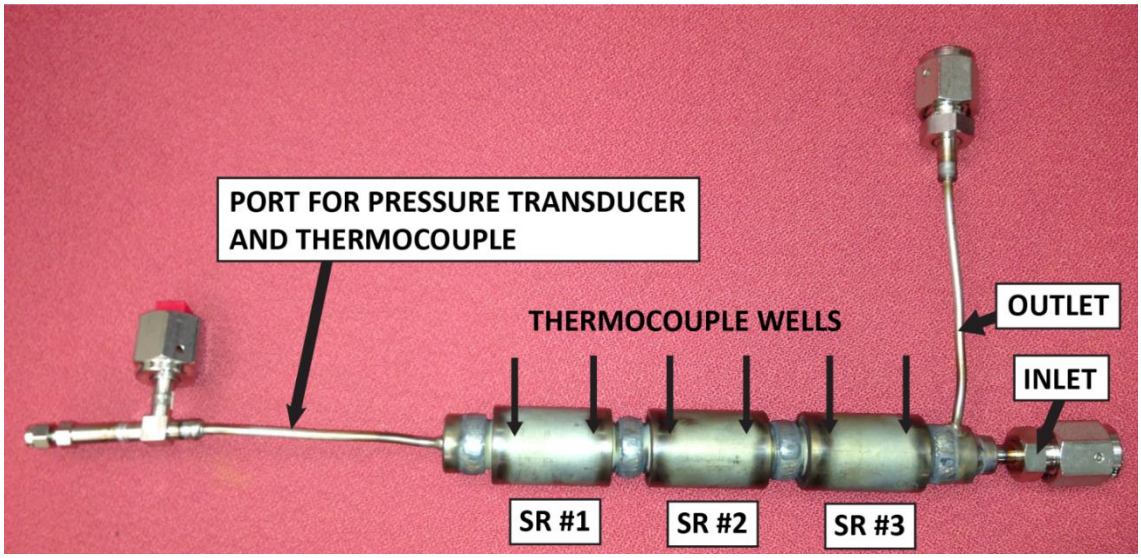

Figure 7. The bench scale AMR prototype employed in the present work. The AMR is divided into three consecutive steam reforming zones of equal length to facilitate temperature control.

Gas composition employed in all reaction studies was a 3.3:1 molar supply of steam and methane. Steam was provided by pressure displacement pumping of DI water using Ar (99.999%, Airgas) at 13.8 bar from a 4L reservoir. Uniform flow of DI water into an evaporator was maintained using a liquid mass flow controller (Bronkhorst® Liqui-FLOW® L23V12). Methane (Airgas® CP Gr 2.5) was supplied by a gas mass flow controller (Bronkhorst® EL-FLOW® F201CV) and preheated to the evaporator outlet temperature (400^{o}C) prior to mixing with steam. The resulting CH_4-H_2O mixture was then brought to the desired AMR operating temperature using a second preheater and supplied to the inner tube of the AMR assembly at the desired operating temperature of the AMR (1023K). The system was operated at 11 bar with the pressure being monitored by multiple pressure transducers (Omega® PX309-300AI) located

immediately downstream of the liquid mass controller for water, mass flow controller for methane, after the location where the steam and methane first mix, and after the final preheating section directly before the AMR. The pressure was regulated by a back pressure regulator located downstream of the dry hydrogen sensor which was controlled via pressure transducer in between the final preheating section and the AMR. Preheating of the feed gas prior to supplying the inner tube of the AMR assembly alleviates most internal preheating of the feed gas, enabling greater control of temperature uniformity within the reactor via three zone heating system, described below.

The AMR temperature was maintained using a combination of variable and fixed power heating bands (Tempco® MPP50801) placed around the three catalytic segments. Reactor wall temperature for each segment of the AMR was measured within the reactor wall via K type thermocouples (Omega® CAIN-116U-12) connected to a National Instruments® touch screen (TPC-2515) equipped with a programmable logic controller (cRIO-9075). Baseline heating rates necessary to maintain each target AMR wall temperature were determined in the absence of methane using Ar flow rates identical to those employed for subsequent reaction experiments. Power supplied to the catalytic AMR segments was varied to maintain target reactor wall temperatures under steam reforming conditions.

Effluent gas exiting the AMR bench scale prototype was cooled to 281K using a VWR 1150S chiller with water trap to remove excess moisture prior to gas analysis. Resulting dry effluent hydrogen partial pressure was measured using a hydrogen sensor designed and patented by Power & Energy, Inc. The sensor consists of a free standing,

close ended dense metallic hydrogen-permselective membrane (0.05mm thick, 23wt% Ag-Pd) nested within an outer sealed tube equipped with permeate side pressure sensor. Prior to use, the permeate chamber was heated to 653K and purged with hydrogen to reduce all other species partial pressures to < 0.07 psia. The retentate volume was then connected via mixing tee to the dry effluent stream, such that the hydrogen partial pressure in the permeate volume may equilibrate with the retentate/effluent hydrogen partial pressure. Once equilibrated, measurement of permeate absolute pressure via transducer corresponds to the retentate hydrogen partial pressure. The membrane is maintained at 380^{o}C, which corresponds to typical equilibration times of < 1s. Resulting dry basis effluent hydrogen partial pressure values were used to calculate the rate of hydrogen production as well as the overall heat duty of catalytic reaction. A schematic of the bench scale apparatus for testing the AMR prototype is presented in **Figure 8.**

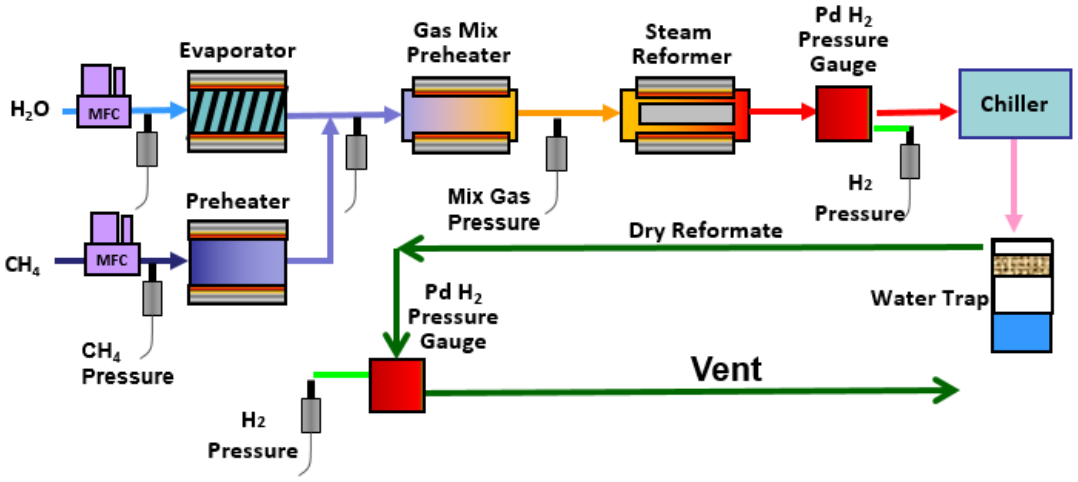

Figure 8. Schematic of the experimental apparatus employed for testing the bench-scale AMR prototype.

2.3 Theoretical Section

A two dimensional, steady state model of the bench scale annular microreactor (AMR) was developed in the COMSOL v4.2a. programming environment and subsequently validated through comparison with experimental data. The resulting model expressions were employed to simulate the final AMR design in order to identify nominal operating conditions (methane flow rates and corresponding reactor heat duties) as well as assessing the risk of catalyst deactivation via coke formation or oxidation. Model geometries for both simulations, with all relevant dimensions shown, are presented in **Figure 9**. The present CFD model differs from the model previously employed in [112] by the introduction of additional expressions dictating the temperature dependence of fluid and catalyst properties and the addition of the inner

tube solid and fluid volumes to the model geometry. Details of model expressions and assumptions are presented below.

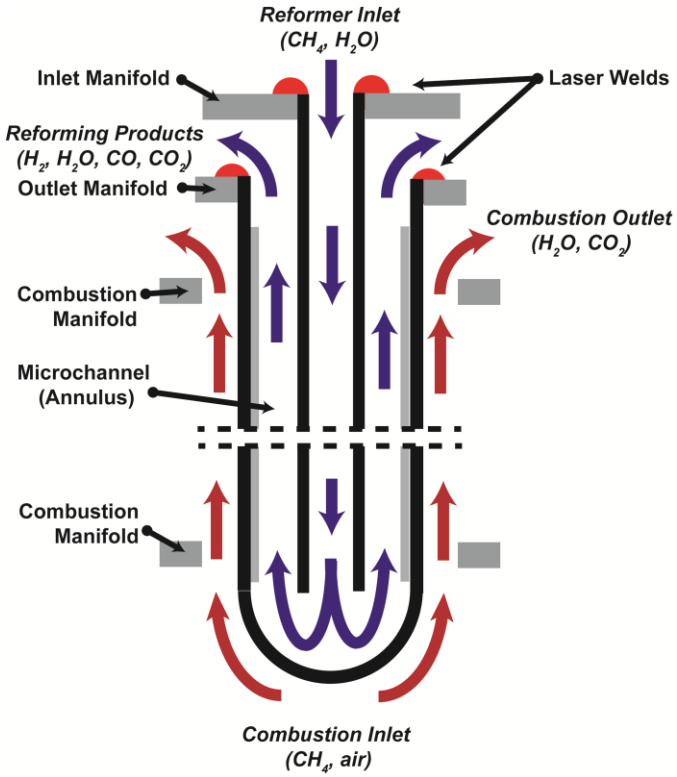

Figure 9. Schematic of the AMR design concept, highlighting annular microchannel flow path for catalytic methane steam reforming with reaction heat supplied via external combustion chamber.

2.3.1 Fluid-Phase Model Expressions

Navier-Stokes and continuity equations (**Eqs. 5, 6**) are used to model the fluid phase portion of the reactor, assuming weakly compressible flow with variable densities and viscosities calculated from using individual species mass fractions (ω_i) via ideal gas law (**Eq. 7**) and Wilke's mixing rule (**Eq. 8**), respectively. Pure component viscosities were calculated by **Eq. 9**, where T* is kT/ε with T in K and ε/k being a Lennard Jones parameter of units K, while σ_i is a Lennard Jones parameter of units Angstroms and the molecular weight is units g.mol^{-1} to obtain a viscosity in units gm.cm^{-1}.s^{-1} [122, 123]

$$\boldsymbol{\rho(u\cdot\nabla)u} =\cdot\left[\boldsymbol{-PI+\mu_{mix}(\nabla u+(\nabla u)^{T})-\frac{2}{3}\mu_{mix}(\nabla\cdot u)I}\right] \quad [5]$$

$$\boldsymbol{\nabla\cdot(\rho u)=0} \quad [6]$$

$$\boldsymbol{\rho=\frac{P}{RT}\sum_{i=1}^{N}\omega_i M_i} \quad [7]$$

$$\boldsymbol{\mu_{mix}=\sum_{i=1}^{N}\frac{x_i\mu_i}{\sum_j x_j\phi_{ij}},\quad \text{where}\quad \phi_{i,j}=\frac{1}{\sqrt{8}}\left(1+\frac{M_i}{M_j}\right)^{-\frac{1}{2}}\left[1+\left(\frac{\mu_i}{\mu_j}\right)^{\frac{1}{2}}\left(\frac{M_j}{M_i}\right)^{\frac{1}{4}}\right]^2} \quad [8]$$

$$\boldsymbol{\mu_i=2.6693\times10^{-5}\frac{\sqrt{M_i T}}{\sigma_i^{2}\,\Omega_\mu},\ \Omega_\mu=\frac{1.16145}{T^{*0.14874}}+\frac{0.52487}{\exp(0.77320T^{*})}+\frac{2.16178}{\exp(2.43787T^{*})}} \quad [9]$$

Convective and conductive heat transport within the bulk fluid was described by **Eq. 10** assuming a mass averaged heat capacity (**Eq. 11**)[124] and using a method analogous to Wilke's mixing rule to calculate the thermal conductivity from individual species thermal conductivities (**Eq. 12**). Pure species heat capacities were calculated

using a five parameter Shomate expression (**Eq. 13**) as a function of fluid temperature, while individual species thermal conductivities are calculated using the Chapman-Enskog formula (**Eq. 14**), which employs coefficients (T^*, σ_i) of identical units to **Eq. 9** to return a thermal conductivity of units $cal.cm^{-1}s^{-1}K^{-1}$.[122]

$$\rho C_{p,mix} u \cdot \nabla T = \nabla \cdot (k_{mix} \nabla T) \quad [10]$$

$$C_{p,mix} = \sum_{i=1}^{N} \omega_i C_{p,i} \quad [11]$$

$$k_{mix} = \sum_{i=1}^{N} \frac{x_i k_i}{\sum_j x_j \phi_{ij}} \quad [12]$$

$$C_{p,i} = A_i + B_i * t + C_i * t^2 + D_i * t^3 + \frac{E_i}{t}\ ,\ t = \frac{T}{1000} \quad [13]$$

$$k_i = 1.9891 \times 10^{-4} \frac{\sqrt{T/M_i}}{\sigma_i^2\, \Omega_k} \quad \Omega_k = \frac{1.16145}{T^{*0.14874}} + \frac{0.52487}{\exp(0.77320 T^*)} + \frac{2.16178}{\exp(2.43787 T^*)} \quad [14]$$

Individual species (CH_4, H_2O, CO, CO_2, H_2, N_2) mass transport was described using the Maxwell-Stefan expression for combined convection and diffusion (**Eq. 15**), with binary-pair diffusivities calculated using the method of Fuller et al. (**Eq. 16**)[125] assuming molecular diffusion volumes for CH_4, CO, CO_2, H_2O, H_2, and N_2 of 24.9, 18.9, 26.9, 2.7, 7.07, and 17.9, respectively. Lennard-Jones parameters employed in **Eqs. 9 and 14** for each species are presented in **Table 1**.

$$\nabla \left(\rho \omega_i \sum_k D_{i,k} \left(\nabla x_k + (x_k - \omega_k) \frac{\nabla P}{P} \right) \right) = \rho u \nabla \omega_i \quad [15]$$

$$\mathbf{D_{i,j}} = \frac{\mathbf{10^{-7}T^{1.75}\left(M_i^{-1}+M_j^{-1}\right)^{\frac{1}{2}}}}{\mathbf{P\left(v_i^{\frac{1}{3}}+v_j^{\frac{1}{3}}\right)^2}} \quad [16]$$

Table 1. Lennard-Jones parameters used in calculating individual species viscosities (**Eq. 7**) and thermal conductivities (**Eq. 12**).

Species	σ_i (Å)
H_2	2.915
N_2	3.667
CO	3.590
CO_2	3.996
CH_4	3.780
H_2O	3.165

2.3.2 Catalyst-Phase Model Expressions

The catalyst washcoating was assumed to be a meso-macroporous (i.e., pore diameter between 100-1000 nm) film, with a thickness of 0.030 mm, such that viscous and Knudsen diffusion contributions may be neglected. Transport of individual molecular species within the gas-filled catalyst pore structure was therefore described using a pseudo-homogeneous model consisting of Maxwell-Stefan (**Eq. 17**) and

Brinkman expressions (**Eq. 18**) to describe multicomponent convection and diffusion in the presence of catalytic reactions and pressure driven flow in porous media, respectively.

$$\nabla\left(\rho\omega_i\sum_k D_{i,k}\left(\nabla x_k+(x_k-\omega_k)\frac{\nabla P}{P}\right)\right)=\sum_{j=1}R_{i,j}+\rho u\nabla\omega_i \quad [17]$$

$$\frac{\rho}{\epsilon_p}(u\cdot\nabla)\frac{u}{\epsilon_p}=\nabla\cdot\left[-PI+\frac{\mu_{mix}}{\epsilon_p}(\nabla u+(\nabla u)^T)-\frac{2}{3}\frac{\mu_{mix}}{\epsilon_p}(\nabla\cdot u)I\right] \quad [18]$$

The fluid permeability of the catalyst film and the effective diffusivities for each binary pair within the catalyst pore structure are calculated as follows (**Eq. 19**), assuming values for pore diameter, porosity and tortuosity of 150 nm, 45%, and 2, respectively.

$$\kappa=\frac{d_p^2\epsilon_p}{32\,\tau}\quad D_{i,j}^{eff}=\frac{\epsilon_p}{\tau}D_{i,j} \quad [19]$$

Heat transport via combination of fluid-phase convection (using velocity vector obtained from Brinkman's equations, above) and both fluid and solid phase conduction, with local heat generation via catalytic reaction, is described by **Eq. 20**:

$$\nabla(-k_{cat}\nabla T)=(-\Delta H_{MSR})R_{MSR}+(-\Delta H_{WGS})R_{WGS}-\rho C_{p_{cat}}u\nabla T \quad [20]$$

The effective heat capacity within the catalyst layer (**Eq. 21**) is assumed to be an average of the local fluid mixture heat capacity (**Eq. 11**) and that of the solid catalyst assuming a constant value of 774.9 J $kg^{-1}K^{-1}$ as weighted by the void fraction of the catalyst film, ϵ_p. The effective thermal conductivity of the fluid phase (**Eq. 14**) within the catalyst film is obtained in similar fashion, assuming a thermal conductivity of the porous catalyst of 0.15 W m^{-1} K^{-1} as obtained using the correlations of Butt[126].

$$\boldsymbol{C_{p,cat} = C_{p,mix} \cdot \epsilon_p + (1 - \epsilon_p) \cdot 774.90} \quad [21]$$

The present model employs Langmuir-Hinshelwood-Hougen-Watson (LHHW) rate expressions, originally developed by Xu and Froment,[127] to describe catalytic methane steam reforming (MSR, Eq. 22) and water-gas shift (WGS, Eq. 23) reactions in the catalyst film:

$$\mathbf{CH_4 + H_2O \rightarrow CO + 3H_2} \quad [22]$$

$$\mathbf{CO + H_2O \rightarrow CO_2 + H_2} \quad [23]$$

$$\mathbf{R_{MSR}} = \frac{\left(\left(\frac{k_{MSR}}{P_{H_2}^{2.5}}\right)\left(P_{CH_4}P_{H_2O} - \left(\frac{P_{H_2}^3 P_{CO}}{K_{e,MSR}}\right)\right)\right)}{\left(\left(1 + K_{CO}P_{CO} + K_{H_2}P_{H_2} + K_{CH_4}P_{CH_4} + \left(\frac{K_{H_2O}P_{H_2O}}{P_{H_2}}\right)\right)^2\right)} \quad [24]$$

$$\mathbf{R_{WGS}} = \frac{\left(\left(\frac{k_{WGS}}{P_{H_2}}\right)\left(P_{CO}P_{H_2O} - \left(\frac{P_{H_2}P_{CO_2}}{K_{e,WGS}}\right)\right)\right)}{\left(\left(1 + K_{CO}P_{CO} + K_{H_2}P_{H_2} + K_{CH_4}P_{CH_4} + \left(\frac{K_{H_2O}P_{H_2O}}{P_{H_2}}\right)\right)^2\right)} \quad [25]$$

where temperature dependent values for rate coefficients (k_j), individual species adsorption coefficients (K_i), and reaction equilibrium coefficients (K_{ej}) are described by

$$\boldsymbol{k_j = k_{j,o} \exp\left[-\frac{E_{Aj}}{RT}\right], K_i = K_{i,o} \exp\left[\frac{\Delta H_i}{RT}\right],} \quad [26]$$

$$\boldsymbol{K_{e,MSR} = \exp\left[\frac{26830}{T} + 30.114\right], and\ K_{e,WSR} = \exp\left[\frac{4400}{T} - 4.036\right]} \quad [27]$$

As previously demonstrated by the authors, the coefficients originally provided by Xu and Froment [127] are suitable for describing MSR and WGS reactions over the presently employed Ni-based catalyst [112], with a slight increase in pre-exponential values for rate coefficients accounting for the improved activity of the proprietary catalyst supplied by Catacel. Pre-exponential values employed in the present work are summarized in **Table 2**.

Table 2. Kinetic Parameters implemented to obtain rates of MSR and WGS reactions based on values reported by Xu and Froment[127]

pre-exponential		exponential	
$k_{MSR,o}$	2.7×10^{19} mol $bar^{0.5}$ m^{-3} cat s^{-1}	$E_{A,MSR}$	240.1 kJ mol^{-1}
$k_{WGS,o}$	1.25×10^{10} mol $bar^{-1}m^{-3}$ cat s^{-1}	$E_{A,WGS}$	67.13 kJ mol^{-1}
K_{CO}	8.23×10^{-5} bar^{-1}	ΔH_{CO}	-70.7 kJ mol^{-1}
K_{CH_4}	6.65×10^{-4} bar^{-1}	ΔH_{CH_4}	-38.3 kJ mol^{-1}
K_{H_2O}	1.77×10^{5} bar^{-1}	ΔH_{H_2O}	88.7 kJ mol^{-1}
K_{H_2}	6.12×10^{-9} bar^{-1}	ΔH_{H_2}	-82.9 kJ mol^{-1}

The above kinetic model represents a simplification of the triangular reaction network reported by Xu and Froment[127] in that the reverse methanation reaction ($CH_4 + 2H_2O \leftrightarrow CO_2 + 4H_2$) was neglected, following similar studies of microchannel reformers reported in the literature.[112, 128] A comparison of relative reaction rates at the conditions simulated indicate that the rate of this third reaction is negligible in comparison to the MSR and WGS reactions at methane conversions in excess of 10%, which corresponds to the majority of the AMR length. As will be shown in the results and discussion section, this simplification had a negligible impact on the accuracy of CFD simulations in predicting experimental trends over the range of space velocities studied.

2.3.3 Reactor Wall (Solid-Phase) Expressions

Conductive heat transfer within the wall separating inlet and annular volumes of the AMR is modeled using **Eq. 28**, below.

$$\mathbf{0} = \nabla \cdot (\boldsymbol{k_{cat}} \nabla \boldsymbol{T}) \quad [28]$$

Constant temperature values for solid phase heat capacity, density, and thermal conductivity of 0.71 kJ kg^{-1} K^{-1}, 7100 kg m^{-3}, and 22 W m^{-1} K^{-1} , respectively, were provided by the supplier, AB Sandvik, for use in the model.

2.3.4 Boundary Conditions

Boundary conditions for the gas phase expressions governing momentum, mass and heat transport were defined as follows. No-slip ($\boldsymbol{u} = 0$) and zero-flux ($-\boldsymbol{n} \cdot \boldsymbol{N_i} = 0$) conditions were assumed for all uncoated wall surfaces (**Boundary I, Figure 10**). Continuity of temperature and heat flux was assumed for the inner uncoated wall surface (**Boundary II, Figure 10**), while constant temperature conditions equal to the inlet temperature (1023K) were assumed for the uncoated outer wall surface (**Boundary III, Figure 10**). Constant temperature (1023K), composition (3.3:1 H_2O:CH_4 molar ratio) and normal fluid velocity (variable) conditions were applied at the fluid inlet (**Boundary IV, Figure 10**), with the latter value reflecting the total gas flow rate supplied to the

AMR volume. Continuity is assumed across the boundary separating the homogenous gas phase volume and the pseudo-homogeneous catalyst region. No slip and zero flux conditions were applied to the catalyst coated outer wall surface (**Boundary V, Figure 10)** along with fixed temperature (1023K); the latter condition enables solution for a target heating profile along the AMR's external surface to ensure isothermal operation. Lastly, the outlet (**Boundary VI, Figure 10**) was set to an open boundary for convective heat and mass flow with a uniform pressure.

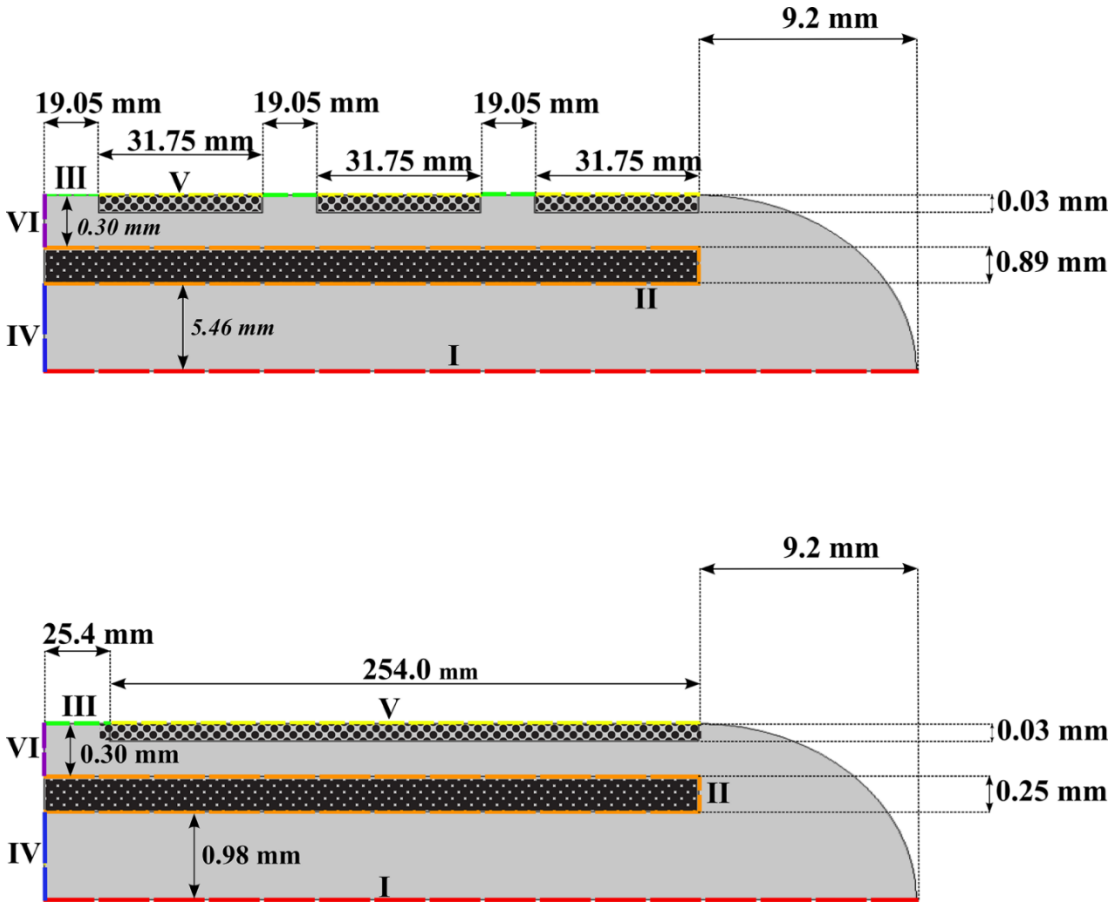

Figure 10. Geometries for 2-D COMSOL simulations, showing all relevant dimensions and boundary conditions. (a) bench scale prototype AMR (b) final AMR design. Boundary conditions are labeled as follows: (I, red) axial symmetry where r=0, (II, orange) no slip and no mass flux, (III, green) no slip, no mass flux, and fixed temperature (IV, blue) uniform velocity and constant mole fractions, (V, yellow) no slip, no mass flux, fixed temperature, (VI, purple) open boundary for convective heat and mass transport with uniform pressure.

2.4 Numerical Methods

The model described above was implemented using the commercial software COMSOL Multiphysics v4.2a equipped with the chemical engineering module. The

fluid phase and catalyst phase domains were modeled using the free and porous media, heat transfer in fluids and transport of concentrated species physics packages. The tubing domain was modeled using heat transfer in fluids physics package. The model was solved using 2D geometries as summarized in Figure 10, applied to radial symmetry space. The finite-element meshes employed were similar for both models and consisted of ~ 260,000 individual elements which corresponded to ~4,300,000 degrees of freedom. The error associated with numerical solutions was calculated from individual atomic mass balances and was found to be <1% for all simulations. Solutions were obtained using the Direct MUMPS (MUltifrontal Massively Parallel sparse direct Solver) solver, which is a multifrontal gaussian elimination method algorithm recommended for sparse matrixes[129]. All solutions were performed on a Dell PowerEdge R820 with eight (8) Intel Xeon CPU E5-4650 at 2.7 GHz and equipped with 256 GB of RAM. The typical solution times for both systems ranged from 400-8000 s.

2.5 Analysis of Simulation Results

Results of each simulation were analyzed by integrating individual mass species fluxes at the inlet and the outlet of the AMR and the heat flux into the catalyst film from the underlying support wall. The first model geometry (**Figure 10a**) was used to predict the total heat duty to the experimental AMR system, and in turn validate the accuracy of the model expressions. The second model geometry (**Figure 10b**) was used to predict the axial heat duty profile, local temperature, pressure and composition within the

catalyst film, and outlet composition for the proposed final design. The total power input was calculated using a surface integral of the total energy flux over the outer wall of the catalyst (Boundary V shown in **Figure 10**). Molar outflows of each species were calculated from individual species' molar fluxes integrated across the inlet and outlet surface.

The efficiency of the AMR was determined by normalizing the predicted hydrogen yield by the theoretical maximum hydrogen yield, assuming reaction proceeds to thermodynamic equilibrium at 1023K. A maximum hydrogen yield of 66.7% (corresponding to 75.6% methane conversion and 32.2% carbon monoxide yield) was calculated using a Gibb's reactor model [54] implemented in Aspen Plus v8.2 equipped with the NIST Standard Reference Database 103b: NIST Thermodata Engine Version 7.1. These values likewise correspond to a theoretical maximum reaction heat duty of 154 $kJ \cdot mol^{-1}$ methane fed.

2.5.1 Experiments and Comparison with CFD Simulations

Experiments were performed using a bench scale, three zone AMR prototype to confirm previous model predictions[112] and to demonstrate the validity of the CFD model presented above. Steady state outlet dry basis hydrogen mole fractions were measured at reaction temperatures of 1023K for dry basis methane feeds ranging from 0.333 to 1.75 SLPM, corresponding to reactor space velocities of 73,400 to 330,700 h^{-1}. Steam to methane molar composition was maintained at 3.3:1 for all experiments.

Figure 11 presents a comparison of measured outlet dry basis hydrogen mole fraction with CFD predictions (using reactor geometry shown in **Figure 10a**). For all experiments, hydrogen outlet composition remained relatively constant and within +/- 1.6% of calculated equilibrium dry basis composition (72.5%). This in turn allowed estimation of the reaction heat duty from ASPEN Gibbs reactor analysis (discussed above) for comparison with CFD predictions of overall heat duty of the bench scale AMR prototype. Experimental data is found to be in good agreement with CFD predictions, and is in agreement with predicted trends reported in our earlier study.[112] For example, at a space velocity of 330,700 h^{-1} (corresponding to a methane feed rate of 1.5 SLPM), a total reaction heat duty of 165W was calculated from an observed hydrogen production of 2.36 $x10^{-3}$ $mol{\cdot}s^{-1}$, which compares favorably with predicted heat duty of 162W. These values correspond to an observed volumetric heat flux of 141 $W{\cdot}cm^{-3}$ of annular reaction volume, or 1380$W{\cdot}cm^{-3}$ catalyst. The validated CFD model was subsequently employed to predict the performance of a final AMR design (geometry shown in **Figure 10b**).

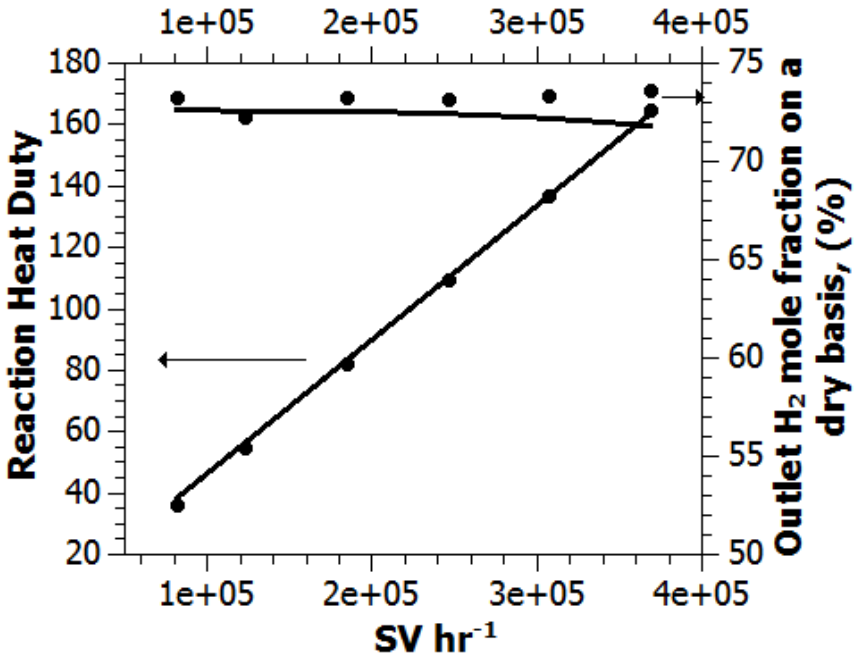

Figure 11. Comparison of experimental results and design simulation for outlet dry-basis hydrogen mole fraction and reaction heat duty vs. space velocity (SV). Experimental data is denoted by symbol while the CFD simulated results denoted by solid line.

The experimentally observed power density of 1380W.cm^{-3} catalyst, reported for a space velocity of 330,700 hr^{-1}, compares favorably with literature values obtained with laboratory-scale packed beds of fine catalyst powders operated at equivalent space velocities.[130, 131] . Zhai *et al*.,[130] reported methane conversions corresponding to estimated power densities of 60 – 470 W/cm^3 over Ni/La-Ca/Al_2O_3 and $Ni_{0.5}Mg_{2.5}AlO_9$ catalysts operated at 1173K with 3:1 steam:methane feed, corresponding to space velocities of 120,000 – 1,200,000 hr^{-1}. Takehira *et al*.[131] reported reforming rates at space velocities of 110,000 – 580,000 hr^{-1} over a Ni-based Mg-Al clay catalyst using 2:1

H_2O:CH_4 feed at 1073K which correspond to an estimated power density of ~560W.cm^{-3} catalyst. The higher catalyst-basis power densities observed for the AMR can be attributed to our use of undiluted methane feeds, in contrast to 50% diluted feeds employed in laboratory-scale packed bed studies. The AMR system employs catalyst length scales (.03mm catalyst coatings) which are comparable to these laboratory packed-bed experiments (< 0.1mm powders), which in both cases removes fluid-phase heat and mass transport limitations to enable operation at space velocities in excess of 100,000 hr^{-1}.

2.5.2 Simulations of Final AMR Design

The above CFD model expressions were employed using the final AMR design geometry (**Figure 10b**) in order to predict the overall reactor heat duty, hydrogen yield, hydrogen production and effluent dry-basis compositions vs. space velocity for this proposed manufacturing design. Results (presented in **Figure 12**) enable identification of a suitable operating window of methane capacities for the AMR as follows. A minimum practical space velocity of 195,000 h^{-1} (corresponding to a dry basis methane supply of 0.5 SLPM) is identified, corresponding to a methane capacity below which hydrogen yield remains > 99% of the theoretical maximum. A maximum space velocity of 782,000 h^{-1} is identified based upon a desired 4:1 turn down ratio; at space velocities beyond this value, predicted hydrogen yields drop significantly to values < 75%. Between these two limits, a nominal space velocity of 391,000h^{-1} (dry basis methane supply of 1 SLPM) is

identified, which corresponds to hydrogen yields and molar production rates of 62.8% and $1.89x10^{-3}$ $mol \cdot s^{-1}$ with a total heat duty of 108.6W. Given an annular reaction volume of $0.66cm^3$, heat transfer surface area of $24.4cm^2$ and total catalyst volume of $72.4mm^3$, this nominal space velocity corresponds to predicted heat fluxes of 165 $W \cdot cm^{-3}$, 4.45 $W \cdot cm^{-2}$ and 1500 $W \cdot cm^{-3}$ on a fluid volumetric, heat transfer surface area and catalyst volumetric basis, respectively. Hydrogen yields, heat duties, heat flux values and effluent compositions predicted for the final AMR device design operating at these three space velocities (195,000, 391,000 and 782,000hr^{-1}) are summarized in **Table 3**.

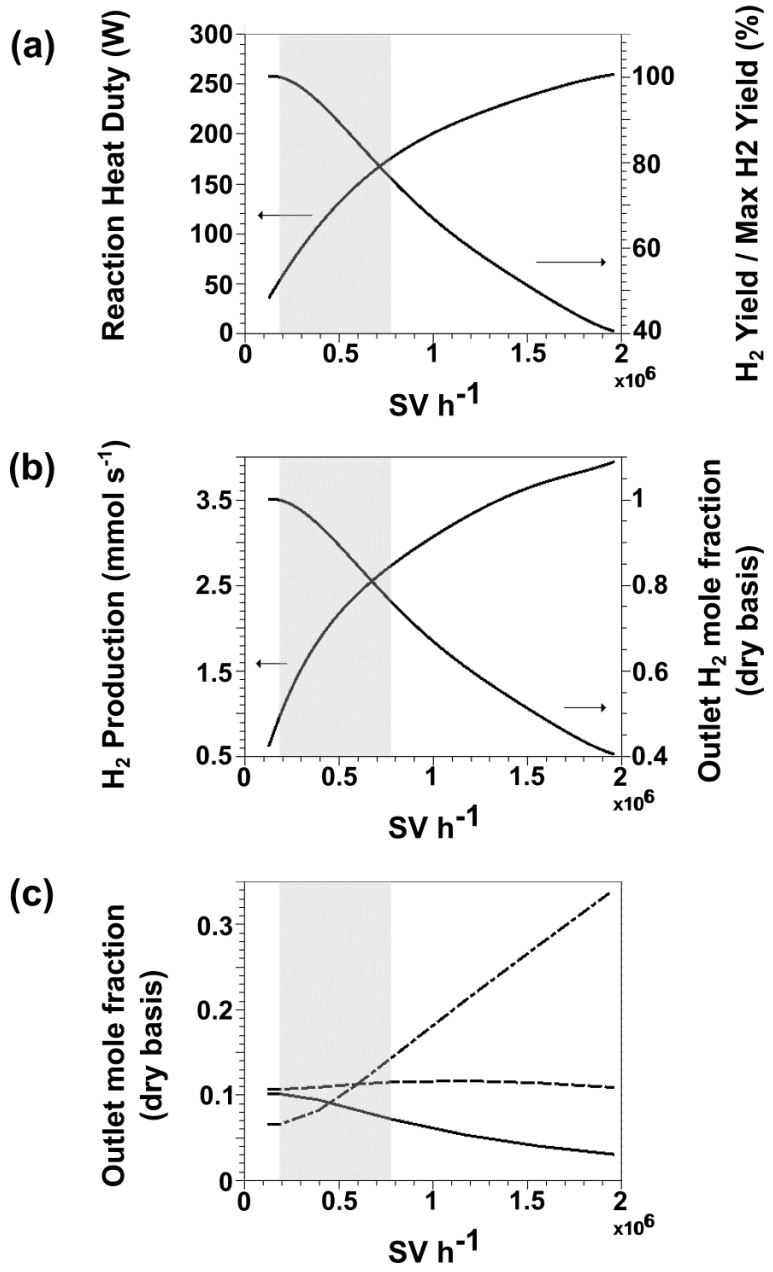

Figure 12. Results for final design simulations for flow rates ranging from 0.333 to 5 SLPM. The nominal flowrate window of 0.5 to 2 SLPM is highlighted on each plot: (a) reaction heat duty and hydrogen yield/maximum hydrogen yield, (b) hydrogen production and outlet hydrogen mole fraction dry basis, and (c) outlet mole fractions for CO (line), CO_2 (dashed line) and CH_4 (dot dashed line).

Table 3. Mole fractions at the outlet of the reactor for minimum, maximum and nominal space velocities. The inlet mole fractions for all flowrates were 0.001, 0.764, 0.001, 0.001, 0.232, and 0.001 for CO, H_2O, H_2, CO_2, CH_4, and N_2, respectively.

Space Velocity	**195000 h^{-1}**	**391000 h^{-1}**	**782000 h^{-1}**
Methane Capacity (dry basis)	**0.5 SLPM**	**1 SLPM**	**2 SLPM**
x_{CO}	0.0638	0.0581	0.0402
x_{H_2O}	0.3698	0.3847	0.4397
x_{H_2}	0.4565	0.4388	0.3741
x_{CO_2}	0.0674	0.0672	0.0646
x_{CH_4}	0.0419	0.0504	0.0807
x_{N_2}	0.0007	0.0007	0.0008
Reaction Heat Duty (W)	55.8	108.6	176.1
Hydrogen Yield /Max Hydrogen Yield (%)	99.8	85.2	76.0
Heat Flux (fluid volume basis) (W/cm^3)	84.5	164.5	266.8
Heat Flux (heat transfer surface area basis) (kW/m^2)	22.9	44.5	72.2
Heat Flux (catalyst volume basis) (kW/cm^3)	0.771	1F.500	2.432

Catalyst-basis energy densities predicted from simulations and experiments are competitive with literature values for ceramic and metallic planar microreactor systems. Murphy et al.[100] recently reported a ceramic-plate heat-exchanger microreactor for MSR with 0.025mm thick catalyst coating of Rh-Al_2O_3/CeO_2; their experimental device contained 20 parallel reforming channels of dimensions 3.144mm x 0.740mm x 70mm and was operated at a nominal temperature of 1023K with a 2.5:1 H_2O:CH_4 feed diluted

in 50% N_2. For a space time of 45,000 hr^{-1}, CH_4 conversions of > 99% equilibrium value were reported, from which a catalyst power density of ~1.6kW/cm^3 catalyst may be estimated (assuming a catalyst density of ~1.5 g.cm^{-3}). Lerou et al.[28] reported results obtained for a prototype metal-plate heat-exchanger microchannel for combustion-driven methane steam reforming developed by Velocys, Inc. For a methane supply rate of 9.96 SLPM at a 2.5:1 CH_4:H_2O feed ratio at an overall gas flow rate of 25.1 SLPM, a methane conversion of 88.5% and CO selectivity of 72% was reported, corresponding to approximately 580kW of reforming heat duty; given a reported surface heat flux for the SMR of 14 W/cm^2, the total reforming catalyst surface area may be estimated at 42,000cm^2. While the catalyst wash-coat thickness was not reported, an assumed thickness of .030mm (consistent with values reported in similar microchannel reformers[100, 112]) would correspond to an estimated catalyst power density of 4.6 kW/cm^3 catalyst at the reported residence time of 9ms, or space velocity of 400,000hr^{-1}. Thus, a comparison of the presently reported catalyst power densities and corresponding space velocities for the experimental AMR apparatus and simulations of the AMR prototype (1380W/cm^3 at 330,700hr^{-1} and 1500W/cm^3 at 391,000hr^{-1}, respectively) are comparable to estimated values from literature reports for metallic and ceramic planar heat-exchanger microreactors (4600W/cm^3 at 400,000hr^{-1} and 1600W/cm^3 at 45,000hr^{-1}). As noted in the Introduction, the AMR system is expected to provide additional advantages in ease of manufacture and durability over planar microreactor architectures; the present discussion confirms that these benefits come at equivalent reactor space times and catalyst power densities.

Local temperature, pressure and compositional data predicted for the minimum, maximum and nominal space velocities discussed above were further analyzed to assess the potential risk of catalyst deactivation owing to coke formation and/or oxidation of the active Ni metal species. Local atomic ratios of O:C and H:C were calculated at all mesh points (approx. 12,250) calculated within the catalyst domain for each of the three space velocities of interest, with all values consistently found to be > 3.2:1 and 9.2:1, respectively. Previous analysis by Probstien[132] for the methane steam reforming system indicates that under these conditions, coke formation is not thermodynamically favorable. The risk of catalyst deactivation via Ni oxidation was also assessed using CFD results obtained at the minimum, maximum and nominal space velocities identified. Local temperature, pressure and composition within the catalyst were employed to calculate the Gibbs free energy associated with the Ni oxidation by steam and carbon monoxide.

$$\boldsymbol{Ni + CO_2 \rightleftharpoons NiO + CO} \quad [29]$$

$$\boldsymbol{Ni + H_2O \rightleftharpoons NiO + H_2} \quad [30]$$

Substitution into the corresponding equilibrium conditions (below) allows calculation of the local H_2O:H_2 and CO_2:CO ratios necessary for Ni oxidation to become thermodynamically favorable; on average, minimum ratios of 545:1 and 710:1 were calculated from simulation results.

$$\boldsymbol{G(T,P) = RT\ \ln(\frac{P_{H_2}}{P_{H_2O}})} \quad [31]$$

$$\boldsymbol{G(T,P) = RT\ \ln(\frac{P_{CO}}{P_{CO_2}})} \quad [32]$$

A comparison of all local minimum compositional values with predicted local H_2O:H_2 and CO_2:CO ratios indicates that oxidation of the active catalyst metal is not favorable under the range of proposed operating conditions. Thus, simulations suggest that long-term catalyst deactivation due to oxidation and/or coke formation should be negligible under nominal operating conditions. Lastly, axial heat duty profiles for all three cases are presented in **Figure 13**. Heat duty profiles were found to follow a simple exponential decay style profile, with overall heat duties of 55.8, 108.6 and 176.1 W, respectively. This information allows identification of optimal combustor designs, including catalyst loading profiles and materials selection for proper manipulation of axial heat conduction within the combustion chamber, which is presently underway.

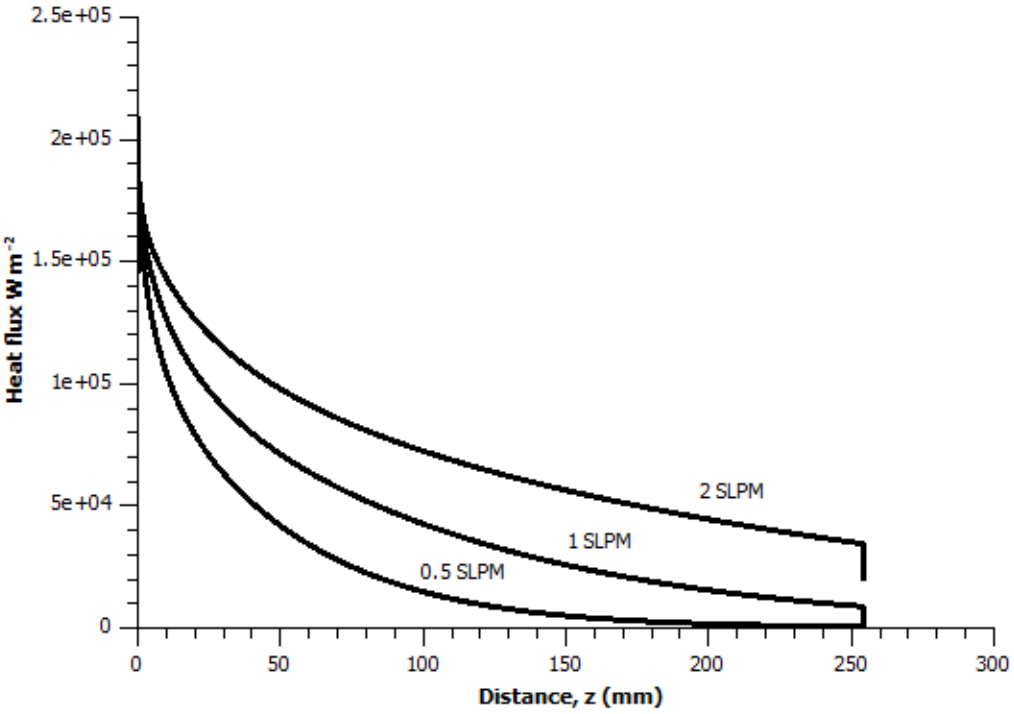

Figure 13. Axial heat duty profiles required by final AMR design for maintaining isothermal operation for minimum, nominal and maximum recommended capacities (0.5, 1, 2 SLPM).

Simulation results allow estimation of the AMR steam reformer thermal efficiency, based upon the lower heating values (LHV) of methane and hydrogen **(Table 4**). For a single-AMR feed of 0.5 SLPM dry-basis methane (0.000370 $mol \cdot s^{-1}$ methane, with latent heat of 297W), the AMR produces 1.32 SLPM of hydrogen (.00098 $mol \cdot s^{-1}$ with a latent heat of 237W) at a heat duty of 55.8W, corresponding to a latent heat of 280.2W for a thermal efficiency of 67.2%. Operation at a feed of 1 SLPM dry-basis methane, the AMR produces 2.54 SLPM hydrogen (0.00189 $mol \cdot s^{-1}$) at a heat duty of 108.6W for a thermal efficiency of 64.1%. Lastly, for a maximum recommended feed of

2 SLPM dry-basis methane, the AMR produces 4.27SLPM of hydrogen at a heat duty of 176.1W for a minimum thermal efficiency of 45.6%.

Table 4 Flowrates of methane in and hydrogen out with thermodynamic efficiency calculations for one AMR tube inside the nominal operation window.

Space Velocity	**195000 h^{-1}**	**391000 h^{-1}**	**782000 h^{-1}**
Flowrates			
Methane in (dry basis)	0.5 SLPM	1 SLPM	2 SLPM
Hydrogen out (dry basis)	1.32 SLPM	2.54 SLPM	4.27 SLPM
Methane Molar Flowrate in	0.000370 mol s^{-1}	0.000753 mol s^{-1}	0.001590 mol s^{-1}
Hydrogen Molar Flowrate out	0.000985 mol s^{-1}	0.00189 mol s^{-1}	0.00274 mol s^{-1}
Thermodynamic Calculations			
Latent heat in (methane)	297W	605W	1277 W
Reaction Heat Duty	55.8 W	108.6 W	176.1W
Latent heat out (hydrogen)	237 W	457 W	663 W
Thermal Efficiency	67.2 %	64.1 %	45.6 %

2.6 Inlet Steam to Methane Ratio Sensitivity

When temperature is held constant (750°C), different molar ratios of steam to carbon give different thermodynamic equilibrium methane conversions as shown in **Figure 14**. Under different circumstances, the availability of water may vary, so an evaluation of a range of molar steam to carbon ratios gives a guideline of how the

reactor would perform under various possible conditions. This study also allows for optimization of the system either globally or locally with different constraints.

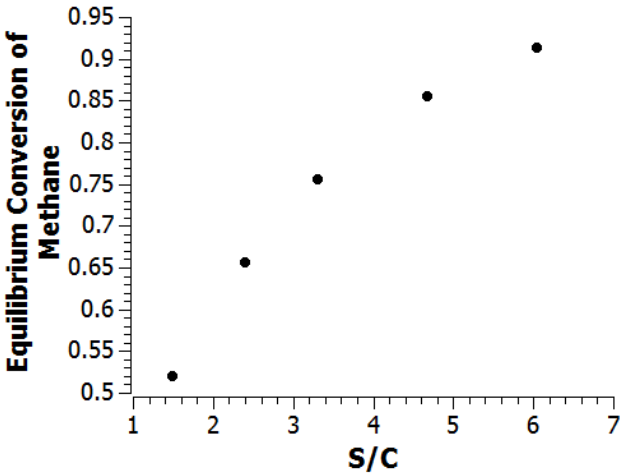

Figure 14. Equilibrium conversion of methane vs. inlet steam to carbon ratio at 11 atm and 750°C.

All of the conditions are the same as in the prototyped device, except for the inlet mole fractions. The inlet mole fractions were changed according to the target molar ratio. Each ratio was tested for a set of residence times. The percent of equilibrium conversion reached decreased with increasing space velocity as seen in **Figure 15**

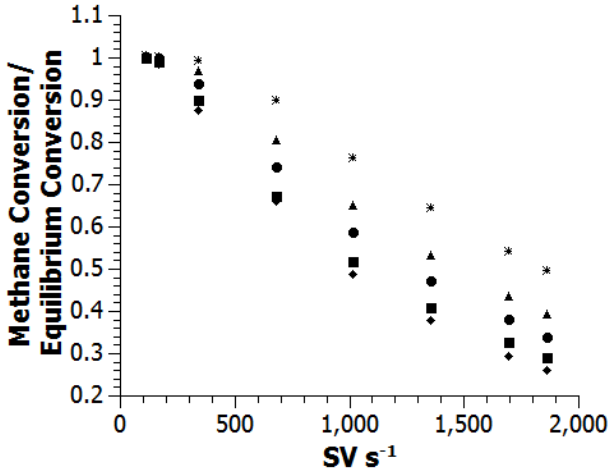

Figure 15. Percent equilibrium conversion reached vs. space velocity for different inlet S/C where 1.5 S/C (stars), 2.4 S/C (triangles), 3.3 S/C (circles), 4.65 S/C (squares), and 6 S/C (diamonds).

The rapid decrease in percent equilibrium conversion with increase in S/C is thought to be due to the methane competing with steam for active sites on the catalyst resulting in a negative order in water [133]. It is common to use a S/C ratio around 3 to reduce the risk of coking which become greater with decreasing S/C ratio [21, 76] This sensitivity shows that there would be an optimum steam to carbon ratio and flow rate to get the maximum performance out of the reactor.

2.7 Initial Assessment of 10kW, 19-AMR Reformer Concept

Based upon the above experimental and simulation results, an end-user 10kW reformer design containing 19 parallel AMRs (geometry equal to that shown in Figure

10**b**) was assembled to obtain initial estimates of system size. Simulation results were employed to provide estimates of final design performance and to identify design targets for the combustion chamber. The resulting reformer design (presented in **Figure 16**) consists of separate distribution chambers for reformer inlet (L1, **Figure 16**) and outlet (L2, **Figure 16**) as well as separate air (L6, **Figure 16**) and methane (L7, **Figure 16**) inlets for achieving stable diffusion flame (L5, **Figure 16**), with subsequent heat exchange between hot combustion gas and the array of 19 parallel AMRs (L4, **Figure 16**). Insertion of a thermally conductive porous matrix within the heat-transfer chamber (L4, **Figure 16**) allows for even axial distribution of combustion heat between individual AMRs. The resulting device has a total volume of 360cm^3, assuming a center-to-center AMR spacing of 5.71mm (based upon existing manufacturing processes at Power & Energy, Inc.) and a combustion chamber height of 15.3mm distance between air inlets and AMRs. Given a nominal rate of hydrogen production per AMR of 2.54 SLPM (at methane feed rate of 1 SLPM per AMR), an energy density of 28.5W.cm^{-3} is estimated.

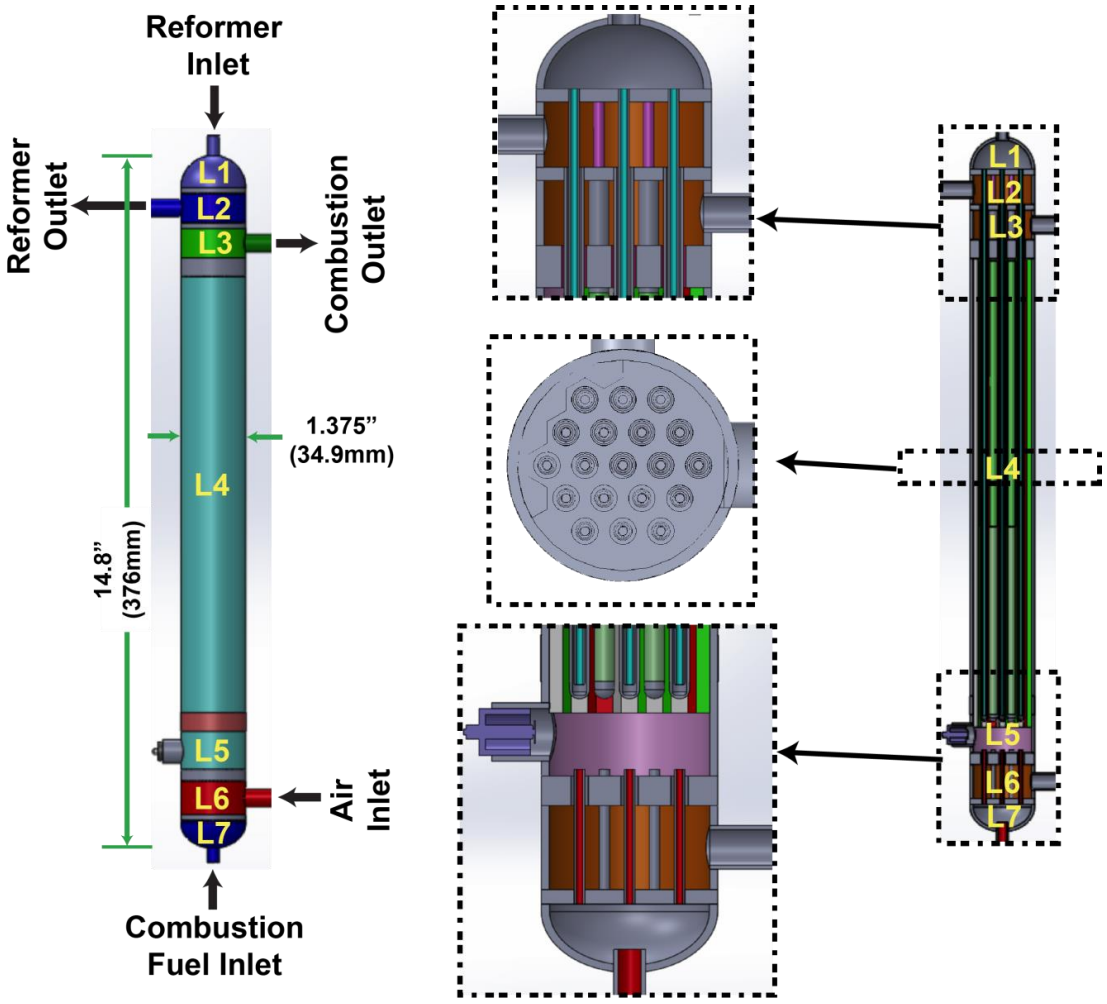

Figure 16. Schematic of 19-AMR autothermal reformer design, highlighting seven unique functional zones. (L1) Reformer inlet chamber, including distribution manifold for affixing individual outer AMR tubes; (L2) Reformer outlet chamber, including second distribution manifold for affixing individual inner, or nested, AMR tubes; (L3) Collection chamber and outlet for spent combustion gas; (L4) chamber containing AMR array, with open space allowing heat exchange between individual AMRs and combustion gas; (L5) homogeneous combustion chamber equipped with spark ignitor; (L6) combustion air inlet chamber with distributor plate; (L7) combustion methane inlet chamber with distributor plate.

Previously reported heat-exchanger microreactor designs have demonstrated combustion heat utilization efficiencies ranging from 40% to 75%;[11, 134] based upon

these literature values, a conservative estimate of 50% combustion heat utilization was assumed for the purpose of providing an initial appraisal of the envisioned 10kW (19 AMR) autothermal reformer shown in Figure 16. Thus, for the target nominal methane feed rate of 1 SLPM per AMR, the total reforming methane capacity of 19 SLPM requires 2,063W of heat provided by 6.24 SLPM of methane supplied to the combustion chamber for an overall thermal efficiency of 61.5%, or a hydrogen yield of 95.6% (on a per-methane basis). Work is currently underway to assess the achievable heat utilization for multiple combustor volume designs, as is process flowsheet analyses to optimize overall system efficiency accounting for balance-of-plant components.

2.8 Conclusions

The present experimental work demonstrated a second-generation bench-scale AMR prototype with an annular microchannel width of 0.3mm and a total catalyst length of 85.8mm capable of catalyst utilizations upwards of 1540W reaction heat per cm^3 of catalyst at >98% of equilibrium hydrogen yields at 11bar and 1023K. Experimental data validated the accuracy of a two-dimensional steady-state computational fluid dynamic model of the AMR prototype, implemented in the COMSOL v4.2a programming environment. CFD simulations of a final AMR manufacturing design identified a nominal methane capacity of 1 SLPM methane per microchannel, with an upper recommended capacity of 2 SLPM (corresponding 75% of maximum theoretical hydrogen yield) and a lower recommended capacity of 0.5 SLPM (corresponding to

>99% of maximum theoretical hydrogen yield). Thermal efficiencies, defined using methane and product hydrogen lower heating values (LHVs), of 67.2-45.6% were obtained from simulations over this range of methane capacities. Analysis of local composition, temperature and pressure indicate that for all flowrates, catalyst deactivation via coke formation or Nickel oxidation is not thermodynamically favored. The inlet S/C ratio sensitivity study concluded that there would be an optimum inlet steam to methane ratio depending on available water sources. Based upon these single AMR simulations, a 10kW autothermal reformer design was developed for combining 19 parallel AMRs within a single methane-air combustion chamber. An initial analysis of this reformer concept suggested achievable energy densities of >28kW.cm^{-3}, corresponding to overall methane capacities of 12.7 – 48.1 SLPM and hydrogen production rates of 25.1 – 81.1 SLPM. In addition to demonstrating the potential of the AMR technology for modular, small-scale hydrogen production from natural gas, this preliminary analysis provides the necessary basis for subsequent detailed design of combustion chamber discussed in Section 3.

3. COMBUSTION

In order to provide the heat duties shown in Figure 13 for MSR, the catalytic combustion of methane will be performed around each AMR tube, so CFD simulations were carried out to find the necessary flow rates corresponding to the heat duties of the nominal operating window for the AMR. CFD simulations of methane-air catalytic combustion over the outer surface of a washcoated AMR were performed in order to confirm the potential for catalytic combustion to (i) provide required reforming heat duties via catalytic reaction, and (ii) match ideal isothermal reforming heat duty axial profiles such that near-isothermal AMR axial temperature profiles may be expected. Our findings confirm that AMR designs are capable of providing overall autothermal hydrogen production from methane via coupled steam reforming and catalytic combustion over a single-AMR methane capacity of 0.25 – 1.0 SLPM on dry-gas basis.

This section details efforts to construct, validate and employ 2-D CFD models of the AMR combustion chamber for assessing the viability of catalytic combustion for driving endothermic methane steam reforming. Two-dimensional CFD models describing catalytic combustion and fluid-phase transport in the AMR combustor volume were developed and employed to facilitate rapid simulations and to facilitate subsequent integration with 2-D CFD models describing the interior (reforming volume) of the AMR. The use of 2-D CFD models to approximate the close hexagonal packing structure of the actual AMR network was validated through comparison of non-reacting

heat transfer models employing the actual 3-D architecture and a 2-D approximation thereof.

3.1 Model Development

A steady state two dimensional model of the combustion volume was developed using COMSOL Multiphysics v4.2a to identify the correct volumetric flowrates necessary to produce the previously identified heat duty profiles to facilitate methane steam reforming in the annular microchannel reactor (AMR) system. The combustion volume consists of the outer volume surrounding individual AMR tubes, assumed to be ordered into a close-packed hexagonal pattern with an actual center-to-center spacing of individual AMR tubes of 4.85 mm (**Figure 17a**). For the purpose of reducing computational costs, this three-dimensional combustion volume is described using a two-dimensional approximate volume (**Figure 17b**) with tube center-to-center spacing chosen to ensure identical ratios of flow volume to heat transfer surface area (characteristic transport length) between the two models. Details of governing equations and model geometries are provided below.

3.1.1 Fluid Volume Expressions

The fluid volume was modeled using Navier Stokes for weakly compressible fluids and the continuity equation (**Eqs. 33,34**). Density was calculated using the local

individual species mass fractions using the ideal gas law (**Eq. 35**). The mixture viscosity is approximated using the pure component viscosity of Nitrogen using the Lennard Jones parameters fit model (**Eq. 36**).

$$\boldsymbol{\rho(u\cdot\nabla)u} =\cdot \left[\boldsymbol{-PI+\mu_{mix}(\nabla u+(\nabla u)^{T})-\frac{2}{3}\mu_{mix}(\nabla\cdot u)I}\right] \quad [33]$$

$$\boldsymbol{\nabla\cdot(\rho u)=0} \quad [34]$$

$$\boldsymbol{\rho=\frac{P}{RT}\sum_{i=1}^{N}\omega_i M_i} \quad [35]$$

$$\boldsymbol{\mu_i=2.6693\times10^{-5}\frac{\sqrt{M_iT}}{\sigma_i^{2}\,\Omega_\mu},\ \Omega_\mu=\frac{1.16145}{T^{*0.14874}}+\frac{0.52487}{\exp(0.77320T^{*})}+\frac{2.16178}{\exp(2.43787T^{*})}} \quad [36]$$

Heat transfer within the bulk fluid was modeled using convection and conduction described by **Eq. 37**. The mixture heat capacity was modeled using a mass fraction weighted sum of the individual species heat capacities (**Eq. 38**), which was calculated using the five parameter Shomate equation (**Eq. 39**). The thermal conductivity for the mixture was calculated using Wilke's mixing rule (**Eq. 40**), and the individual species thermal conductivities were calculated using the Chapman-Enskog formula. Lennard-Jones parameters for **Eqs 36 and 41** can be found in **Table 5**.

$$\boldsymbol{\rho C_{p,mix}u\cdot\nabla T=\nabla\cdot(k_{mix}\nabla T)} \quad [37]$$

$$\boldsymbol{C_{p,mix}=\sum_{i=1}^{N}\omega_i C_{p,i}} \quad [38]$$

$$\boldsymbol{k_{mix}=\sum_{i=1}^{N}\frac{x_i k_i}{\sum_j x_j\phi_{ij}}} \quad [39]$$

$$C_{p,i} = A_i + B_i * t + C_i * t^2 + D_i * t^3 + \frac{E_i}{t}\ ,\ t = \frac{T}{1000} \quad [40]$$

$$\mathbf{k_i} = \mathbf{1.9891 \times 10^{-4}}\ \frac{\sqrt{\mathbf{T/M_i}}}{\mathbf{\sigma_i^2\ \Omega_k}} \quad \mathbf{\Omega_k} = \frac{\mathbf{1.16145}}{\mathbf{T^{*0.14874}}} + \frac{\mathbf{0.52487}}{\mathbf{\exp(0.77320T^*)}} + \frac{\mathbf{2.16178}}{\mathbf{\exp(2.43787T^*)}} \quad [41]$$

Table 5. Lennard-Jones parameters used in calculating individual species viscosities (**Eq. 36**) and thermal conductivities (**Eq.41**).

Species	σ_i (Å)
O_2	3.433
N_2	3.667
CO_2	3.996
CH_4	3.780
H_2O	3.165

Mass transport was modeled using a combination of convection and diffusion as defined by Maxwell-Stefan expression (**Eq. 42**). The binary diffusivities were calculated using the method given by Fuller et al. (**Eq.43**) assuming molecular diffusion volumes for CH_4, CO_2,O_2, H_2O, and N_2 of 24.42, 12.7, 16.6, 26.9, and 17.9, respectively.

$$\nabla\left(\rho\omega_i \sum_k D_{i,k}\left(\nabla x_k + (x_k - \omega_k)\frac{\nabla P}{P}\right)\right) = \rho u \nabla \omega_i \quad [42]$$

$$D_{i,j} = \frac{10^{-7} T^{1.75}\left(M_i^{-1} + M_j^{-1}\right)^{\frac{1}{2}}}{P\left(v_i^{\frac{1}{3}} + v_j^{\frac{1}{3}}\right)^2} \quad [43]$$

3.1.2 Catalyst-Phase Model Expressions

The catalyst coating is assumed to have a thickness of 0.03 mm in all simulations describing catalytic combustion in the combustion chamber. Individual molecular species transport within the catalyst pores are described by Maxwell-Stefan (**Eq. 44**) and Brinkkman expressions (**Eq. 45**) in order to describe multipcomponent convection and diffusion in the presence of a catalytic reaction and pressure driven flow in porous media, respectively.

$$\nabla\left(\rho\omega_i\sum_k D_{i,k}\left(\nabla x_k+(x_k-\omega_k)\frac{\nabla P}{P}\right)\right)=\sum_{j=1}R_{i,j}+\rho u\nabla\omega_i \quad [44]$$

$$\frac{\rho}{\epsilon_p}(u\cdot\nabla)\frac{u}{\epsilon_p}=\nabla\cdot\left[-PI+\frac{\mu_{mix}}{\epsilon_p}(\nabla u+(\nabla u)^T)-\frac{2}{3}\frac{\mu_{mix}}{\epsilon_p}(\nabla\cdot u)I\right] \quad [45]$$

The permeability of fluid into the catalyst film and effective diffusivities for each binary pair within the catalyst pore structure (**Eq. 46**) are calculated assuming values for pore diameter, porosity, and tortuosity of 10 nm, 45%, and 2, respectively.

$$\kappa=\frac{d_p^2\epsilon_p}{32\,\tau}\quad D_{i,j}^{eff}=\frac{\epsilon_p}{\tau}D_{i,j} \quad [46]$$

Heat transport was characterized using a combination of fluid-phase convection, fluid phase conduction, and heat generation due to catalyst reaction is described in **Eq.47**.

$$\nabla(-k_{cat}\nabla T) = (-\Delta H_{CCM})R_{CCM} - \rho C_{p_{cat}} u\nabla T \quad [47]$$

The heat capacity and thermal conductivity of the catalyst was approximated by that of the fluid phase at local conditions. The present model employs a rate expression developed by Deshmukh and Vlachos[135] to describe catalytic combustion of methane (CCM).

$$r_{CCM} = \frac{\Gamma^2 \cdot k_{CH_4}^{ads} \cdot [CH_4]}{\left(1 + \sqrt{\frac{k_{O_2}^{ads} \cdot [O_2]}{k_{O_2}^{des}}}\right)^2} \quad [48]$$

where temperature dependent modified Arrhenius rate constants can be described by **Eqs. 49 and 50**.

$$k_i^{des} = A e^{\frac{-E_a^{des}}{RT}} \left(\frac{T}{T_{ref}}\right)^{\beta^{des}} \quad [49]$$

$$k_i^{ads} = \frac{s \cdot P_{tot} e^{\frac{-E_a^{ads}}{RT}}}{\Gamma\sqrt{2\pi MRT}} \left(\frac{T}{T_{ref}}\right)^{\beta^{ads}} \quad [50]$$

where the oxygen surface coverage, θ_O, can be described by **Eq. 51**. The activation energy of desorption of oxygen and the activation energy of methane can be found in **Eqs. 52 and 53**, respectively.

$$\boldsymbol{\theta_O} = \frac{\sqrt{k_{O_2}^{ads} X_{O_2} / k_{O_2}^{des}}}{1+\sqrt{k_{O_2}^{ads} X_{O_2} / k_{O_2}^{des}}} \quad [51]$$

$$\mathbf{E_a^{des}} = \mathbf{52.8 - 2.3 \cdot \left(\frac{T}{300}\right) - 32.0 * \theta_O} \quad [52]$$

$$\mathbf{E_a^{ads}} = \mathbf{7.3 + 1.9 * \left(\frac{T}{300}\right)} \quad [53]$$

All other variables for **Eqs. 51-53** can be found in **Table 6**. In the above equations, s, represents a sticking coefficient (dimensionless) describing chemisorption of species, P_{tot} is the total pressure, β is a temperature exponent obtained from reduction of the microkinetic model, E_a is the activation energy for desorption or adsorption, and Γ is the number of catalytic metal sites per cm^2 of catalytic metal surface area.

Table 6. Kinetic parameters used for kinetic model.

Parameter	Value
$\beta_{O_2}^{des}$	-0.796
$\beta_{O_2}^{ads}$	0.766
$\beta_{CH_4}^{ads}$	0.154
Γ	2E-5
s_{O_2}	0.0542
s_{CH_4}	0.116
$A_{O_2}^{des}$	8.41E12 (1/s)

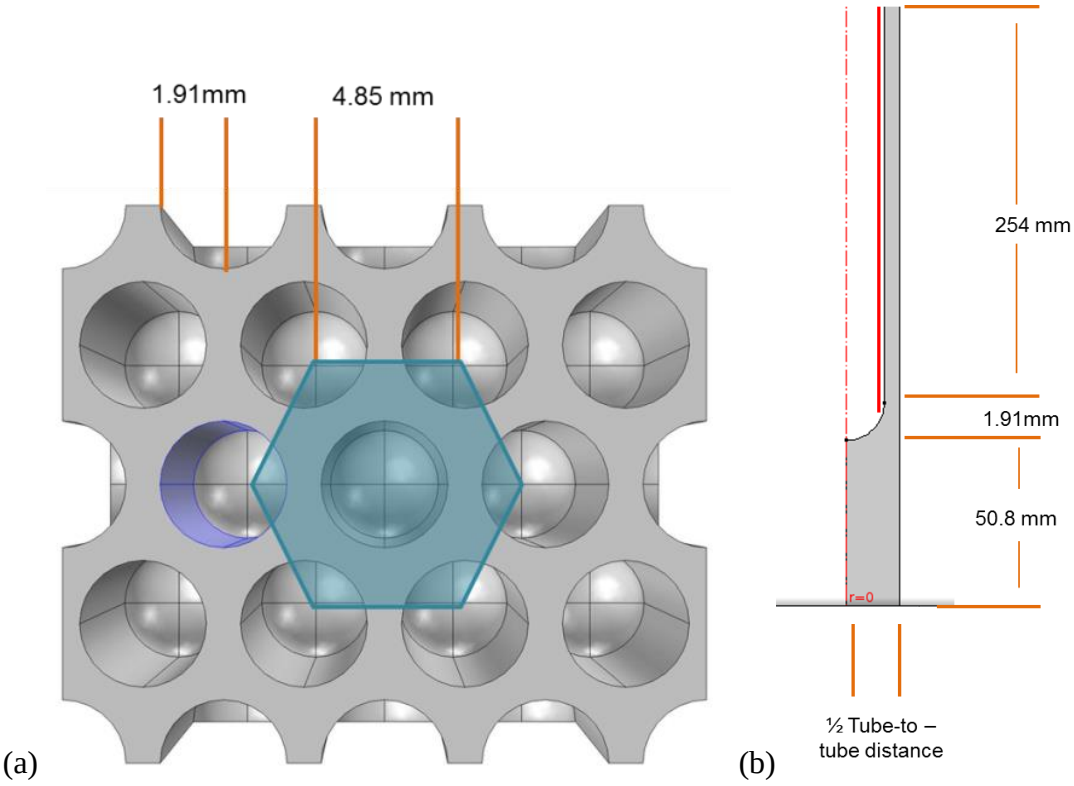

Figure 17. CFD geometries employed for combustion and heat transfer simulations; (a) 3-D geometry of AMR system; (b) 2-D approximate geometry of AMR system.

3.2 Geometry Verification

2D Model Geometry. The 2D axisymmetric geometry was constructed as follows: 1.91mm tube radius, 254mm cylinder depth, and 50.8mm free-flow area beneath the tubes. Total heat flow, q [W], for a given inlet velocity, V_{in} [m/s], was determined by taking the line integral of the radial heat flux [W/m^2] along the tube boundary (**red, Figure 17b**).

$$\boldsymbol{q = q' * 2r\pi} \quad [54]$$

The tube-to-tube length for the 2-D model is calculated such that characteristic transport length (defined as the total fluid volume divided by the available heat transfer surface area) is identical to that of the 3-D model. By equating this ratio for the actual 3-D architecture (**Figure 17a**) and for the 2-D approximation (**Figure 17b**), the following expression is obtained for calculating the tube-to-tube spacing in mm:

$$\mathbf{L_C = \frac{\sqrt{3}a^2h - 2r^2\pi}{2r\pi h} - 2r = 5.304\ mm} \quad [55]$$

where a is the actual center-to-center tube spacing in the hexagonal packing (4.85mm), r is the radius of the outer tube comprising a single AMR (1.91mm), h is the height of the AMR (254mm) and L_C is the characteristic transport length (or center-to-center tube spacing) for the 2-D approximation.

The 3D model's geometry was based on AMR specifications and includes a hexagonal pattern, 4.85mm tube-to-tube length, 1.91mm tube radius, 254mm cylinder depth, and 50.8mm free-flow area beneath the tubes. Total heat flow, q [W], for a given inlet velocity, V_{in} [m/s], was determined by taking the surface integral of the normalized heat flux [W/m^2] around the tube boundary (purple, **Figure 17a**).

3.2.1 Comparison of 3D and 2D Geometries Under Non-reacting Flow

Prior to reactive-flow simulations of the catalytic combustion volume, the accuracy of employing a 2D approximate geometry was validated by comparing heat transfer rates between a hot gas and cold AMR outer wall using both geometries over an appropriate range of gas superficial velocities. For both non-reacting flow heat transfer models, the AMR wall temperature was fixed at 800K while the inlet gas temperature was fixed at 1023K. Constant-pressure heat capacity and density for air, increased by a factor of five to magnify any differences between results obtained from each geometry, were used. The heat flows for both models were calculated, and their results compared for inlet velocities ranging from 1-4.5 m/s in 0.5 m/s increments. The previously determined 5.3mm tube-to-tube length was used in the simulations for the 2D model. The average percent error is 2.13%. Results are summarized in Table 7, below.

Table 7. Heat flow comparison of 2-D and 3-D model for different velocities.

vin [m/s]	q 2D [W]	q 3D [W]	% Difference
1.0	73.5	70.4	4.5
1.5	93.6	92.8	1.0
2.0	108.1	109.5	1.2
2.5	119.5	122.3	2.2
3.0	129.0	132.5	2.6
3.5	137.2	140.3	2.2
4.0	144.5	147.2	1.8
4.5	151.1	153.2	1.4

3.2.2 2D Simulations of AMR Combustion Volume

Simulations of methane and air mixtures undergoing catalytic combustion by a 30 micron-thick catalyst coating covering the outer surface of the AMR were performed using the 2D geometry described above with a uniform AMR center-to-center spacing of 5.304 mm, AMR length of 254mm and an initial inlet height of 48.9 mm between combustion volume inlet and the rounded tip of the AMR. This schematic of the model can be found in Figure 18. This model was used to find the methane capacity needed to match the heat duties from the previously done steam reforming analysis.

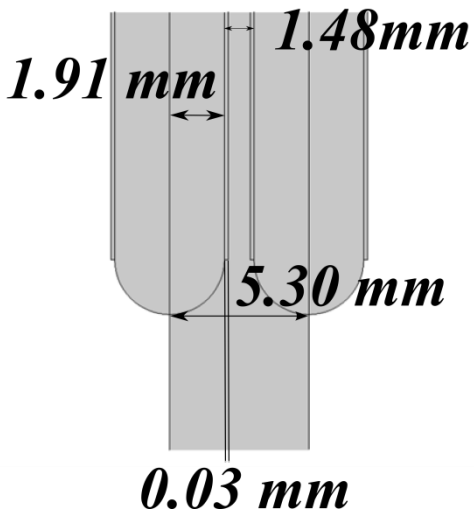

Figure 18. 2-D geometry used to model combustion.

Previous simulations of the reforming volume[136] identified the reforming heat duty required from the combustion volume for each AMR reforming capacity (given in terms of dry-basis methane flowrate, SLPM). For each required heat duty, 2D combustion volume simulations were performed to identify the corresponding combustion dry-basis methane feed rate capable of providing the requisite heat to the reformer volume. Results of separate reforming and combustion volumes at matched heat duties are summarized in **Table 8**, below.

Table 8 Results for combustion velocities that matched AMR heat duties at different flow rates.

Reforming Capacity (SLPM CH_4)	Combustion Capacity (SLPM CH_4)	heat duty (W)	Combustion Heat Utilization
0.25	0.052	28.8	90.8%
0.33	0.082	38.4	76.5%
0.50	0.126	57.8	74.3%
0.75	0.235	85.7	58.5%
1.00	0.251	110.9	70.7%

Table 8, shows the heat duties associated with the AMR flowrates and flowrates to the combustion chamber. All of the heat productions were matched within 2% of the necessary heat duty for the AMR flowrates. This resulted in a ratio of around one fourth of the methane needed for combustion as used in the AMR. This is the result of the high combustion heat utilization, which was calculated from the heat flux from combustion to

reforming volume divided by the maximum possible heat generation by catalytic combustion (i.e., at 100% conversion):

$$\textbf{Heat Utilization}_{\textbf{combustion}} = \frac{\oiint(\mathbf{q}\cdot\mathbf{n})\mathbf{ds}}{\mathbf{F}_{\mathbf{CH_4},\mathbf{i}_{\mathbf{CM}}} * \Delta\mathbf{H}_{\mathbf{CM}}} \quad [56]$$

In addition to the above combustion heat utilization, the overall thermal efficiency of the combined reforming and combustion AMR volumes is calculated following **Eq. 57**:

$$\boldsymbol{\eta}_{\mathbf{T}} = \frac{\mathbf{F}_{\mathbf{H_2},\mathbf{e}_{\mathbf{MSR}}} * \mathbf{LHV}_{\mathbf{H_2}}}{(\mathbf{F}_{\mathbf{CH_4},\mathbf{i}_{\mathbf{MSR}}} + \mathbf{F}_{\mathbf{CH_4},\mathbf{i}_{\mathbf{CM}}}) * \mathbf{LHV}_{\mathbf{CH_4}}} \mathbf{x}\ \mathbf{100}\% \quad [57]$$

Values employed for determining the thermal efficiency of the combined reforming and combustion AMR volumes are summarized in **Table 9** for each reformer dry-basis methane feed rate investigated. The local (axial) heat duty profiles for each pair of reforming and combustion flowrates summarized in **Tables 9** are compared in **Figures 19-23**.

Table 9. Flowrates of methane to the combustor and AMR and flowrates of hydrogen out of the AMR.

Reformer Capacity (SLPM CH_4)	Reforming Capacity (CH_4 mmol/s)	Combustion Capacity (CH_4 mmol/s)	Reforming Outlet (H_2 mmol/s)	Overall Thermal Efficiency	mol H_2 generated, per mol CH_4 supplied
0.25	0.185	0.040	0.495	66.5%	2.21
0.33	0.247	0.063	0.661	64.3%	2.14
0.50	0.373	0.097	0.994	63.8%	2.12
0.75	0.563	0.183	1.48	59.9%	1.99
1.00	0.756	0.199	1.92	60.8%	2.02

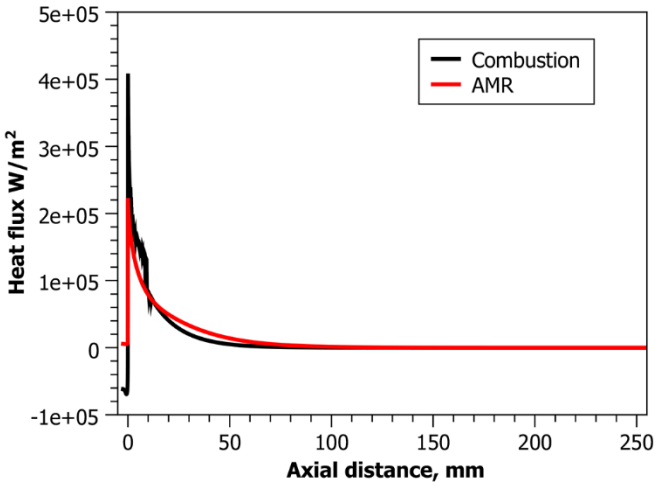

Figure 19. Heat duty profiles for total heat duty of 28.8 W corresponding to combustion capacity of 0.052 SLPM CH_4 (black) and reforming capacity of 0.25 SLPM CH_4 (red) and overall thermal efficiency of 66.5%.

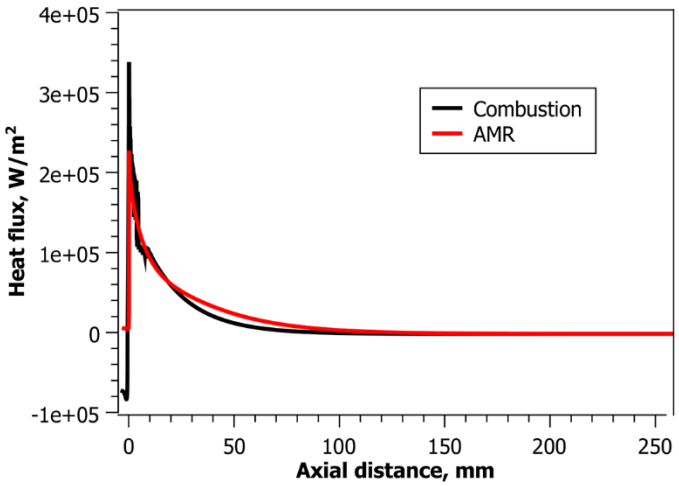

Figure 20. Heat duty profiles for total heat duty of 38.4 W, corresponding to combustion capacity of 0.082 SLPM CH_4 (black) and reforming capacity of 0.333 SLPM CH_4 (red) and overall thermal efficiency of 64.3%.

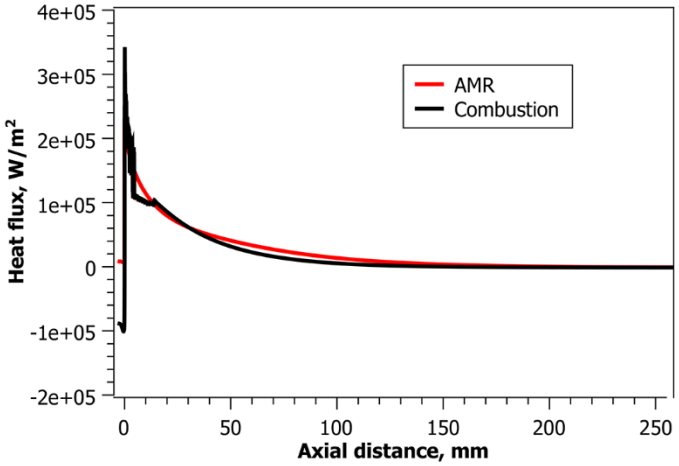

Figure 21. Heat duty profiles for total heat duty of 57.8 W, corresponding to combustion capacity of 0.126 SLPM CH_4 (black) and reforming capacity of 0.5 SLPM CH_4 (red) and overall thermal efficiency of 64%.

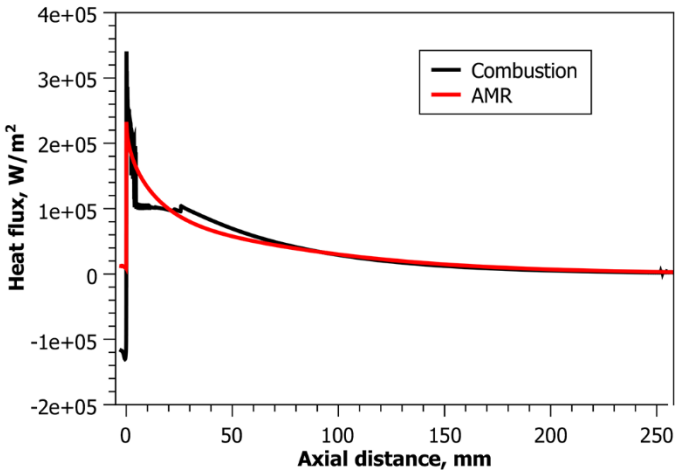

Figure 22. Heat duty profiles for total heat duty of 85.7 W, corresponding to combustion capacity of 0.235 CH_4 (green) and reforming capacity of 0.75 SLPM CH_4 (red) and overall thermal efficiency of 60 %.

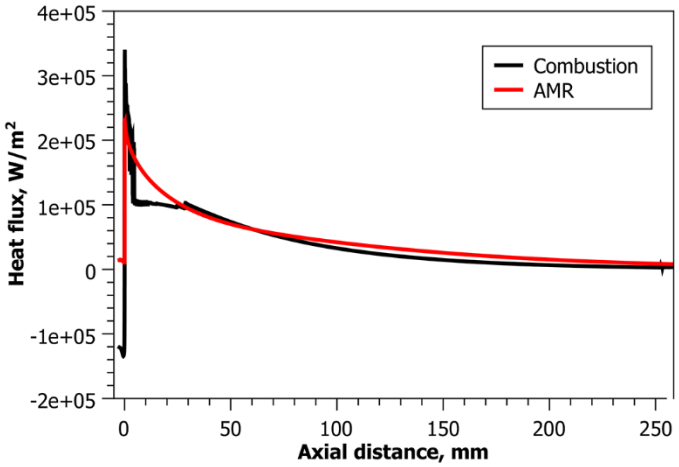

Figure 23. Heat duty profiles for total heat duty of 111 W, corresponding to combustion capacity of 0.251 CH_4 (green) and reforming capacity of 0.75 SLPM CH_4 (red) and overall thermal efficiency of 61%.

3.3 Conclusions

Our previous research effort provided net reforming heat duty and axial heat duty profiles required for maintaining an AMR outer wall temperature of 1023K and identified a viable reformer operating range between 0.5 and 2.0 SLPM dry-basis CH_4 supplied to each individual AMR reforming volume with a nominal operating condition of 1 SLPM dry-basis CH_4 per AMR. The present analysis employed separate stand-alone CFD simulations of the AMR combustion volume, assuming a fixed AMR outer wall temperature of 1023K while varying combustion inlet flowrate to match the net reforming heat duties identified previously. Simulation results thus predict the required dry-basis methane feed rate to the combustion chamber (on a per-AMR basis) required to meet the reformer net heat duty while maintaining the target outer AMR wall temperature. These flow rates were employed to predict combustion heat utilizations of 67 – 61% over the range of 0.25 – 1.0 SLPM dry-basis CH_4 feed rate to each AMR reforming volume. Comparison of axial heat duties predicted for matched combustion and reforming flowrates indicate acceptable agreement in local heat duties at all flowrates. Thus, it is expected that catalytic combustion is a viable means of providing heat to the AMR.

4. CATALYST DESIGN IN MICROREACTORS*

Unlike conventional packed-beds, wherein catalyst particles are symmetrically exposed to reaction fluid, microreactors employ thin films of catalyst supported by the heat transfer media (wall). One-D non-isothermal reaction-diffusion analysis was used to determine the possibility of gaining higher effectiveness factors for conventionally-determined film thicknesses, or conversely achieving comparable effectiveness at higher than conventional film thicknesses, through exploiting internal heat addition to the catalyst present in the AMR design. Using dimensional proportions corresponding to methane steam reforming, analysis predicted high thermal efficiencies and higher effectiveness factors may be achieved at higher catalyst thickness than conventionally used. This hypothesis was tested using an experimentally validated computational fluid dynamics model of an Annular Microreactor (AMR) device, currently under development by Power+Energy, Inc. The effectiveness factor for each catalyst thickness was compared with an isothermal reference case at flow rates corresponding to 95% of equilibrium conversion of methane, and a flow rate much greater than equilibrium conversion. The thermal efficiency was calculated for the non-isotheral system for each case. In all cases the non-isothermal catalyst with external heating had a higher relative average effectiveness with a thermal efficiency greater than 100%. This investigation

* Reprinted with permission from *Enhancing catalyst effectiveness by increasing catalyst film thickness in coated-wall microreactors: Exploiting heat effects in catalytic methane steam micro-reformers* by Butcher, H. and B.A. Wilhite, 2016. Chemical Engineering Science, 143, 47-54, Copyright 2016 by Elsevier Ltd.

proves that a thicker catalyst can be used to increase hydrogen production with little loss in effectiveness, thus improving the reforming capacity in existing microreactors.

4.1 Theory

In this section, a one dimensional study using first order irreversible kinetics is employed to verify the feasibility of enhancing catalyst effectiveness by exploiting internal heat addition. The study is conducted over a range of conditions to show wide-scale feasibility and tested for parameters that would occur in the steam reforming of methane. Once the feasibility was proven for this reaction, a two dimensional computational fluid dynamics model of the AMR system developed by Power & Energy was constructed.

Over the past decade, several heat-exchanger micro-reactor designs have been reported for hydrogen production via methane steam reforming coupled with combustion and/or partial oxidation[58, 94, 95, 101, 104-106]. To-date, research has aimed at optimizing the methane conversion and hydrogen yield through the variation of design parameters such as temperature, steam to carbon ratio, and residence time [57, 137] or design parameters such as the thermal conductivity of the supporting wall [58, 104] or catalyst loading [137, 138]. Additionally, several optimization studies have been conducted in the interest of maximizing methane conversions by investigating the potential of countercurrent flow and the offsetting of reactions zones [139], the use of stripe combustion catalyst patterning [140], and the use of phase-change media [63, 64],

in order to minimize hotspots. Common to the majority of studies to-date is the assumption of isothermal and/or unity effectiveness catalyst justified by the use of thin catalyst washcoatings. In contrast to this practice, the present study aims to identify new catalyst design rules for maximizing production capacity through exploiting the presence of direct internal heat addition to the catalyst film at the wall-catalyst interface in sufficiently thick washcoatings.

Traditional catalyst design rules are based upon the mathematical treatment of a symmetrical catalyst particle suspended in a fluid supplying both heat and mass to the catalyst, such that heat and mass source conditions (either in form of Direchlet or Robin-type boundary expressions) are located at the outer boundary of the reaction-transport domain while zero net flux of heat and mass is assumed at an inner boundary corresponding to the center of the symmetry [141-146]. By exploiting shape-, kinetics- and reaction reversibility normalizations [142-144, 147], a robust rule-of-thumb expression relating expected catalyst effectiveness (η) in terms of the Thiele modulus (ratio of reaction to diffusion rates within the catalyst body) in the absence of external mass or heat transfer resistances is obtained which in turn indicates a maximum value for ϕ of 0.4 to ensure an effectiveness of greater than 95%:

$$\boldsymbol{\eta_{cat} = \frac{\tanh(\phi)}{\phi} = 0.95 \rightarrow \phi = 0.4} \quad [58]$$

where ϕ is the normalized Thiele modulus relating catalyst particle size or washcoating thickness to reaction and diffusion rates as follows:

$$\boldsymbol{\phi^2 = \frac{L^2 r(C_f, T_f)}{C_f D_{eff}}} \quad [59]$$

This results in a sufficiently thin catalyst layer as to prevent significant reduction in internal reaction concentration arising from internal diffusion resistances. However, in the presence of internal heating of the catalyst (such that a finite heat flux condition occurs at the inner boundary), reduction in local reaction rates due to species depletion via diffusional resistances may be countered by local elevation of temperature. In the case of heat-exchanger microreactors, this elevation arises from a combination of heat addition at the inner boundary (catalyst-wall interface) and conductive heat resistances within the catalyst film arising with the use of unconventionally-thick ($\phi > 0.4$) catalyst films. Given that defect-free and smooth catalyst washcoatings of 30-100 μm have been readily achieved in meso-to microscale channels, the use of thicker catalyst coatings is a viable means to exploit heat effects at the catalyst-scale in microreactors[148, 149].

This section provides a demonstration of this new design approach as follows. First, a representative non-isothermal one-dimensional reaction-diffusion model with first order irreversible kinetics is employed to verify the feasibility of enhancing catalyst effectiveness by exploiting internal heat addition and identify parametric design rules. These design rules are validated using a two dimensional computational fluid dynamic (CFD) model, previously described and experimentally validated by the authors [112, 150], of an industrial annular microreactor (AMR). The CFD model is employed to predict local and overall catalyst effectiveness factors alongside overall thermal efficiencies at reformer flow rates corresponding to 95% of equilibrium conversion of

methane via MSR over a range of catalyst thicknesses corresponding to ϕ= 0.27 – 2.4 (10 – 90 micron).

4.1.1. One Dimensional Analysis of Internally-Heated Slab Catalyst

A one-dimensional reaction-conduction-diffusion model assuming negligible fluid-catalyst transport resistances is employed for parametric analysis of the impact of internal heating of a slab-catalyst upon both local heat utilization and catalyst efficiency for the case of an endothermic unimolecular first-order irreversible reaction. Within the catalyst slab, mass, conduction, and reaction are described by:

$$\frac{\mathbf{d^2u}}{\mathbf{ds^2}} = \boldsymbol{\phi}^{\mathbf{2}}\ \mathbf{f(u,v)} \qquad [60]$$

$$\frac{\mathbf{d^2v}}{\mathbf{ds^2}} = -\boldsymbol{\beta}\ \boldsymbol{\phi}^{\mathbf{2}}\ \mathbf{f(u,v)} \qquad [61]$$

with dimensionless boundary conditions

$$\text{at } \mathbf{s = 0} \qquad \frac{\mathbf{du}}{\mathbf{ds}} = \mathbf{0}\ ; \quad \frac{\mathbf{dv}}{\mathbf{ds}} = \boldsymbol{\chi} \qquad [62]$$

$$\text{at } \mathbf{s = 1} \quad \mathbf{u = 1, v = 1} \qquad [63]$$

where the Thiele modulus (ϕ), Prater number (β), dimensionless activation energy (γ) and ratio of internal heat addition to conduction (χ) are defined as follows:

$$\phi^2 = \frac{L^2 r(C_f,T_f)}{C_f\, D_{eff}};\quad \beta = \frac{-\Delta H\, C_f\, D_{eff}}{k_{eff}\, T_f};\quad \gamma = \frac{E_A}{R * T_f};\quad \chi = \frac{q}{T_f}\cdot\frac{L}{k_{eff}} \qquad [64]$$

And the dimensionless rate of reaction is

$$f(u,v) = \frac{k_o \cdot C \cdot \exp\left[\frac{-E_A}{RT}\right]}{k_o \cdot C_f \cdot \exp\left[\frac{-E_A}{RT_f}\right]} = u \cdot \exp\left[\gamma\left(1 - \frac{1}{v}\right)\right] \qquad [65]$$

Numerical solution to the above pair of differential equations were obtained using the BVP4C package in the Matlab programing environment and employed to calculate catalyst effectiveness and internal heat utilization. The former, defined as the net volumetric rate of catalytic reaction normalized by the expected rate in the absence of heat and mass transport limitations, may be obtained from derivative analysis of the numerical solution as follows:

$$\eta_{cat} = \frac{\int_V r(T,C)dv}{r(T_f,C_f)\int_V dv} = \frac{1}{\phi^2}\frac{du}{ds}_{s=1} \qquad [66]$$

The internal heat utilization is defined as the net heat consumption by endothermic reaction within the catalyst slab normalized by the rate of internal heat addition,

$$\eta_T = \frac{\int_0^1 \beta\phi^2 f(u,v)\, ds}{\frac{dv}{ds}_{s=0}} = \frac{\frac{dv}{ds}_{s=0} - \frac{dv}{ds}_{s=1}}{\frac{dv}{ds}_{s=0}} \qquad [67]$$

The above model allows identification of design conditions necessary for complete local utilization of internally supplied heat (i.e. $\eta_T = 1$) while achieving local catalyst effectiveness in excess of unity ($\eta_{cat} \geq 1$). These design conditions in turn enable identification of a suitable set of dimensional operating conditions for simulating the performance of an industrial microreactor design previously reported by the authors [112, 150].

4.1.2. Two Dimensional Analysis

A previously developed two-dimensional computational fluid dynamic (CFD) model, implemented in COMSOL v4.2a and describing an annular microchannel reactor (AMR) for the endothermic methane steam reforming of a 3.3:1 H_2O:CH_4 mixture at 11 bar and 750 ºC, is employed in the present study to predict overall and local heat utilization and catalyst effectiveness over an appropriate span of axially-uniform film thicknesses [136]. The AMR design consists of a 2.46 mm x 228.6 mm open ended inner tube of wall-thickness 0.25 mm, suspended within a 3.82 mm x 247.65 mm closed-ended outer tube of wall thickness 0.38 mm. The catalyst film is uniformly coated over the inner surface of the outer-tube, such that the 0.3 mm-wide annular volume acts as a catalytic-wall annular microreactor with internal heating of the catalyst provided by external heating of the AMR by resistive heating, appropriate heat-transfer fluid or thermally-balanced exothermic chemical reaction. For these simulations a 25.4 mm (1 inch) relaxation zone was added before and after the catalyst coating resulting in a

catalyst coating of 177.8 mm long (7 inches) with the thickness being changed for each case.

The CFD model employs a combination of laminar flow, (Navier-Stokes and continuity of mass) heat conduction and convection, and Maxwell-Stefan convection-conduction physics with appropriate correlations for fluid density, viscosity, heat capacity, thermal conductivity, and individual binary-pair diffusivities to describe the gas or fluid phase. A combination of Darcy's law (for convection in porous media), heat convection-conduction and Maxwell-Stefan convection-conduction physics with methane steam reforming and water-gas-shift kinetics from Xu and Froment [127] describe the catalyst film. A catalyst temperature boundary condition imposed on the outer wall of the microreactor (**Figure 24**) allows solution with an axially-varying rate of heat addition necessary to satisfy the isothermal boundary condition, experimentally provided through multi-stage resistive heating [136]. A complete description of expressions, model of the methane steam reforming AMR, and its validation with experimental data are provided elsewhere [112, 150].

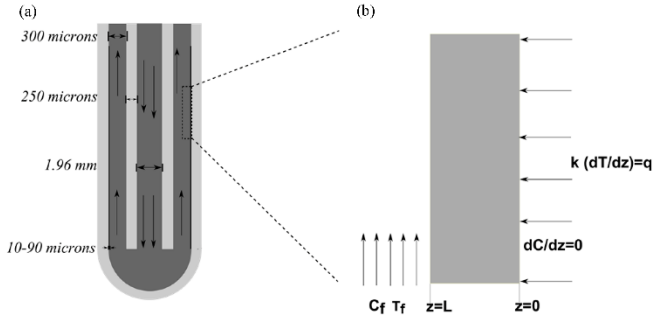

Figure 24. (a)Schematic of AMR configuration and (b) one dimensional porous catalyst slab with boundary conditions.

Simulation results are employed to calculate local internal heat utilization and catalyst effectiveness for comparison with expected local catalyst effectiveness assuming an isothermal catalyst. Following Aris [151], inspection of the catalyst volume to surface area ratio for the case of a thin catalyst washcoating on the inside of a cylindrical wall indicates that for $t_c << r_1$, where t_c is the thickness of the catalyst washcoating and r_1 is the inner radius of the washcoating, the appropriate shape normalization corresponds to a Cartesian slab (i.e., n=1).

The actual local catalyst effectiveness is thus obtained from the interfacial (fluid-catalyst) mass flux and local Thiele modulus by the formula,

$$\boldsymbol{\eta_{cat} = \frac{1}{\phi_{obs}{}^2}\frac{du}{ds}_{s=1}, \text{where } u = \frac{C}{C_f}, s = \frac{z}{L}, \phi = L\sqrt{\frac{r(C_f,T_f)}{C_f D_{eff}}}} \quad [68]$$

The overall thermal efficiency (Eq. 12) was calculated using the energy input at the outer wall boundary via a surface integral of the total energy flux normal to heat

transfer surface area and individual species inlet and outlet enthalpies ($\mathbf{H_i}$) multiplied by their respective molar flow rates ($\mathbf{\dot{n}_i}$). Individual species enthalpies were obtained from the six-parameter Shomate equation with parameter values for each species obtained from the NIST Chemistry Webbook.

$$\boldsymbol{\eta_T = 1 - \frac{H_{out}}{H_{in} + Q_{rxn}} = 1 - \frac{\sum_i (H_i \dot{n})_{out}}{\sum_i (H_i \dot{n})_{in} + \oint\oint (q \cdot n) dS}} \quad [69]$$

It may be readily shown that for an endothermic catalytic reaction with finite internal diffusion resistance, assumption of an isothermal catalyst film always yields higher catalyst effectiveness than when true heat effects are considered; thus we select as an appropriate reference case an isothermal catalyst with finite internal mass transfer resistance. The isothermal catalyst effectiveness is obtained using the shape and kinetics-normalized correlation [151],

$$\boldsymbol{\eta_{iso} = \frac{\tanh\left[\frac{\phi}{\sqrt{\frac{2}{3}}}\right]}{\left[\frac{\phi}{\sqrt{\frac{2}{3}}}\right]}} \quad [70]$$

4.2. Results and Discussion

4.2.1. 1-D Results

The one dimensional model was used to investigate the possible improvement in catalyst effectiveness due to internal heating of the catalyst. Operating conditions for the AMR system (discussed in a previous manuscript [136]) are used to obtain a baseline parameter set [ϕ,β,χ,γ] for one-dimensional analysis (**Table 10**). In brief, feed compositions correspond to a 3.3:1 molar supply of steam to methane, pre-heated to a feed temperature of 750^{o}C, in the absence of inert species while a variable heat duty (achieved experimentally via multi-stage electrical heating) along the microchannel length is employed to maintain a uniform wall temperature of 750^{o}C. Flow through the inner tube and tube cap have been accounted for including all heat transfer implications due to heat transfer through the wall, using material properties for Kanthal. These values provide a point of comparison between one-dimensional analysis and subsequent simulations of the AMR system.

Table 10. Parameter values for operating conditions present in AMR system for MSR

Parameter	AMR values	Operating conditions
β	-0.22	T=1023 K
γ	28.2	P=11 atm
χ	> 0	S/C=3.3
ϕ	0.76	Catalyst thickness= 30μm

Figure 25 presents internal heat utilization (η_T) and catalyst effectiveness (η_{Cat}) as a function of catalyst thickness (via varying ϕ) for the case of γ=28.2 and β=-0.22 with internal heating matched to the local catalyst heat duty ($\beta=\chi$). Three critical values of ϕ are identified from Figure 25, the first being a minimum value for ϕ above which the local heat utilization is unity (ϕ^{**}) and the second being a maximum value of ϕ below which the catalyst effectiveness is greater than unity (ϕ^{*}), and a third is the minimum value of ϕ at which the catalyst effectiveness for the internal heating case becomes equal to the isothermal case where above this value the internal heating case would be less effective than the isothermal case ($\phi^{\dagger}$).

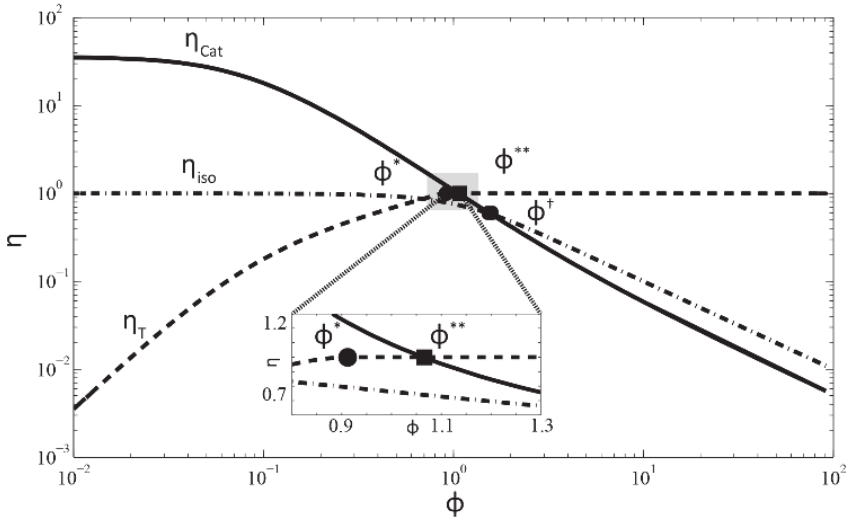

Figure 25. η_{Cat} (dashed) and η_T(solid) vs. ϕ for γ=28.2 and β=χ=-0.22. Inset illustrates the operating window corresponding to ϕ*=1.065 and ϕ**=0.91, wherein complete internal heat utilization corresponds to greater-than-unity catalyst effectiveness. $\phi^\dagger$ is labeled at ϕ=1.571 to show the intersection of $\eta_{Cat\ and}$ η_{iso}.

The range of values $\phi \in (\phi^{**},\phi^*)$ thus represent a favorable design window in which catalyst film thickness is sufficient to trap locally supplied heat such that complete internal heat utilization may be achieved without loss in catalyst effectiveness arising from internal diffusion and/or conduction resistance. Furthermore, values of ϕ below $\phi^\dagger$, inside or outside the $\phi \in (\phi^{**},\phi^*)$ range, achieve greater catalyst utilization than expected by conventional design.

The dependence of ϕ* and ϕ**, and thus the above described operating window, upon γ, β and χ was investigated as follows. For the case of matched internal heating to catalyst heat duty (χ=β), catalyst heat duty was varied from 0 to -0.3 at fixed dimensionless activation energy (γ=28.2) and values for ϕ* and ϕ** were obtained at

each parameter set (**Figure 26**). A minimum absolute value of β (β^*=-0.105) is identified, below which the aforementioned design window $\phi \in (\phi^{**},\phi^*)$ does not exist as $\phi^{**} > \phi^*$ for $\beta < \beta^*$. Likewise, varying dimensionless activation energy (γ) from 5-30 while maintaining matched values of $\beta=\chi$=-0.22 (**Figure 26b**) identifies a minimum activation energy (γ^*=14.08) below which $\phi^{**} > \phi^*$, corresponding to the non-existence of the design window $\phi \in (\phi^{**},\phi^*)$. It is worth noting from Figure 3a,b that the conventional design rule (ϕ = 0.4) also corresponds to greater-than-unity catalyst efficiency, but at the cost of negligible local heat utilization internal to the catalyst slab; this corresponds to a direct heating of the bulk fluid via internal heating of the catalyst which results in non-trivial fluid-phase axial temperature profiles. Lastly, varying dimensionless internal heating parameter (χ) at fixed values for activation energy (γ=28.23) and catalyst heat duty (β=-0.22) sufficient to ensure existence of the catalyst design window $\phi \in (\phi^{**},\phi^*)$, confirming the existence of this operating window for all non-zero values of χ (**Figure 26c**). The effects of internal heating, χ, on β^* can be seen in **Figure 26d**, where β^* was found for the cases of $\chi=\beta$ (solid), χ=-0.1 (dashed), and χ=-0.2 (dot).

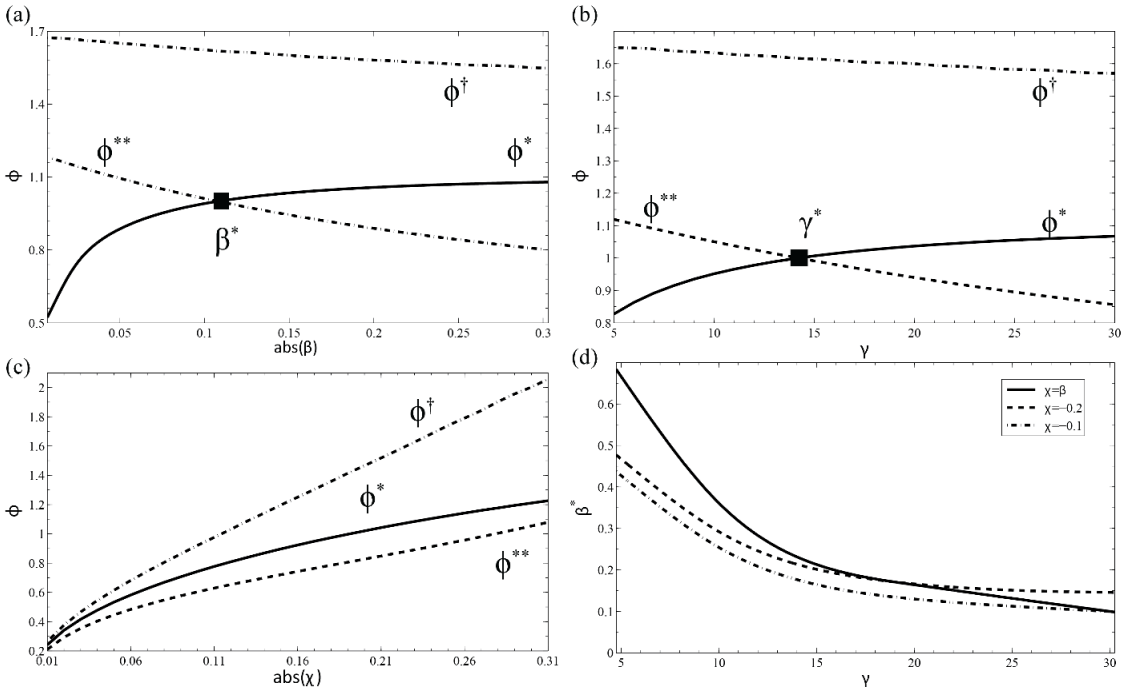

Figure 26. Window of $\phi^*>\phi^{**}$, corresponding to enhanced effectiveness at complete local heat utilization. ϕ^*,ϕ^{**}, and $\phi^\dagger$ as a function of (a) β, indicating minimum value (β^*) for existence of $\phi^*>\phi^{**}$, (b) γ, indicating the minimum value (γ^*) for existence of $\phi^*>\phi^{**}$, (c) χ, indicating all nonzero value of χ result in $\phi^*>\phi^{**}$; and β^* as a function of γ.

Thus, the present parametric study indicates the existence of a loci in β-γ-χ space delineating conditions wherein internally-heated catalyst designs may be realized with complete local utilization of both catalyst and internally-supplied heat. This boundary corresponding to the condition that $\phi^*=\phi^{**}$ or ($\eta_T=\eta_{cat}=1$ at $\phi^*=\phi^{**}$) is presented in **Figure 26d** for the cases of χ=β (solid), χ=-0.1 (dashed), and χ=-0.2 (dot).

Previous experimental and simulation reports of the industrial AMR system for performing the endothermic methane steam reforming process employed a catalyst

thickness of 30 microns, corresponding to a value of ϕ = 0.76 (as noted in **Table 10**). The above analysis using dimensionless parameters corresponding to the operating conditions employed for the industrial AMR suggest an optimal catalyst design window of $\phi \in (0.91..1.065)$ or thicknesses of 34-40 microns based on reference conditions. Moreover, an enhancement over conventional design can be seen when $\phi<1.571$ or a thickness up to 59 microns based on reference conditions. In the following section, a previously developed and experimentally validated CFD model of the AMR system is employed to investigate whether an improvement in overall catalyst effectiveness, and thus overall reactor productivity may be achieved through implementation of the above design rules.

4.2.2 2-D Results

Fourteen different catalyst thicknesses, ranging from 10 - 90 microns and corresponding to 33% - 300% of the thickness previously reported for the AMR system [112, 150] were investigated via CFD simulation. For each catalyst thickness, a flow rate corresponding to 95% of equilibrium methane conversion was identified (**Table 11** and **Figure 27**) in order illustrate the impact of catalyst thickness upon overall reactor productivity while providing a uniform basis for subsequent comparison of catalyst performance as a function of thickness. An equilibrium conversion of 75.6% was obtained via separate Gibb's reactor calculations in Aspen Plus at the operating conditions present in the AMR system (P = 11bar, T = 750^{o}C). Simulation results were

analyzed to determine catalyst effectiveness predicted from classical theory, actual catalyst effectiveness, and thermal efficiency as a function of axial position at each catalyst thickness.

Table 11. Flowrate corresponding to 95% equilibrium methane conversion (64% hydrogen yield) for each catalyst thickness

Thickness	Vin m/s	flowrate m^3/s	Hydrogen outlet flowrate (mol/s)
10	2.17	6.60E-6	5.03E-4
15	3.12	9.48E-6	7.25E-4
20	3.98	1.21E-5	9.27E-4
25	4.74	1.44E-5	1.11E-3
30	5.41	1.64E-5	1.27E-3
35	6.00	1.82E-5	1.41E-3
40	6.50	1.98E-5	1.54E-3
45	6.94	2.11E-5	1.64E-3
50	7.30	2.22E-5	1.73E-3
55	7.61	2.31E-5	1.81E-3
60	7.85	2.38E-5	1.88E-3
70	8.20	2.49E-5	1.97E-3
80	8.38	2.55E-5	2.03E-3
90	8.46	2.57E-5	2.07E-3

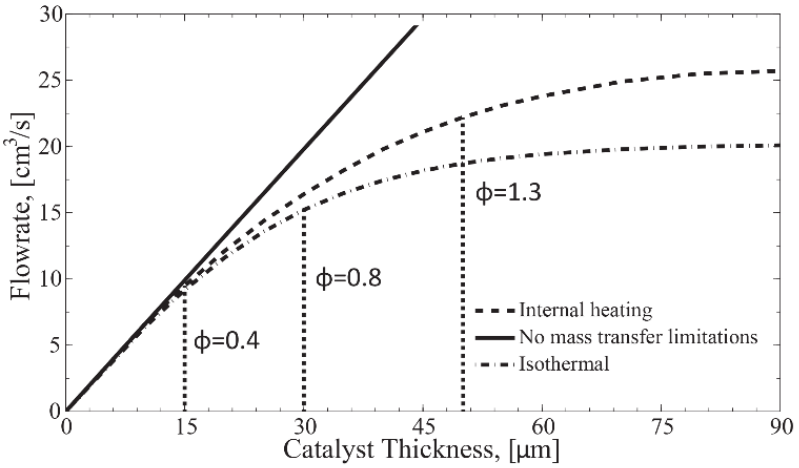

Figure 27. Reformer capacity corresponding to 95% of equilibrium methane conversion as a function catalyst thickness. Dashed lines correspond to expected relationship assuming unity catalyst efficiency (i.e., absence of mass transfer limitations) and estimating catalyst efficiency via Eq. 1. (i.e., isothermal catalyst efficiency, or in absence of internal heating effects).

Figure 27 shows that at catalyst film thicknesses greater than 15 microns ($\phi >$ 0.4), internal mass transfer resistances begin to reduce the achievable reforming capacity at the target methane conversion of 95% of equilibrium (corresponding to an overall H_2 yield of 65%). However, when compared to the traditionally expected reduction in reforming capacity (assuming overall effectiveness may be estimated using Eq.49, it is seen that the presence of internal heat addition to the catalyst inner-boundary mitigates these mass transfer resistances.

.

Table 12. Results for two-dimensional simulations of the AMR system

Catalyst Thickness [microns]	Outlet Temperature [K]	Hin	Hout	Qrxn [W]	Thermal Efficiency	Inlet Thiele	Outlet Thiele	Volume-Average Relative Improvement (%)	Maximum Local Relative Improvement (%)
10	1023	-0.147	-0.118	-28.9	0.996	0.27	0.07	0.43	0.71
15	1023	-0.212	-0.170	-41.7	0.996	0.40	0.10	0.81	1.76
20	1023	-0.271	-0.218	-53.1	0.996	0.53	0.13	1.20	2.90
25	1023	-0.325	-0.260	-63.3	0.996	0.65	0.16	1.66	4.06
30	1023	-0.373	-0.298	-72.2	0.996	0.77	0.19	2.08	5.64
35	1023	-0.414	-0.331	-80.2	0.996	0.90	0.22	2.46	7.34
40	1023	-0.450	-0.361	-87.0	0.996	1.02	0.25	2.89	8.88
45	1022	-0.481	-0.386	-92.8	0.996	1.14	0.28	3.05	9.68
50	1022	-0.509	-0.407	-97.6	0.996	1.26	0.31	3.49	11.47
55	1022	-0.531	-0.426	-101.6	0.996	1.37	0.34	3.63	13.33
60	1022	-0.551	-0.440	-105.1	0.996	1.48	0.36	3.68	14.17
70	1022	-0.579	-0.465	-109.9	0.996	1.71	0.41	3.95	19.44
80	1021	-0.597	-0.476	-112.7	0.996	1.94	0.46	4.10	19.37
90	1021	-0.605	-0.484	-113.4	0.996	2.18	0.51	3.19	25.07

Table 12 presents CFD simulation results used to determine thermal efficiency (Eq. 60), which indicates an overall thermal efficiency of approximately 99.6% is maintained for all film thicknesses when flowrate is selected such that 95% of equilibrium methane conversion is achieved. **Table 12** also quantifies the reduction in Thiele modulus from the reactant-rich inlet region of the reactor to that of the reactant-poor outlet; thus, local enhancements in catalyst effectiveness over the reference case of an isothermal film are expected to occur primarily within the inlet region of the microreactor. For this reason, volume-averaged relative improvements, which balance significant local improvements near the reformer inlet against negligible improvements or reduction in performance near the outlet, are also provided in **Table 12**. Results indicate that there is a significant improvement in both volume-averaged relative improvement and maximum local relative improvement in catalyst effectiveness, as compared against an isothermal catalyst of identical thickness, for the case of an internal heated catalyst.

Axial heat duty and gas-phase composition profiles for the case of a 90-micron thick catalyst washcoating are presented in **Figure 28a** in terms of the dimensionless Prater temperature, activation energy, local catalyst effectiveness and estimated isothermal catalyst effectiveness under identical conditions. **Figure 28b** shows the three critical values of Thiele modulus at the local conditions presented in **Figure 28a** and the corresponding local Thiele modulus. **Figure 28b** shows that while the Thiele modulus is outside of the ϕ^*, ϕ^{**} range, it is still lower than the critical value $\phi^{\dagger}$ (with the exception of the first 10mm of the catalyst region), indicating that even outside of the ϕ^*, ϕ^{**}

range internal heating allows for higher than classically predicted catalyst effectiveness. At axial positions > 110mm, depletion of methane reactant is sufficient for the actual catalyst effectiveness to drop below that of the ideal case, indicating that further advances in performance may be achieved via appropriate step-profiling of catalyst film thickness to maintain local ϕ within ϕ^*, ϕ^{**} range. This may be achieved via optimization of a multi-step catalyst thickness profile corresponding to a single, target reforming capacity, which will be the subject of subsequent study. A similar approach is used by Pattison et al.[63], where the use of catalytically active and inactive zones are optimized for both the methane steam reforming and the paired exothermic reaction of combustion of methane [65].

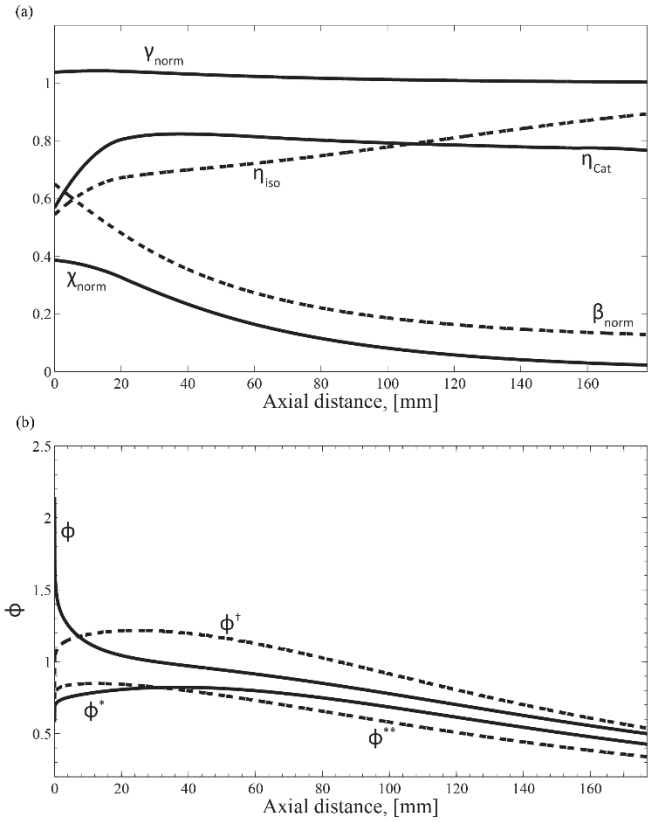

Figure 28. Ninety micron thickness properties vs. axial length (a) Local catalyst effectiveness and local normalized variables (normalized by reference conditions: -0.22, 28.23 and -0.22 for β, γ and χ, respectively) (b) Thiele modulus comparison down axial length

Catalyst deactivation is detrimental to reactor performance and in many cases cause a domino effect of deactivation by sintering due to thermal interactions between channels. However in the case of the AMR, each tube is thermally isolated, catalyst deactivation in a single AMR tube would have little effect on operation of the other tubes due to sufficiently high thermal conductivity media that exists between each tube. Recently, the companies Velocys and Mourik have set out to solve the problem of

replacing catalyst in microreactors [152]. They report using a technique of delamination that dissolves adhesion of the film from the reactor walls. In the future, this technique could be utilized to replace the catalyst.

4.3 Conclusions

The above analysis confirms that the use of unconventionally-thick catalyst washcoatings in the endothermic reforming chambers of a heat-exchanger microreactor is a viable and promising means to increase reforming capacity at a minimum reduction in catalyst effectiveness. One-dimensional analysis identified design rules for implementing sufficiently thick catalyst films such that accumulation of heat supplied at the internal boundary of the catalyst film (i.e., catalyst-wall interface) is exploited to maintain high rates of reaction throughout the catalyst film in the presence of moderate diffusional resistances. CFD simulations of an industrial catalytic-wall micro-channel reformer design for methane steam reforming, operated with variable axial heating rates such that the catalyst-supporting wall remains isothermal at 750^{o}C, confirm the validity and promise of this approach to increase microchannel reformer capacity. Comparison of local catalyst effectiveness against predicted isothermal effectiveness along the entire axial length of an AMR with a 90-micron (ϕ = 2.18 at inlet) catalyst washcoating operated at a flowrate corresponding to an outlet methane conversion of 95% equilibrium value at 750^{o}C confirm up to a 25.1% improvement in local catalyst efficiency near the inlet, owing to the internal accumulation of supplied heat within the

catalyst film itself. These conditions correspond to a volume-averaged 3.2% improvement over isothermal case, indicating the potential to further improve overall catalyst effectiveness via step-wise patterning of washcoating thickness over the length of the microchannel.

Along with these potential improvements, it should be mentioned that the use of a thicker catalyst film would be associated with additional capital costs and a reduction in the flow channel area. However, the increase in production capacity per AMR tube would reduce the number of parallel tubes, potentially saving more capital overall depending on the consumer's needs. Additionally, when using the 90 micron thickness (32.3% of the annular area), the reduction in flow area is a 9 fold the reduction when compared to the 10 micron case (3.7% of the annular area) and a 3 fold reduction in area when compared to the 30 micron case (11.0% of the annular area), resulting in only a mild increase in pressure across the reactor of 6% and 4%, respectively.

5. COUPLED METHANE STEAM REFORMING AND COMBUSTION

In this section, modeling analysis of an individual AMR unit combining methane steam reforming within the annular reaction zone and catalytic combustion of methane on the outer AMR surface is presented. The uncoupled model provides an initial estimate of required combustion flowrates to drive the MSR process at reduced computational cost. Coupled (or simultaneous) modeling of both MSR and combustion volumes provides accurate prediction of local temperature profiles and thus more precise prediction of overall system performance. Two coupled models are reported; the first has symmetric axial placement of combustion and reforming catalyst on either surface of the AMR outer wall; the second has off-set combustion catalyst in an attempt to match the steep and abrupt heat duty requirements of the first few axial inches of the steam reforming volume, following techniques previously employed in analogous planar reactors [139].

5.1 Model Description

Two-dimensional, steady-state models of the AMR were developed to identify a heat-integrated AMR design for directly coupling endothermic methane reforming with exothermic catalytic combustion of methane. Three specific modeling cases are explored; (I) separate modeling of the reforming chamber and combustion chamber assuming a shared isothermal dividing wall; (II) simulates modeling of the coupled

reforming-combustion chambers with symmetric coating of combustion and reforming catalyst, and (III) simulates modeling of the coupled reforming combustion chambers with asymmetric coating of combustion and reforming catalyst where the combustion catalyst is coated on the AMR tube tip. Model geometries for the three cases are presented in Figure 29. All models were developed in the COMSOL Multiphysics v4.2a platform. A detailed description of the steam reforming model is provided in section 2 and the combustion model is provided in section 3. The model description remains identical for the three cases with the exception that homogeneous combustion of methane (shown in section 5.1.2) is included for case II and case III and only minor changes in model geometry. The operating window over which these models were implemented over was previously determined by the authors [136]. The three cases are compared using performance metrics such as overall thermal efficiency, hydrogen yield, reforming methane conversion, and heat utilization.

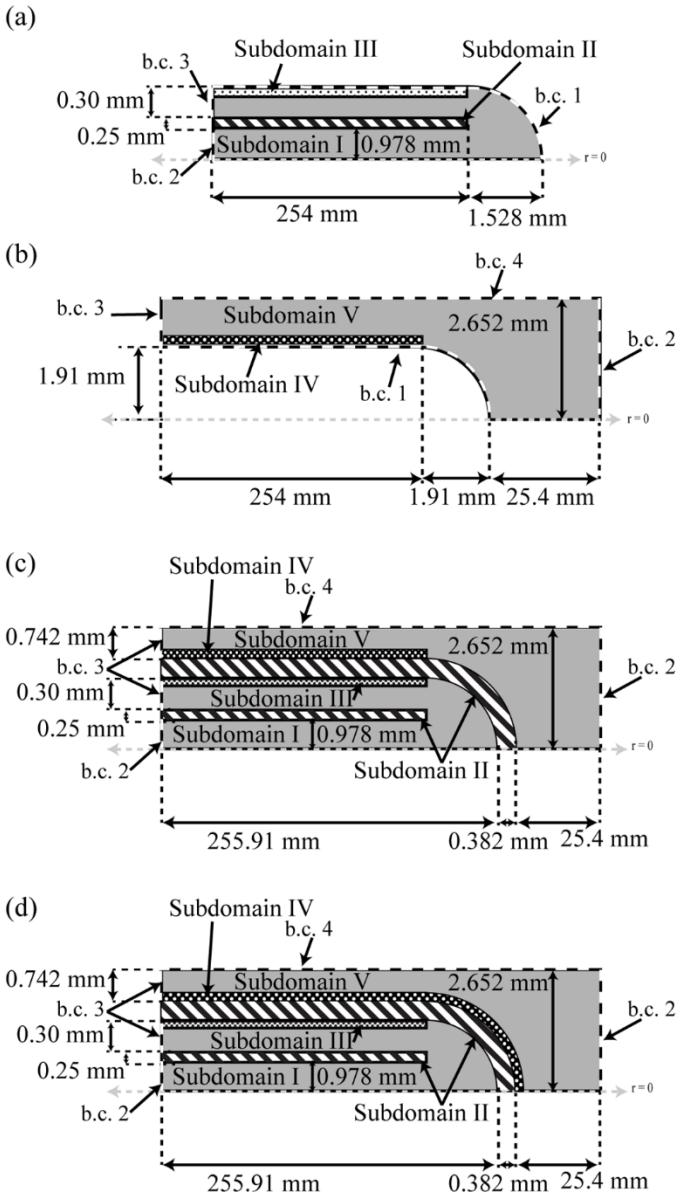

Figure 29. Geometries for 2-D COMSOL simulations with relevant boundary conditions (a) Methane steam reforming with isothermal wall (b.c. 1), (b) Combustion of methane with isothermal wall (b.c. 1), (c) case II- coupled reactor with symmetric catalyst coatings and (d) case III- coupled reactor with asymmetric catalyst coatings. Table 13 details subdomain and boundary condition information.

Table 13. Subdomain and boundary condition details corresponding to **Figure 29**.

Subdomain	Associated Volume	
I	Fluid volume for methane steam reforming	
II	AMR wall volume	
III	Methane steam reforming catalyst volume	
IV	Catalytic combustion of methane catalyst volume	
V	Fluid volume for combustion	
Boundary Condition	Steam Reforming	Combustion
b.c. 1	Constant temperature (T=1023.15 K). No slip, no mass flux.	Constant temperature (T=1023.15 K). No slip, no mass flux.
b.c. 2	Constant inlet mole fractions of 0.76438, 0.23163, 0.001, 0.001, 0.001 for H2O, CH4, CO, CO2, and H2, respectively, with balance N2; constant temperature (T=1023.15 K) and constant uniform velocity.	Constant inlet mole fractions of 0.19, 0.08, 1e-20 and 1e-20 for O2, CH4, H2O, CO2, respectively, with balance nitrogen; constant temperature (T=623.15 K) and constant uniform velocity.
b.c. 3	Open boundary, constant pressure (P= 11 atm).	Open boundary, constant pressure (P=1 atm).
b.c. 4	-	Symmetry

For case I, the reforming and combustion volumes are modeled separately, assuming an isothermal boundary condition of 1023.15 K at the shared outer AMR wall. Stand-alone simulation of each volume allows for rapid investigation of the efficacy of pairing methane steam reforming with combustion of methane in the AMR geometry. Cases II and III pair these separate volumes in a single model by removing the isothermal dividing-wall boundary condition, thus accounting for heat conduction across the shared outer AMR tube wall. Case II employs symmetric patterning of both

reforming and combustion catalyst on either side of the outer AMR tube wall. Case III introduces combustion catalyst to the tip of the AMR tube, off-setting the combustion reaction zone from the beginning of the steam reforming reaction zone, in an attempt to balance the significant endotherm at the reforming zone inlet.

In previous, models detailed in sections 2 and 3 the wall separating the annular AMR volume from external combustion volume were assumed to be infinitely thermally conductive. However in this section for cases 2 and 3 they were included with the same physics as the wall separating the inlet from the annular volume. The heat transfer for the wall is included this section to reiterate the equation used and the wall material properties.

5.1.1 Reactor Wall (Solid-Phase) Expressions

Conductive heat transport within the outer and inner AMR walls (separating inlet from annular volumes of the AMR, and annular AMR volume from external combustion volume, respectively) are modeled using **Eq. 71**, below.

$$\mathbf{0} = \boldsymbol{\nabla} \cdot (\mathbf{k_{wall}} \boldsymbol{\nabla} \mathbf{T}) \qquad [71]$$

Constant temperature values for solid phase heat capacity, density, and thermal conductivity of 0.71 kJ kg^{-1} K^{-1}, 7100 kg m^{-3}, and 22 W m^{-1} K^{-1} , respectively, were provided by the supplier, AB Sandvik, for use in the model.

5.1.2 Homogenous Combustion of Methane

A one-step simplified reaction mechanism is used to describe homogenous combustion of methane (HCM) (**Eq. 72**). This mechanism is validated in the literature 72under a range of fuel-lean to fuel-rich conditions and reactor pressures (1 to 25 atm) [153]. Current simulated conditions fall between these limits (P ≥ 1 atm and 14% excess air). Homogenous combustion is not included in the case I combustion model (**Figure 29b**) as that model served solely as a proof-of-concept study.

$$\mathbf{R_{HCM} = 8.3e5 \ * exp\left(\frac{-E_A}{RT}\right) * C_{CH_4}^{-0.3} C_{CO_2}^{1.3}}\ \mathbf{, E_A = 30\ \frac{kcal}{mol}} \qquad [72]$$

5.1.3 Numerical Methods

The models described above were implemented using the commercial software COMSOL Multiphysics v4.2a equipped with the chemical engineering module. The fluid phase and catalyst phase domains were modeled using the free and porous media, heat transfer in fluids and transport of concentrated species physics packages. The tubing domain was modeled using heat transfer in fluids physics package. The model was solved using 2D geometries as summarized in Figure 2, applied to radial symmetry space. For case I, the finite-element meshes employed consisted of ~2.6 x 10^5 and 6.2 x 10^5 individual elements which corresponded to ~1.3 x 10^6 and 2.5 x 10^6 degrees of freedom for MSR and CM models, respectively. For case II and III, fully coupled

models, the finite-element meshes consisted of ~4.1 x 10^5 individual elements which corresponded to ~5.4 x 10^6 degrees of freedom. The error associated with numerical solutions was calculated from individual atomic mass balances and was found to be <1% for all reactive species (C, O, H) and <5% for the inert balance species (N_2), so uniform error bars of 1% will be used in the figures contained in the results section. Solutions were obtained using the Direct MUMPS (MUltifrontal Massively Parallel sparse direct Solver) solver, which is a multifrontal gaussian elimination method algorithm recommended for sparse matrixes[129]. All solutions were performed on a Dell PowerEdge R820 with eight (8) Intel Xeon CPU E5-4650 at 2.7 GHz and equipped with 256 GB of RAM. The typical solution times for both systems ranged from 400-8000 s.

5.2 Analysis of Simulation Results

Results of each simulation were analyzed by integrating individual species mass fluxes at the inlet and the outlet of the AMR and the heat flux into the catalyst film from the underlying support wall. Case I, the separate model geometries (**Figure 29 a and b**), was used to predict the performance of the AMR system, and prove the efficacy of pairing methane steam reforming with catalytic combustion of methane in the AMR configuration. Case I results were analyzed by pairing steam reforming capacities with matching combustion capacities via matching of overall heat duties across the dividing wall calculated using a surface integral of the total energy flux over the boundary marked by b.c. 1 (Figure 29 a and b). Cases II and III, (**Figure 29c and d**) combustion

capacities were chosen such that the outlet methane conversion of the steam reforming volume matched values obtained under identical reforming flowrates from case I. Molar outflows of each species were calculated from individual species' molar fluxes integrated across the outlet surface. Hydrogen yield was calculated based on the theoretical yield of hydrogen produced from the methane supplied (**Eq. 73**). Heat utilization (**Eq. 74**) was calculated by dividing the heat flux through the AMR wall separating reforming and combustion volumes by the maximum possible heat duty produced by the combustion volume at that flow rate. Thermal efficiency (**Eq. 75**) was defined as the outlet molar flowrate of hydrogen divided by the total inlet methane (both combustion and reforming) multiplied by their respective lower heating values.

$$\mathbf{Y_{H_2}} = \frac{\mathbf{1}}{\mathbf{4}} \frac{\mathbf{F_{H_2,e}}}{\mathbf{F_{CH_4,i}}} \mathbf{x\ 100\%} \quad [73]$$

$$\mathbf{Heat\ Utilization_{combustion}} = \frac{\oint\oint (\mathbf{q \cdot n}) \mathbf{ds}}{\mathbf{F_{CH_4,i_{CM}} * \Delta H_{CM}}} \quad [74]$$

$$\boldsymbol{\eta_T} = \frac{\mathbf{F_{H_2,e_{MSR}} * LHV_{H_2}}}{(\mathbf{F_{CH_4,i_{MSR}} + F_{CH_4,i_{CM}}}) * \mathbf{LHV_{CH_4}}} \mathbf{x\ 100\%} \quad [75]$$

5.3 Results and Discussion

Three cases were investigated: (I) separate MSR and CM volumes were modeled assuming a constant operating temperature boundary condition at the separating wall (II) symmetrically coupled MSR and CM volumes including a finite-thermal conductivity wall and (III) an asymmetrically coupled MSR and CM volumes. Five different

reforming capacities are investigated for each case. In all three cases, the five predefined steam reforming capacities (0.25, 0.33, 0.50, 0.75 and 1.00 SLPM CH_4, dry basis) were simulated, with combustion capacity varied to match heat duties of the two separate models (case I), or the overall methane conversion predicted by the MSR model in case I (case II,III). **Figure 30** summarizes the predicted hydrogen yield, heat utilization, required combustion flowrate and overall thermal efficiency for all three cases. Case 1 overpredicts combustion methane flow, which results in under prediction of heat utilization and thermal efficiency. This is owing to the simplifying assumption of an isothermal outer AMR wall that enables separate modeling of CM and MSR volumes. While overall heat duties are matched for case I, local differences in axial heat profiles are substantial. These heat duties were employed in a single 1-D conduction model (**Eq. 76**) of the outer AMR wall which predicted a local temperature deviation in excess of 500 K, in the absence of direct interaction between endothermic and exothermic reactions.

$$\mathbf{0} = -\mathbf{k_{wall}}\frac{\boldsymbol{\delta^2 T}}{\boldsymbol{\delta t^2}} + \hat{\mathbf{a}}(\mathbf{q}^+ + \mathbf{q}^-)\cdot\mathbf{n} \qquad [76]$$

Additional analysis was conducted on the simulation results from cases II and III, concentrating on the temperature profiles across the outer AMR wall and supported reforming catalyst. The temperature profiles are compared in **Figure 31a** and temperature surface maps of a portion of the reactor are shown in **Figure 31b and c** for

case II and III, respectively. Furthermore, three critical temperature values and corresponding positions are summarized in **Table 14**.

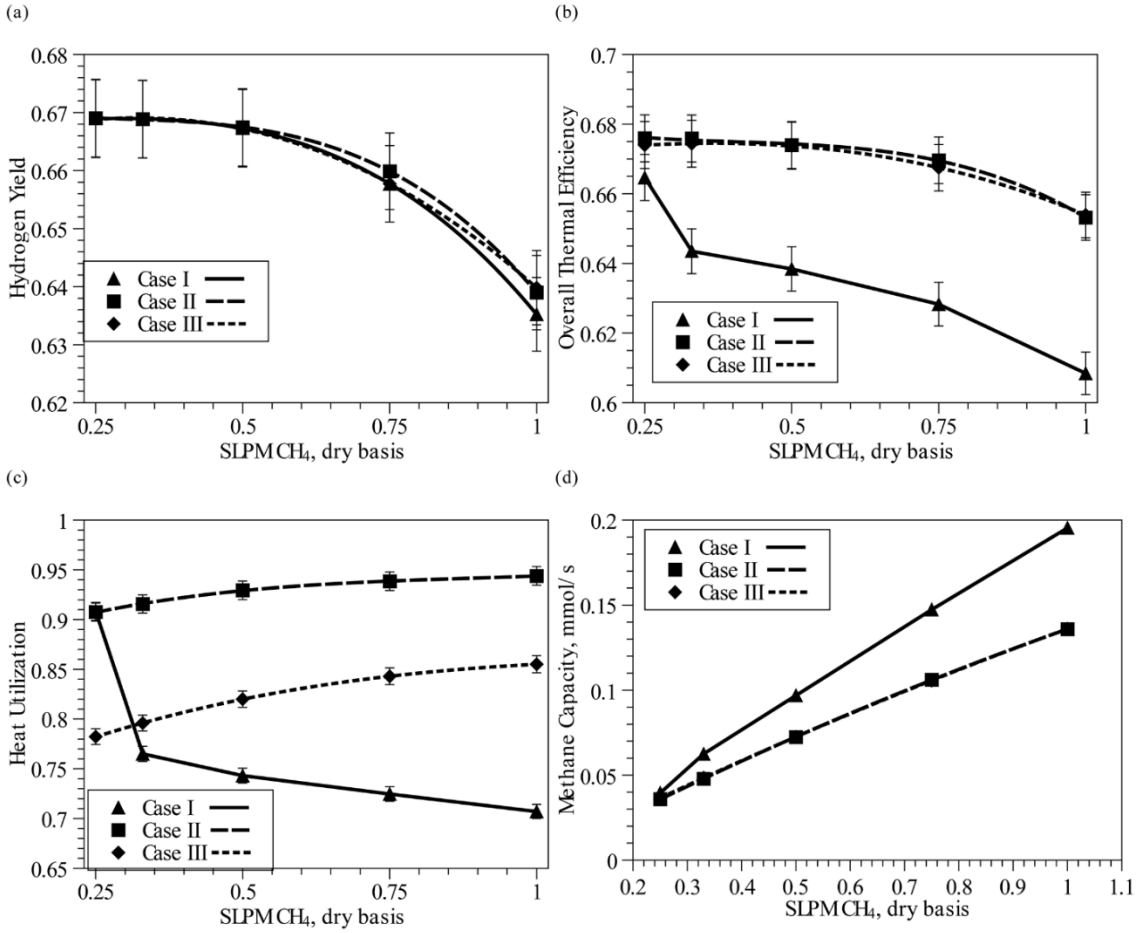

Figure 30. Simulation results for all three cases. (a) Hydrogen yield, (b) overall thermal efficiency, (c) heat utilization, (d) combustion methane capacity.

Table 14. Critical Temperature and Positions for Cases II and III.

	Case II 0.25 SLPM CH_4	Axial Position X, mm	Case III 0.25 SLPM CH_4	Axial Position X, mm
T_{high}	1164.80	0	1271.67	0
T_{low}	1023.14	254	1023.07	254
X(T=1023K)	1023.15	253	1023.15	232
	Case II 0.33 SLPM CH_4	Axial Position X, mm	Case III 0.33 SLPM CH_4	Axial Position X, mm
T_{high}	1169.72	0	1281.83	0
T_{low}	1023.08	254	1022.84	254
X(T=1023K)	1023.15	221	1023.15	223
	Case II 0.50 SLPM CH_4	Axial Position X, mm	Case III 0.50 SLPM CH_4	Axial Position X, mm
T_{high}	1173.62	0	1286.73	0
T_{low}	1022.21	245	1022.26	234
X(T=1023K)	1023.15	152	1023.15	126
	Case II 0.75 SLPM CH_4	Axial Position X, mm	Case III 0.75 SLPM CH_4	Axial Position X, mm
T_{high}	1167.50	0	1281.00	0
T_{low}	1017.56	180	1017.54	181
X(T=1023K)	1023.15	108	1023.15	109
	Case II 1.00 SLPM CH_4	Axial Position X, mm	Case III 1.00 SLPM CH_4	Axial Position X, mm
T_{high}	1160.35	6	1267.70	0
T_{low}	1007.93	192	1009.11	202
X(T=1023K)	1023.15	111	1023.15	109

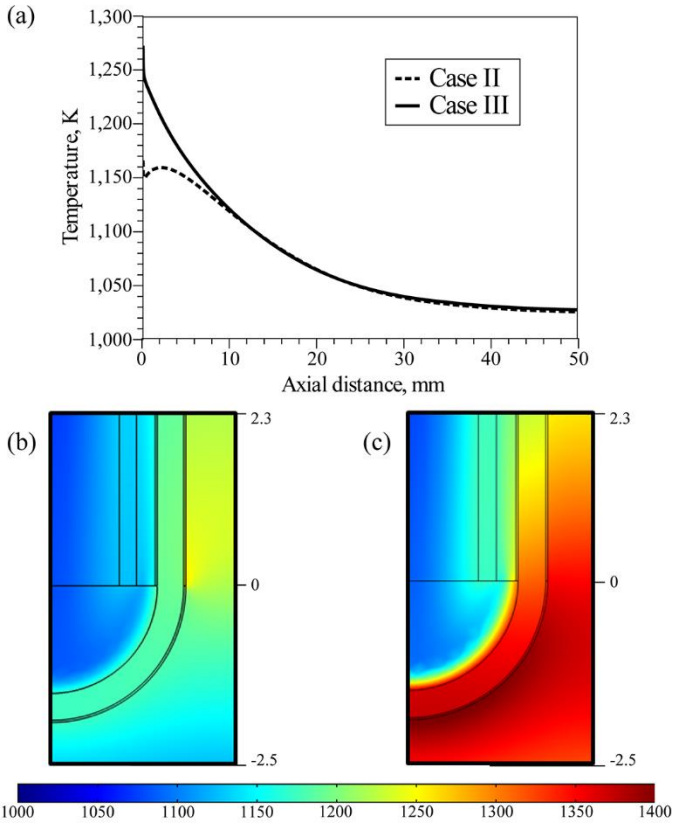

Figure 31. (a) Temperature profiles for cases II and III at MSR catalyst-fluid boundary for first 50 mm axially down the reactor for 0.25 SLPM CH_4 AMR flowrate, (b) temperature surface map of the AMR tube tip for case II, (c) temperature surface map of the AMR tube tip for case III.

Table 14 summarizes the critical temperatures and positions down the outer boundary of the reforming catalyst layer. The maximum temperature is important for considering catalyst stability and lifetime; in Case III this maximum temperature approaches 1300 K, which is ~70% of the melting point for the alumina catalyst support. In comparison, Case II maximum temperatures are consistently ~110K less than Case III. Thus, symmetric patterning of combustion and reforming zones is favorable for

minimizing catalyst degradation arising from local hot-spot formation. In contrast, Case II and Case III result in similar values for local minimum wall temperature, occurring at the reactor outlet. **Figure 31a** presents a comparison of axial wall temperature profiles between Case II and Case III at a reforming flowrate of 0.25 SLPM CH_4. For Case III, wall temperatures are >100K greater than the corresponding Case II at and near the reactor inlet zone; this difference in wall temperature between the two catalyst configurations becomes negligible by the 50mm mark (~20% of total reactor length). Complete thermal maps of the AMR corresponding to the Case II and Case III wall profiles presented in **Figure 31a** are presented in **Figure 31b** and **c**. The spike in wall temperature at the inlet for Case III arises owing to the offsetting of combustion catalyst, which allows combustion to generate heat upstream of the reforming endotherm. However, as shown in **Figure 30**, off-setting of the combustion catalyst does not result in any significant improvement in overall hydrogen yield or thermal efficiency, despite ~110K increase in local hot-spot magnitude.

5.4 Conclusions

Computational fluid-dynamic modeling of a thermally-integrated annular microreactor (AMR) coupling endothermic methane steam reforming and catalytic combustion of methane in separate process volumes, separated by a common wall (outer AMR tube wall) was investigated for three unique cases. The first case study assumed a uniform, isothermal outer AMR wall boundary, such that reforming and combustion

volumes may be modeled separately at minimum computational cost. Conduction analysis of the dividing wall using resulting axial heat duty profiles suggested deviations in wall temperature of >500^{o}C even at a thermal conductivity of 100 W/m/K; nevertheless, this first case study demonstrated a means for rapidly estimating thermal efficiency and required combustion flowrates to drive a target methane steam reforming capacity. Cases II and III simultaneously modeled both process volumes in tandem with solid-phase axial and radial heat conduction within the separating wall, assuming symmetric application of reforming and combustion coatings (case II) and off-set combustion coating (case III). Both case II and III predict significant hot-spot formation at the AMR inlet; the latter case results in >100K increase in hot spot magnitude, as compared to case II. However, this increase in hot-spot magnitude did not result in any substantial improvement in hydrogen yield or overall thermal efficiency. Thus, symmetric pairing of combustion and reforming catalytic zones is recommended for minimizing hot-spot magnitude and thus potential catalyst degradation.

5.5. Additional Hot-Spot Mitigation via Coating Inner Wall of AMR

In the previous chapter, simulations of coupled methane steam reforming and catalytic combustion of methane predicted significant exotherms at the inlet to the reforming zone for the asymmetrical AMR design (case III). This asymmetric design was implemented in an attempts to meet the abrupt heat duty required by the inlet of the steam reforming reaction zone. In at least one simulated case, hotspot temperature near the AMR tip approached 70% of the catalyst support's melting point of 1400 K, which raises significant concerns regarding long-term catalyst stability. In this chapter, simulations are used to investigate hot-spot mitigation via inclusion of addition reforming catalyst within the AMR. Specifically, the addition of reforming catalyst to the outer wall of the inner AMR tube is explored as a means of countering this entrance-zone exotherm (**Figure 32**). This catalyst addition servers as a reactive heat sink that not only reduces temperature in this region but takes advantage of the excess energy in the fluid to increase the overall performance of the reactor. The model for this study is identical to the model used for case III and the additional catalyst volume follows the same modeling used for the other reforming catalyst present.

5.5.1 Model Description

In this study, three different catalyst thicknesses and lengths are investigated in order to determine the best use of catalyst volume. The thicknesses include 30, 45, and

60 microns and the lengths include 10, 20 and 30 millimeters. **Table 15** shows the different resulting volume addition for the length and thickness combinations.

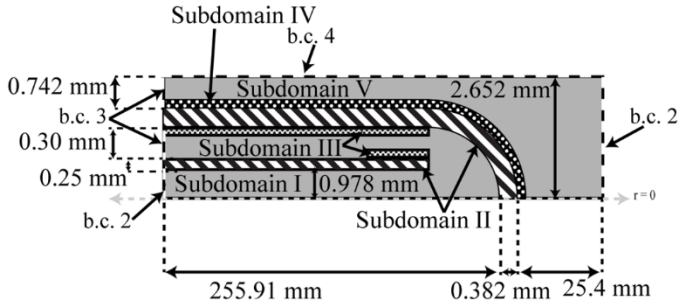

Figure 32. Schematic with dimensions, subdomains and boundary conditions marked. **Table 13** includes the description of the boundary conditions and subdomains.

Table 15. Volume addition of different thickness and length combinations with percentage volume increases.

Thickness (μm)/ Length (mm)	**30**	**45**	**60**
10	2.34 mm^3 (3.2%)	3.54 mm^3 (4.9%)	4.74 mm^3 (6.5%)
20	4.69 mm^3 (6.5%)	7.07 mm^3 (9.8%)	9.49 mm^3 (13.1%)
30	7.03 mm^3 (9.7%)	10.6 mm^3 (14.6%)	14.2 mm^3 (19.6%)

The original volume of catalyst is 72.4 mm^3, so even the largest volume addition of 14.2 mm^3 only results in less than a 20 % volume increase. The range of flowrates investigated for this study were 0.25, 0.5. 0.75, and 1.0 SLPM CH_4 AMR flow but with

combustion methane flows similar to the previous results shown for case III. To further depict the hotspot issue present in case III, **Figure 33** illustrates the maximum temperature at the reforming catalyst-wall boundary and the outer wall of the inner AMR tube (where the catalyst addition occurs in this study) for the range of flowrates studied for case III.

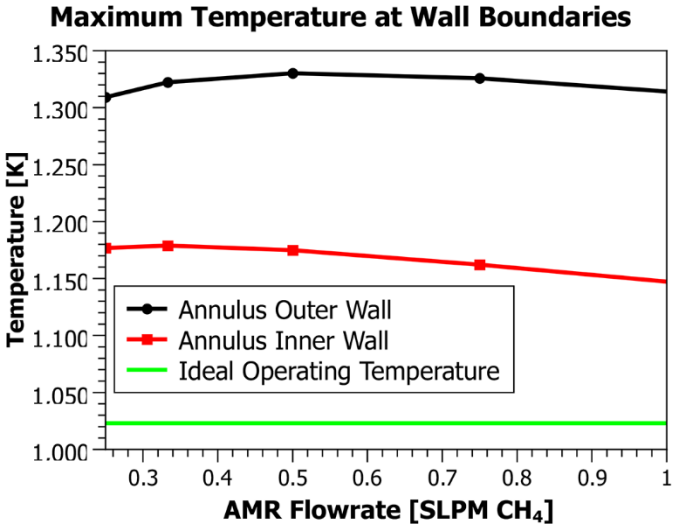

Figure 33. Maximum temperature present at reforming volume annulus wall boundaries for 0.25 to 1 SLPM CH_4 for case III.

The maximum temperature peaks at 0.5 SLPM CH_4 AMR flow rate for the outer wall and at 0.333 SLPM CH_4. However, for all flowrates the temperature is over 100 degrees higher than the ideal operating temperature of 1023.15 K at both wall boundaries. These temperature values will be revisited in the results section in order to highlight the difference that the catalyst additions made to the maximum temperatures.

In addition to the value of the maximum temperatures the location of occurrence is investigated.

5.5.2 Results

The study was conducted over multiple flow rates however all thicknesses and length combinations were not completed for all flowrates. The only flowrate that contains all thickness/length combinations is the lowest flowrate of 0.25 SLPM CH_4 AMR flow. **Table 16** shows the thickness/length combinations completed for each AMR flowrate and the corresponding hydrogen production and methane conversion for the reforming volume.

Table 16. List of simulations completed with corresponding inlet methane flows, outlet hydrogen flow and methane conversion for the reforming volume.

Width (microns)	Length (mm)	AMR flow SLPM CH_4, dry basis	$CH_{4,in}$ (CM), mol/s	$CH_{4,in}$ (MSR), mol/s	$H_{2,out}$ (MSR), mol/s	CH_4 conversion (MSR)
None	none	0.25	3.65E-05	1.86E-04	4.97E-04	0.759
30	10	0.25	3.65E-05	1.86E-04	4.97E-04	0.760
45	10	0.25	3.65E-05	1.86E-04	5.02E-04	0.767
60	10	0.25	3.65E-05	1.86E-04	5.02E-04	0.768
30	20	0.25	3.65E-05	1.85E-04	4.99E-04	0.765
45	20	0.25	3.65E-05	1.87E-04	5.03E-04	0.765
60	20	0.25	3.65E-05	1.86E-04	5.01E-04	0.767
30	30	0.25	3.65E-05	1.85E-04	4.99E-04	0.765
45	30	0.25	3.65E-05	1.89E-04	5.05E-04	0.760
60	30	0.25	3.65E-05	1.86E-04	5.01E-04	0.766
none	none	0.50	7.25E-05	3.74E-04	9.98E-04	0.757
30	10	0.50	7.25E-05	3.74E-04	1.00E-03	0.761
45	10	0.50	7.25E-05	3.74E-04	1.00E-03	0.760
60	10	0.50	7.25E-05	3.74E-04	1.00E-03	0.760
30	20	0.50	7.25E-05	3.74E-04	1.00E-03	0.761
30	30	0.50	7.25E-05	3.74E-04	9.98E-04	0.758
None	none	0.75	1.06E-04	5.63E-04	1.48E-03	0.744
30	10	0.75	1.06E-04	5.64E-04	1.48E-03	0.741
None	none	1.00	1.36E-04	7.58E-04	1.94E-03	0.719
30	10	1.00	1.36E-04	7.58E-04	1.94E-03	0.719

Table 17. Performance metrics and critical temperatures/positions.

Width (microns)	Length (mm)	AMR flow SLPM CH_4, dry basis	Overall Thermal Efficiency	H_2 Yield	Heat Utilization	z* outer wall, mm	T* outer wall, K	z* inner wall, mm	T* inner wall, K
None	none	0.25	0.671	0.669	0.784	0	1310	1.43	1177
30	10	0.25	0.671	0.669	0.783	0	1255	12.8	1065
45	10	0.25	0.677	0.675	0.744	0	1244	13.7	1058
60	10	0.25	0.677	0.675	0.780	0	1234	14.5	1054
30	20	0.25	0.675	0.673	0.780	0	1248	8.34	1041
45	20	0.25	0.676	0.673	0.775	0	1234	23.9	1033
60	20	0.25	0.677	0.674	0.789	0	1229	25.1	1033
30	30	0.25	0.676	0.674	0.785	0	1248	8.22	1040
45	30	0.25	0.673	0.669	0.789	0	1234	36.9	1025
60	30	0.25	0.675	0.673	0.789	0	1228	38.3	1029
none	none	0.50	0.671	0.667	0.820	0	1330	4.00	1175
30	10	0.50	0.674	0.670	0.827	0	1286	17.2	1096
45	10	0.50	0.674	0.670	0.829	0	1277	18.2	1090
60	10	0.50	0.673	0.670	0.831	0	1269	19.0	1087
30	20	0.50	0.674	0.670	0.827	0	1275	25.2	1066
30	30	0.50	0.671	0.668	0.821	0	1268	34.3	1045
none	none	0.75	0.665	0.658	0.843	0	1326	6.65	1162
30	10	0.75	0.663	0.656	0.848	0	1292	21.3	1103
None	none	1.00	0.650	0.639	0.855	0	1314	9.58	1147
30	10	1.00	0.650	0.639	0.860	0	1290	25.3	1102

An increase in methane conversion can be seen for all thickness/length combinations over the results for case III for all flowrates even if the difference is negligible and not seen in **Table 16** due to significant digits. The performance metrics of hydrogen yield (**Eq. 62**), overall thermal efficiency (**Eq. 63**), and combustion heat utilization (**Eq 64**) are shown in **Table 17**. Additionally, the critical positions, z*, at which the maximum temperatures at annular wall boundaries occur are shown in **Table 17**.

The critical positions for the outer annulus wall boundary all occurred at the 0 mm position at the beginning of the reforming catalyst zone (the first data point included). However, the position of the maximum temperature on the inner annulus wall boundary varied and showed a trend of increasing when compared to the uncoated case III results for each flowrate. More data points would be needed to confirm a definitive correlation with ascending position with increased catalyst volume. The maximum temperatures shown in **Table 17** are illustrated in a graphical format in **Figure 34** for the 0.25 SLPM CH_4 AMR flow data. Additionally, hydrogen yield, overall thermal efficiency, and heat utilization for the 0.25 SLPM CH_4 AMR flow data is shown in **Figure 35**.

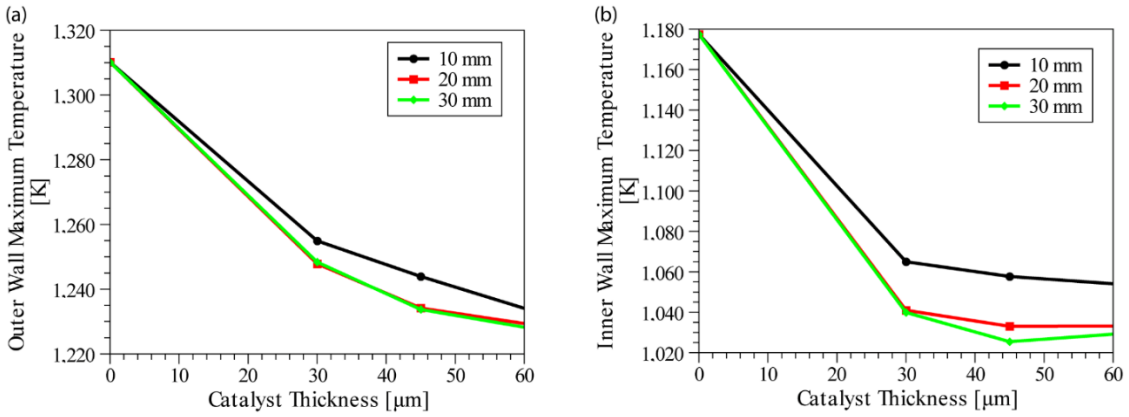

Figure 34. Maximum temperature at annular boundaries for 0.25 SLPM CH_4 AMR flowrate. (a) Outer annulus wall maximum temperature for all thickness/length combinations. (b) Inner annulus wall maximum temperature for all thickness/length combinations. The uncoated results (case III) are shown on the y-axis (0, y) at the corresponding temperature.

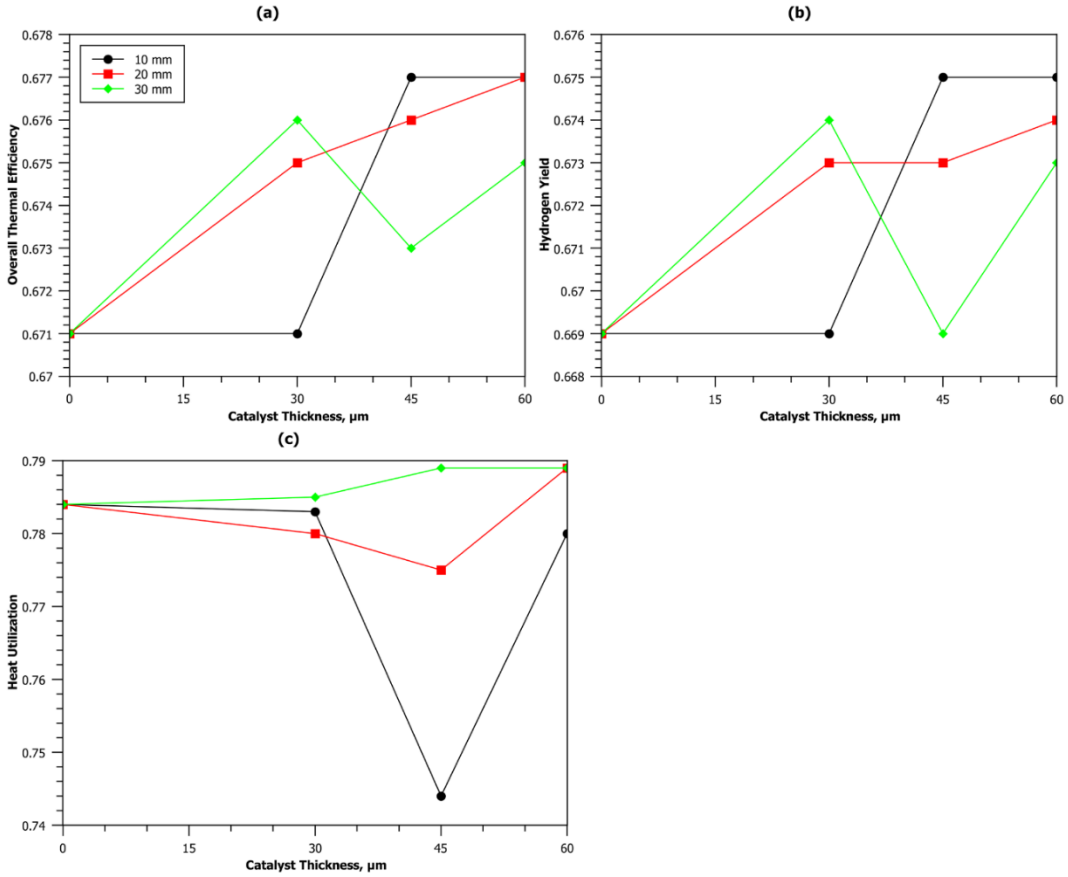

Figure 35. Performance metrics for 0.25 SLPM CH4 AMR flow for all thickness/length combinations. (a) Overall thermal efficiency, (b) Hydrogen yield, (c) heat utilization. The uncoated results (case III) are shown on the y-axis (0, y) at the corresponding metric result.

As seen in **Figure 35,** the maximum temperature for inner wall is reduced by up to 148 K and by up to 82 K for the outer wall both occurring for the 60 micron/ 30 mm addition. However, any additional coating reduced the temperature at both boundaries significantly. Although there is some temperature reduction with increasing thickness at each length the bulk of the reduction is had by the 30 micron thickness. The same is to

be said about the addition of catalyst length because most of the reduction is seen with the 10mm catalyst length. However, a side effect not depicted by the maximum temperatures are the low temperature seen in the reactor which in some cases drops below the ideal operating temperature of 1023.15 K for a short axial distance. The minimum temperature drops as catalyst addition increase, which is to be expected. When considering the three performance metrics, there are no clear trends seen among the groupings provided. However a trend may exist with more data points or for additional flow rates where methane conversion is further away from equilibrium. Without concern for trends, overall thermal efficiency and hydrogen yield are equal to or increased for all catalyst addition combinations when compared to the uncoated case (case III). Conversely, heat utilization is less for all thicknesses in the 10 and 20 mm length cases when compared to the uncoated case, but for all thicknesses in the 30 mm length had a higher heat utilization. This heat utilization increase is most probably due to the drastic drop in overall temperature surrounding the catalyst addition allowing for higher heat flux rates to occur in this area from the combustion volume.

5.5.3 Conclusions

The addition of catalyst to the inner wall of the annulus boundary are investigated including nine catalyst thickness and length combinations. Multiple flow rates are tested and compared to their uncoated equivalents (case III) on the basis of maximum temperature at annular boundaries (including positions at which these

maximums occur), hydrogen yield, overall thermal efficiency, and heat utilization. Overall the addition of catalyst to this inner annular boundary in any of the combinations tested resulted in far more stable operation. The maximum temperatures in the annular region can be decreased by more than 40 degrees for the smallest catalyst addition and up to over 80 degrees for the largest catalyst addition (for 0.25 SLPM CH_4 flow). Overall thermal efficiency and hydrogen yields are greater than or equal to the uncoated case for all combinations and most heat unitizations are less than the uncoated case except for the 30 mm length combinations which are great or equal to for the 0.25 SLPM CH_4 AMR flow data. Additionally for the 0.25 SLPM CH_4 AMR flow data, the methane conversion is higher for the reforming reaction for all catalyst addition cases. In conclusion for the 0.25 SLPM CH_4 AMR flowrate, catalyst addition mitigates the hotspot with little to no detriment to the performance metrics considered and considerably increases the catalyst stability. The other flow rates are investigated as thoroughly, restricting the conclusions that can be made without heavy speculation. Further data points would need to be collected for further trends and conclusions to be determined.

6. CONCLUSIONS

The overall goal was to produce an AMR geometry that coupled methane steam reforming and catalytic combustion of methane to produce hydrogen and/or synthesis gas efficiently and with higher power densities than the planar competitors. In Section 2, a CFD model was developed and experimentally verified, providing a computational tool for exploring the AMR design in later sections. This design was used to determine a nominal operating window bounded by 75% of maximum theoretical hydrogen yield at the operating temperature of 1023.15 K. Once this nominal operating window was established the axial heat duty profiles were extracted from the simulation results to use in subsequent modeling work. These heat duty profiles would need to be matched exactly in order to maintain isothermal operation.

The goal for Section 3 was to match the AMR heat duty profiles using catalytic combustion of methane. After testing many methane capacities it was determined that the heat duty profiles produced would not matched the shape of the AMR heat duty profiles, so overall heat duty was chosen as the new metric for successful matching. Once the corresponding methane capacities were established, the heat duty profiles were compared. Despite mismatch between the two profile sets, it was concluded that catalytic combustion of methane was a viable option in powering the AMR, however, with the understanding that temperature deviations would occur.

The goal of Section 4 was to identify if an unconventional catalyst design space exists that allows for a thicker catalyst coating to be used to trap heat in turn raising

thermal efficiency with minimal loses in catalyst efficiency. In spite of going against rules of thumb when concerning catalyst efficiency, taking advantage of the already high thermal efficiency of the AMR's micro-scale design could allow for a strategic tradeoff between costs of catalyst addition and increased reforming capacity. A 1-D study was conducted using parameters associated with the current operating conditions of the AMR. This 1-D study showed the potential for increasing the catalyst thickness, while also increasing thermal efficiency. This design space was then investigated in the 2-D space using the AMR model to corroborate the 1-D results. The results show that the ideal catalyst thickness is around twice the current catalyst coating thickness and that even as much as a three-fold increase in thickness would result in increased capacity with an acceptable loss in catalyst effectiveness.

The goal of Section 5 was to prove that actual results from pairing the models from Sections 2 and 3 were similar to the separated model results, further proving the efficacy of this design. The first objective for this section was to prove that the temperature deviations produced from this combined modeling would be less drastic than predicted by comparing the axial heat duty profiles because the models in Sections 2 and 3 do not account for the dividing wall between the two volumes. Therefore, these models do not account for the actual thermal conductivity present within the wall with a finite thermal conductivity. Another objective was to show that an asymmetric catalyst design could meet the abrupt, initial heat duty needs of the steam reforming reaction, which accounts for the highest mismatch in combustion and steam reforming heat duties. Overall, the inclusion of the dividing wall does lessen the temperature deviations axially

and shows that the predicted methane capacity needed for combustion was an over prediction. This over prediction lead to the under predicting of metrics including overall thermal efficiency and combustion heat utilization. Additionally the temperature deviations resulted in higher hydrogen yields than expected due to the shifting of equilibrium in those areas. The asymmetric design was able to over compensate for the needed heat flux in the first few mm of the reforming reaction zone resulting in hotspot formation. This hotspot formation was a catalyst stability concern and is investigated in Section 5.5.

The goal for Section 5.5 was to mitigate the hotspots produced earlier in Section 5 by the addition of reforming catalyst to the inner tube of the AMR. The objective was to show that catalyst addition to the inner tube of the AMR would maintain the performance of the asymmetrical design, proposed in Section 5.1, while reducing the magnitude and size of the hotspot produced subsequently increasing catalyst stability. This was done by introducing nine different catalyst thickness and length combinations to the outer wall of the inner tube of the AMR. The results showed that the temperature in the hotspot region could be reduced back to a reasonably stable temperature, while increasing reactor performance. Overall the catalyst addition in any of the variations tested decreased the hotspot and increased the reactor performance suggesting that catalyst addition is a way to mitigate the hotspots produced and increase catalyst stability.

NOMENCLATURE

A_i = Shomate parameter A of species i

a = actual center to center tube spacing [mm]

B_i = Shomate parameter B of species i

C = local concentration [g m^{-3}]

C_i = Shomate parameter C of species i

$C_{p,i}$ = heat capacity of species i [J mol^{-1} K^{-1}]

$C_{p,mix}$ = average heat capacity of mixture [J mol^{-1} K^{-1}]

$C_{p,cat}$ = effective heat capacity within the porous catalyst [J mol^{-1} K^{-1}]

D_i = Shomate parameter D of species i

$D_{i,j}^{eff}$ =Effective Fick's diffusivity of solute i in solvent j inside the catalyst, m^2 s^{-1}

$D_{i,j}$= Fick's diffusivity of solute i in solvent j, m^2 s^{-1}

d_p= nominal pore diameter of catalyst layer, m

$E_{A,j}$= Activation energy of reaction j, J mol^{-1}

$E_{a,j}$= Activation energy of reaction j, J mol^{-1}

E_i = Shomate parameter E of species i

F_i= molar flowrate of species i, mol s^{-1}

G = molar Gibbs free energy [J.mol^{-1}]

h = height of AMR tube [mm]

I= Identity matrix, dimensionless

k_{mix} = thermal conductivity of the mixture [W m^{-1} K^{-1}]

k_i = thermal conductivity of species i [W m^{-1} K^{-1}]

k_{cat} = effective thermal conductivity of species i inside the catalyst [W m^{-1} K^{-1}]

$K_{e,j}$ = reaction equilibrium coefficient, jth reaction

K_j= individual species adsorption coefficients [bar^{-1}]

k_j = individual reaction rate coefficients, jth reaction [mol $bar^{0.5}$ m^{-3} cat s^{-1}]

k_k = Arrhenius rate coefficients, kth reaction

L_c = estimated center to center tube spacing [mm]

M_i= Molecular weight of species i, g mol^{-1}

$\boldsymbol{n}$ = vector normal to the surface

$\boldsymbol{N}_i$ = individual species flux [mol m^{-2} s^{-1}]

P= absolute pressure, Pa

p_i= partial pressure of species i, Pa

q = total heat flow [W]

q' = line integral of radial heat flux [W m^{-1}]

R= ideal gas constant [=8.314 J mol^{-1} K^{-1} or m^3 Pa mol^{-1} K^{-1}]

R_i =catalytic reaction rate of reaction i [$mol.s^{-1}.m^3$ catalyst]

r = outer radius of AMR tube [mm]

s = sticking coefficient, dimensionless

T= Temperature, Kelvin

T^*=Lennard-Jones corrected temperature, dimensionless

t=Temperature used in Shomate equations (T/1000), [K]

u= velocity vector, [m s^{-1}]

V_{in} = uniform inlet velocity [m s^{-1}]

x_i= mole fraction of species i, dimensionless

Y_i= yield of species i, dimensionless

$[i]$=concentration of species i, [mol/m^3]

Symbol

β= Temperature exponent, dimensionless

β= Prater number, dimensionless

Γ= number of catalytic metal sites [cm^{-2}]

γ= activation energy, dimensionless

ϵ_p = porosity of catalyst layer, dimensionless

η_T= Thermal effectiveness, dimensionless

η_C= Catalyst Effectiveness Factor, dimensionless

θ_o=Oxygen Surface Coverage, dimensionless

κ = Permeability of catalyst layer, m^2

ρ = density, kg m^{-3}

τ= tortuosity of catalyst pores, dimensionless

ϕ= Thiele modulus, dimensionless

ω_i= mass fraction of species i, dimensionless

ν_i = molecular diffusion volume of species i, dimensionless

$\phi_{i,j}$ = binary pair mixture coefficient, from Wilke's mixing rule, dimensionless

Ω_μ = collision integral for predicting pure component viscosities

Ω_k = collision integral from predicting pure component thermal conductivity

ΔH_i = enthalpy of reaction for reaction i [J.mol^{-1}]

μ_i= viscosity of species i [Pa s]

μ_{mix}= viscosity of the mixture [Pa s]

σ_i= Lennard-Jones parameter, dimesionless

Subscripts

C= catalyst

Cat= catalyst

CH_4 = methane

CO= carbon monoxide

CO_2= carbon dioxide

e= reactor exit

f= fluid

H_2= hydrogen

H_2O= water

k= kinetic and shape corrected

mix= mixture basis

MSR= methane steam reforming

N_2= nitrogen

O_2= oxygen

o= reactor inlet or initial

obs= observable

WGS= water-gas-shift

Superscripts

ads= adsorption

des= desorption

*= critical

REFERENCES

1. Economides, M.J. and D.A. Wood, *The state of natural gas.* Journal of Natural Gas Science and Engineering, 2009. **1**(1–2): p. 1-13.
2. Zagoria, A. and R. Huycke, *Refinery hydrogen management - The Big Picture.* Hydrocarbon Processing, 2003. **82**(2): p. 41-46.
3. French, R.J., J. Hrdlicka, and R. Baldwin, *Mild hydrotreating of biomass pyrolysis oils to produce a suitable refinery feedstock.* Environmental Progress & Sustainable Energy, 2010. **29**(2): p. 142-150.
4. Elliott, D.C., *Historical developments in hydroprocessing bio-oils.* Energy & Fuels, 2007. **21**(3): p. 1792-1815.
5. Andrews, J. and B. Shabani, *Re-envisioning the role of hydrogen in a sustainable energy economy*. International Journal of Hydrogen Energy, 2012. **37**(2): p. 1184-1203.
6. Balat, M., *Potential importance of hydrogen as a future solution to environmental and transportation problems.* International Journal of Hydrogen Energy, 2008. **33**(15): p. 4013-4029.
7. Luk Ho, T., M. Lei Ho, Y. Ng Wai, Y. Ju, and F. Lam Koon, *Techno-economic analysis of distributed hydrogen production from natural gas.* Chinese Journal of Chemical Engineering, 2012. **20**(3): p. 489-496.
8. Holladay, J.D., J. Hu, D.L. King, and Y. Wang, *An overview of hydrogen production technologies.* Catalysis Today, 2009. **139**(4): p. 244-260.

9. Amin, A.M., E. Croiset, and W. Epling, *Review of methane catalytic cracking for hydrogen production.* International Journal of Hydrogen Energy, 2011. **36**(4): p. 2904-2935.

10. Udengaard, N.R., *Hydrogen production by steam reforming of hydrocarbons.* Abstracts of Papers of the American Chemical Society, 2004. **228**: p. U682-U682.

11. Kolios, G., B. Glockler, A. Gritsch, A. Morillo, and G. Eigenberger, *Heat-integrated reactor concepts for hydrogen production by methane steam reforming.* Fuel Cells, 2005. **5**(1): p. 52-65.

12. Barbir, F., *PEM fuel cells: theory and practice*. Pem Fuel Cells: Theory and Practice. 2005. 1-433.

13. Gencoglu, M.T. and Z. Ural, *Design of a PEM fuel cell system for residential application.* International Journal of Hydrogen Energy, 2009. **34**(12): p. 5242-5248.

14. Larminie, J., A. Dicks, and M.S. McDonald, *Fuel cell systems explained*. Vol. 2. 2003: J. Wiley Chichester, UK.

15. Jochem, E. and E. Schirrmeister, *Potential economic impact of fuel cell technologies*, in *Handbook of fuel cells*. 2010, John Wiley & Sons, Ltd. Document number: 10.1002/9780470974001.f313111. http://dx.doi.org/10.1002/9780470974001.f313111

16. Aceves, S.M., G. Petitpas, F. Espinosa-Loza, M.J. Matthews, and E. Ledesma-Orozco, *Safe, long range, inexpensive and rapidly refuelable hydrogen vehicles*

with cryogenic pressure vessels. International Journal of Hydrogen Energy, 2013. **38**(5): p. 2480-2489.

17. Furuhama, S., M. Hiruma, and Y. Enomoto, *Development of a liquid-hydrogen car*. International Journal of Hydrogen Energy, 1978. **3**(1): p. 61-81.
18. Furuhama, S. and Y. Kobayashi, *A liquid-hydrogen car with a 2-stroke direct injection engine and LH2-pump.* International Journal of Hydrogen Energy, 1982. **7**(10): p. 809-820.
19. Bowers, B.J., J.L. Zhao, M. Ruffo, R. Khan, D. Dattatraya, et al., *Onboard fuel processor for PEM fuel cell vehicles.* International Journal of Hydrogen Energy, 2007. **32**(10): p. 1437-1442.
20. Lin, Y.-M. and M.-H. Rei, *Separation of hydrogen from the gas mixture out of catalytic reformer by using supported palladium membrane.* Separation and Purification Technology, 2001. **25**(1–3): p. 87-95.
21. Ogden, J.M., *Review of small stationary reformers for hydrogen production.* . IEA/H2/TR-02/002. April, 2002. http://www.afdc. energy.gov/pdfs/31948.pdf
22. Lucredio, A.F., J.M. Assaf, and E.M. Assaf, *Reforming of a model biogas on Ni and Rh-Ni catalysts: Effect of adding La.* Fuel Processing Technology, 2012. **102**: p. 124-131.
23. Jain, I.P., *Hydrogen the fuel for 21st century.* International Journal of Hydrogen Energy, 2009. **34**(17): p. 7368-7378.
24. Richardson, I.A., J.T. Fisher, P.E. Frome, B.O. Smith, S.T. Guo, et al., *Low-cost, transportable hydrogen fueling station for early market adoption of fuel cell*

electric vehicles. International Journal of Hydrogen Energy, 2015. **40**(25): p. 8122-8127.

25. Najdi, R.A., T.G. Shaban, M.J. Mourad, and S.H. Karaki, *Hydrogen production and filling of fuel cell cars.* 2016 3rd International Conference on Advances in Computational Tools for Engineering Applications (Actea), 2016: p. 43-48.
26. Khalilpour, R. and I.A. Karimi, *Evaluation of utilization alternatives for stranded natural gas.* Energy, 2012. **40**(1): p. 317-328.
27. Lemons, R.A., *Fuel cells for transportation.* Journal of Power Sources, 1990. **29**(1): p. 251-264.
28. Lerou, J.J., A.L. Tonkovich, L. Silva, S. Perry, and J. McDaniel, *Microchannel reactor architecture enables greener processes.* Chemical Engineering Science, 2010. **65**(1): p. 380-385.
29. Thackeray, F. and G. Leckie, *Stranded gas: a vital resource.* Petroleum Economist, 2002. **69**(5): p. 10-12.
30. Max, M.D., A.H. Johnson, and W.P. Dillon, *Economic geology of natural gas hydrate*. Vol. 9. 2005: Springer Science & Business Media.
31. Sloan, E.D., *Fundamental principles and applications of natural gas hydrates.* Nature, 2003. **426**(6964): p. 353-363.
32. Elvidge, C.D., D. Ziskin, K.E. Baugh, B.T. Tuttle, T. Ghosh, et al., *A fifteen year record of global natural gas flaring derived from satellite data.* Energies, 2009. **2**(3): p. 595-622.

33. Kargbo, D.M., R.G. Wilhelm, and D.J. Campbell, *Natural gas plays in the Marcellus Shale: Challenges and potential opportunities*, 2010, ACS Publications.

34. Rotty, R.M., *First estimates of global flaring of natural gas.* Atmospheric Environment (1967), 1974. **8**(7): p. 681-686.

35. Dong, L., S. Wei, S. Tan, and H. Zhang, *GTL or LNG: which is the best way to monetize "stranded" natural gas?* Petroleum Science, 2008. **5**(4): p. 388-394.

36. Seo, J.G., M.H. Youn, Y. Bang, and I.K. Song, *Hydrogen production by steam reforming of simulated liquefied natural gas (LNG) over mesoporous nickel-M-alumina (M = Ni, Ce, La, Y, Cs, Fe, Co, and Mg) aerogel catalysts.* International Journal of Hydrogen Energy, 2011. **36**(5): p. 3505-3514.

37. Seo, J.G., M.H. Youn, D.R. Park, I. Nam, and I.K. Song, *Hydrogen production by steam reforming of liquefied natural gas (LNG) over Ni-Al2O3 catalysts prepared by a sequential precipitation method: Effect of precipitation agent.* International Journal of Hydrogen Energy, 2009. **34**(19): p. 8053-8060.

38. Thomas, S. and R.A. Dawe, *Review of ways to transport natural gas energy from countries which do not need the gas for domestic use.* Energy, 2003. **28**(14): p. 1461-1477.

39. Wood, D.A., C. Nwaoha, and B.F. Towler, *Gas-to-liquids (GTL): A review of an industry offering several routes for monetizing natural gas.* Journal of Natural Gas Science and Engineering, 2012. **9**: p. 196-208.

40. Khalilpour, R. and I. Karimi, *Evaluation of utilization alternatives for stranded natural gas.* Energy, 2012. **40**(1): p. 317-328.

41. Economides, M.J., *The economics of gas to liquids compared to liquefied natural gas.* World Energy, 2005. **8**(1): p. 136-140.

42. Holditch, S., *Turning natural gas to liquid.* Oilfield Review, 2003. **15**(3): p. 32e7.

43. Dry, M.E., *The Fischer-Tropsch process: 1950-2000.* Catalysis Today, 2002. **71**(3-4): p. 227-241.

44. Dry, M.E., *Present and future applications of the Fischer-Tropsch process.* Applied Catalysis a-General, 2004. **276**(1-2): p. 1-3.

45. Dry, M.E., *The fischer-tropsch process - commercial aspects.* Catalysis Today, 1990. **6**(3): p. 183-206.

46. Van der Laan, G.P. and A. Beenackers, *Kinetics and selectivity of the Fischer-Tropsch synthesis: A literature review.* Catalysis Reviews-Science and Engineering, 1999. **41**(3-4): p. 255-318.

47. Bakkerud, P.K., *Update on synthesis gas production for GTL.* Catalysis Today, 2005. **106**(1-4): p. 30-33.

48. Dry, M.E. and A.P. Steynberg, *Commercial FT process applications.* Fischer-Tropsch Technology, 2004. **152**: p. 406-481.

49. Wilhelm, D.J., D.R. Simbeck, A.D. Karp, and R.L. Dickerson, *Syngas production for gas-to-liquids applications: technologies, issues and outlook.* Fuel Processing Technology, 2001. **71**(1-3): p. 139-148.

50. Aasberg-Petersen, K., I. Dybkjaer, C.V. Oversen, N.C. Schjodt, J. Sehested, et al., *Natural gas to synthesis gas - Catalysts and catalytic processes.* Journal of Natural Gas Science and Engineering, 2011. **3**(2): p. 423-459.

51. Delsman, E.R., M. de Croon, G.J. Kramer, P.D. Cobden, C. Hofmann, et al., *Design and operation of a preferential oxidation microdevice for a portable fuel processor.* Chemical Engineering Science, 2004. **59**(22-23): p. 4795-4802.

52. Deshmukh, S.R., A.L.Y. Tonkovich, K.T. Jarosch, L. Schrader, S.P. Fitzgerald, et al., *Scale-up of microchannel reactors for Fischer-Tropsch synthesis.* Industrial & Engineering Chemistry Research, 2010. **49**(21): p. 10883-10888.

53. Kolb, G., *Review: Microstructured reactors for distributed and renewable production of fuels and electrical energy.* Chemical Engineering and Processing, 2013. **65**: p. 1-44.

54. *Aspen Plus*, in *Getting started customizing unit operation models.* 2012, aspen tech.

55. Bhat, S.A. and J. Sadhukhan, *Process intensification aspects for steam methane reforming: An overview.* Aiche Journal, 2009. **55**(2): p. 408-422.

56. Cremers, C., A. Pelz, U. Stimming, K. Haas-Santo, O. Goerke, et al., *Micro-structured methane steam reformer with integrated catalytic combustor.* Fuel Cells, 2007. **7**(2): p. 91-98.

57. Karakaya, M., S. Keskin, and A.K. Avci, *Parametric study of methane steam reforming to syngas in a catalytic microchannel reactor.* Applied Catalysis a-General, 2012. **411**: p. 114-122.

58. Mettler, M.S., G.D. Stefanidis, and D.G. Vlachos, *Scale-out of microreactor stacks for portable and distributed processing: Coupling of exothermic and endothermic processes for syngas production.* Industrial & Engineering Chemistry Research, 2010. **49**(21): p. 10942-10955.

59. Ramaswamy, R.C., P.A. Ramachandran, and M.P. Dudukovic, *Recuperative coupling of exothermic and endothermic reactions.* Chemical Engineering Science, 2006. **61**(2): p. 459-472.

60. Ramaswamy, R.C., P.A. Ramachandran, and M.P. Dudukovic, *Coupling exothermic and endothermic reactions in adiabatic reactors.* Chemical Engineering Science, 2008. **63**(6): p. 1654-1667.

61. Hwang, K.-R., C.-B. Lee, S.G.W. Lee, S.-K. Ryi, and J.-S. Park, *Novel micro-channel methane reformer assisted combustion reaction for hydrogen production.* International Journal of Hydrogen Energy, 2011. **36**(1): p. 473-481.

62. Wang, F., J. Zhou, and G. Wang, *Transport characteristic study of methane steam reforming coupling methane catalytic combustion for hydrogen production.* International Journal of Hydrogen Energy, 2012. **37**(17): p. 13013-13021.

63. Pattison, R.C. and M. Baldea, *A thermal-flywheel approach to distributed temperature control in microchannel reactors.* Aiche Journal, 2013. **59**(6): p. 2051-2061.

64. Pattison, R.C. and M. Baldea, *Robust autothermal microchannel reactors.* Computers & Chemical Engineering, 2015. **81**: p. 171-179.

65. Pattison, R.C., F.E. Estep, and M. Baldea, *Pseudodistributed Feed Configurations for Catalytic Plate Microchannel Reactors.* Industrial & Engineering Chemistry Research, 2014. **53**(13): p. 5028-5037.

66. Soliman, M.A., S.S.E.H El-Nashaie, A.S. Al-Ubaid, and A. Adris, *Simulation of steam reformers for methane.* Chemical Engineering Science, 1988. **43**(8): p. 1801-1806.

67. Alves, J.J. and G.P. Towler, *Analysis of Refinery Hydrogen Distribution Systems.* Industrial & Engineering Chemistry Research, 2002. **41**(23): p. 5759-5769.

68. Yang, S.-I., D.-Y. Choi, S.-C. Jang, S.-H. Kim, and D.-K. Choi, *Hydrogen separation by multi-bed pressure swing adsorption of synthesis gas.* Adsorption, 2008. **14**(4): p. 583-590.

69. Butcher, H. and B.A. Wilhite, *Enhancing catalyst effectiveness by increasing catalyst film thickness in coated-wall microreactors: Exploiting heat effects in catalytic methane steam micro-reformers.* Chemical Engineering Science, 2016. **143**: p. 47-54.

70. Honda, G.S. and B.A. Wilhite, *Influence of internal heat removal upon effectiveness, stability of an exothermic catalytic film: Implications for process intensification.* Chemical Engineering Science, 2012. **68**(1): p. 663-667.

71. Agnelli, M.E., E.N. Ponzi, and A.A. Yeramian, *Catalytic deactivation on methane steam reofrming catalyst. 2. kinetic study.* Industrial & Engineering Chemistry Research, 1987. **26**(8): p. 1707-1713.

72. Lakhapatri, S.L. and M.A. Abraham, *Deactivation due to sulfur poisoning and carbon deposition on Rh-Ni/Al2O3 catalyst during steam reforming of sulfur-doped n-hexadecane.* Applied Catalysis a-General, 2009. **364**(1-2): p. 113-121.

73. Lakhapatri, S.L. and M.A. Abraham, *Analysis of catalyst deactivation during steam reforming of jet fuel on Ni-(PdRh)/gamma-Al2O3 catalyst.* Applied Catalysis a-General, 2011. **405**(1-2): p. 149-159.

74. Moulijn, J.A., A.E. van Diepen, and F. Kapteijn, *Catalyst deactivation: is it predictable?: What to do?* Applied Catalysis A: General, 2001. **212**(1–2): p. 3-16.

75. Zhang, Y. and K.J. Smith, *Carbon formation thresholds and catalyst deactivation during CH4 decomposition on supported Co and Ni catalysts.* Catalysis Letters, 2004. **95**(1-2): p. 7-12.

76. Chen, Z., Y. Yan, and S.S.E.H. Elnashaie, *Novel circulating fast fluidized-bed membrane reformer for efficient production of hydrogen from steam reforming of methane.* Chemical Engineering Science, 2003. **58**(19): p. 4335-4349.

77. Adris, A.M., B.B. Pruden, C.J. Lim, and J.R. Grace, *On the reported attempts to radically improve the performance of the steam methane reforming reactor.* The Canadian Journal of Chemical Engineering, 1996. **74**(2): p. 177-186.

78. Hou, K.H. and R. Hughes, *The kinetics of methane steam reforming over a Ni/alpha-Al2O catalyst.* Chemical Engineering Journal, 2001. **82**(1-3): p. 311-328.

79. Luna, E.C., A.M. Becerra, and M.I. Dimitrijewits, *Methane steam reforming over rhodium promoted Ni/Al2O3 catalysts.* Reaction Kinetics and Catalysis Letters, 1999. **67**(2): p. 247-252.

80. Munster, P. and H.J. Grabke, *Kinetics of the steam refomring of methane on iron as a catalyst.* Berichte Der Bunsen-Gesellschaft-Physical Chemistry Chemical Physics, 1980. **84**(10): p. 1068-1071.

81. Alzate-Restrepo, V. and J.M. Hill, *Carbon deposition on Ni/YSZ anodes exposed to CO/H-2 feeds.* Journal of Power Sources, 2010. **195**(5): p. 1344-1351.

82. Bartholomew, C.H., *Carbon deposition in steam reforming and methanation.* Catalysis Reviews-Science and Engineering, 1982. **24**(1): p. 67-112.

83. Foo, S.Y., C.K. Cheng, T.-H. Nguyen, E.M. Kennedy, B.Z. Dlugogorski, et al., *Carbon deposition and gasification kinetics of used lanthanide-promoted Co-Ni/Al2O3 catalysts from CH4 dry reforming.* Catalysis Communications, 2012. **26**(0): p. 183-188.

84. Guo, J., H. Lou, and X. Zheng, *The deposition of coke from methane on a Ni/MgAl2O4 catalyst.* Carbon, 2007. **45**(6): p. 1314-1321.

85. Rodriguez, N.M., C.A.M. Afonso, J. Benavente, E. Rodriguez-Castellon, and J.G. Crespo, *Carbon deposition on iron-nickel alloy particles.* Applied Catalysis a-General, 1997. **148**(2): p. 265-282.

86. Trimm, D.L., *Formation and removal of coke from nickel catalyst.* Journal Name: Catal. Rev. - Sci. Eng.; (United States); Journal Volume: 16:2, 1977: p. Medium: X; Size: Pages: 155-189.

87. Xie, C., Y. Chen, Y. Lan, X. Wang, and C. Song, *Influence of sulfur on the carbon deposition in steam reforming of liquid hydrocarbons over CeO2-Al2O3 supported Ni and Rh catalysts.* Applied Catalysis a-General, 2011. **394**(1-2): p. 32-40.

88. Jensen, K.F., *Microchemical systems for discovery and development*, in *New Avenues to Efficient Chemical Synthesis: Emerging Technologies*, P.H. Seeberger and T. Blume, Editors. 2007. p. 57-76.

89. Jensen, K.F., *Microchemical systems: Status, challenges, and opportunities.* Aiche Journal, 1999. **45**(10): p. 2051-2054.

90. Mills, P.L., D.J. Quiram, and J.F. Ryley, *Microreactor technology and process miniaturization for catalytic reactions - A perspective on recent developments and emerging technologies.* Chemical Engineering Science, 2007. **62**(24): p. 6992-7010.

91. Shah, K., X. Ouyang, and R.S. Besser, *Microreaction for microfuel processing: Challenges and prospects.* Chemical Engineering & Technology, 2005. **28**(3): p. 303-313.

92. Jensen, K.F., *Microreaction engineering - is small better?* Chemical Engineering Science, 2001. **56**(2): p. 293-303.

93. Cheng, X., Z. Shi, N. Glass, L. Zhang, J. Zhang, et al., *A review of PEM hydrogen fuel cell contamination: Impacts, mechanisms, and mitigation.* Journal of Power Sources, 2007. **165**(2): p. 739-756.

94. Tonkovich, A.L.Y., B. Yang, S.T. Perry, S.P. Fizgerald, and Y. Wang, *From seconds to milliseconds to microseconds through tailored microchannel reactor design of a steam methane reformer.* Catalysis Today, 2007. **120**(1): p. 21-29.

95. Tonkovich, A.Y., S. Perry, Y. Wang, D. Qiu, T. LaPlante, et al., *Microchannel process technology for compact methane steam reforming.* Chemical Engineering Science, 2004. **59**(22-23): p. 4819-4824.

96. Ehrfeld, W., V. Hessel, and H. Löwe, *Microreactors: New Technology for Modern Chemistry 2000*, 2005, Wiley-VCH: Weinheim.

97. Arana, L.R., S.B. Schaevitz, A.J. Franz, M.A. Schmidt, and K.F. Jensen, *A microfabricated suspended-tube chemical reactor for thermally efficient fuel processing.* Journal of Microelectromechanical Systems, 2003. **12**(5): p. 600-612.

98. Kiwi-Minsker, L. and A. Renken, *Microstructured reactors for catalytic reactions.* Catalysis Today, 2005. **110**(1–2): p. 2-14.

99. Knitter, R., D. Gohring, P. Risthaus, and J. Hausselt, *Microfabrication of ceramic microreactors.* Microsystem Technologies, 2001. **7**(3): p. 85-90.

100. Murphy, D.M., A. Manerbino, M. Parker, J. Blasi, R.J. Kee, et al., *Methane steam reforming in a novel ceramic microchannel reactor.* International Journal of Hydrogen Energy, 2013. **38**(21): p. 8741-8750.

101. Tonkovich, A., D. Kuhlmann, A. Rogers, J. McDaniel, S. Fitzgerald, et al., *Microchannel technology scale-up to commercial capacity.* Chemical Engineering Research & Design, 2005. **83**(A6): p. 634-639.

102. Rebrov, E.V., S.A. Duinkerke, M. de Croon, and J.C. Schouten, *Optimization of heat transfer characteristics, flow distribution, and reaction processing for a microstructured reactor/heat-exchanger for optimal performance in platinum catalyzed ammonia oxidation.* Chemical Engineering Journal, 2003. **93**(3): p. 201-216.

103. Delsman, E.R., M. de Croon, G.J. Kramer, P.D. Cobden, C. Hofmann, et al., *Experiments and modelling of an integrated preferential oxidation-heat exchanger microdevice.* Chemical Engineering Journal, 2004. **101**(1-3): p. 123-131.

104. Mettler, M.S., G.D. Stefanidis, and D.G. Vlachos, *Enhancing stability in parallel plate microreactor stacks for syngas production.* Chemical Engineering Science, 2011. **66**(6): p. 1051-1059.

105. Stefanidis, G.D. and D.G. Vlachos, *Intensification of steam reforming of natural gas: Choosing combustible fuel and reforming catalyst.* Chemical Engineering Science, 2010. **65**(1): p. 398-404.

106. Stefanidis, G.D. and D.G. Vlachos, *High vs. low temperature reforming for hydrogen production via microtechnology.* Chemical Engineering Science, 2009. **64**(23): p. 4856-4865.

107. Ferreira-Aparicio, P., M.J. Benito, and J.L. Sanz, *New trends in reforming technologies: from Hydrogen industrial plants to multifuel microreformers.* Catalysis Reviews, 2005. **47**(4): p. 491-588.

108. Foli, K., T. Okabe, M. Olhofer, Y. Jin, and B. Sendhoff, *Optimization of micro heat exchanger: CFD, analytical approach and multi-objective evolutionary algorithms.* International Journal of Heat and Mass Transfer, 2006. **49**(5–6): p. 1090-1099.

109. Turner, K.T. and S.M. Spearing, *Modeling of direct wafer bonding: Effect of wafer bow and etch patterns.* Journal of Applied Physics, 2002. **92**(12): p. 7658-7666.

110. Ponyavin, V., Y Chen, T. Mohamed, M. Trabia, A.E. Hechanova, et al., *Design of a compact ceramic high-temperature heat exchanger and chemical decomposer for hydrogen production.* Heat Transfer Engineering, 2012. **33**(10): p. 853-870.

111. Penniall, C., C. Williamson, and A. Marshall, *Comparison of the performance of washcoating variations for fisher-tropsch synthesis in a microchannel reactor.* 2012.

112. Wilhite, B.A., L. Breziner, J. Mettes, and P. Bossard, *Radial microchannel reactors (RMRs) for efficient and compact steam reforming of methane: Experimental demonstration and design simulations.* Energy & Fuels, 2013.

113. Besser, R.S., *Thermal integration of a cylindrically symmetric methanol fuel processor for portable fuel cell power.* International Journal of Hydrogen Energy, 2011. **36**(1): p. 276-283.

114. Bossard, P.R. and J. Mettes, *Integrated micro-channel reformer and purifier for extracting ultra-pure hydrogen gas from a hydrocarbon fuel*, 2014, Google Patents.

115. Bossard, P.R., *Multiple tube micro-channel steam reformer and method*, 2012, Google Patents.

116. Bossard, P.R. and J. Mettes, *System and method for processing fuel for use by a fuel cell using a micro-channel catalytic hydrogen separator*, 2010, Google Patents.

117. Bossard, P.R., *System and method for processing natural gas*, 2012, Google Patents.

118. Bossard, P.R., *Micro-channel steam reformer and system for extracting ultra-pure hydrogen gas from a hydrocarbon fuel*, 2012, Google Patents.

119. Bossard, P.R., *System and method for separating hydrogen gas from a hydrocarbon using a hydrogen separator assisted by a steam sweep*, 2010, Google Patents.

120. Davis, M., G. Fairweather, and J. Yamanis, *Annular bed reactor-Methanation of carbon-dioxide.* Canadian Journal of Chemical Engineering, 1981. **59**(4): p. 497-500.

121. Davis, M.E. and J. Yamanis, *Analysis of annular bed reactor for methanation of Carbon-Monoxide.* Aiche Journal, 1982. **28**(2): p. 266-273.

122. Hirschfelder, J.O.C., C.F.; Bird, R.B., *Molecular theory of gases and liquids*. 2nd ed. 1964, New York: Wiley.

123. Neufeld, P.D., R.A. Aziz, and A.R. Janzen, *Emperical equations to calculate 16 of the tranport collision integrals-Omega(L,S) for Lennard-Jones (12-6) potential*. Journal of Chemical Physics, 1972. **57**(3): p. 1100-&.

124. Mason, E.A. and S.C. Saxena, *Approximate formula for the thermal conductiviy of gas mixtures.* Physics of Fluids, 1958. **1**(5): p. 361-369.

125. Fuller, E.N., Schettle.Pd, and J.C. Giddings, *A new method for prediction of binary gas-phase diffusion coefficient.* Industrial and Engineering Chemistry, 1966. **58**(5): p. 19-&.

126. Butt, J.B., *Thermal conductivy of porous catalysts.*. Aiche Journal, 1965. **11**(1): p. 106-&.

127. Xu, J.G. and G.F. Froment, Methane steam reforming, methanation and water-gas shift. 1. Intrinsic kinetics. Aiche Journal, 1989. **35**(1): p. 88-96.

128. Vaccaro, S., G. Ferrazzano, and P. Ciambelli, Proceedings of COMSOL User Conference, Milan Italy, 2006.

129. COMSOL. *Multiphysics refrence guide 4.2a*, 2012.

130. Zhai, X.L., S. Ding, Z. Liu, Y. Jin, and Y. Cheng, *Catalytic performance of Ni catalysts for steam reforming of methane at high space velocity.* International Journal of Hydrogen Energy, 2011. **36**(1): p. 482-489.

131. Takehira, K., T. Shishido, P. Wang, T. Kosaka, and K. Takaki, *Steam reforming of CH4 over supported Ni catalysts prepared from a Mg-Al hydrotalcite-like anionic clay.* Physical Chemistry Chemical Physics, 2003. **5**(17): p. 3801-3810.

132. Probstein, R.F.H., R.E., *Synthetic fuels*. 1982, Mineola, New York: Dover Publications.

133. Chibane, L.a.D., B. , *Methane steam reforming reaction behaviour in a packed bed membrane reactor*. International Journal of Chemical Engineering and Applications, 2011. **2**(3): p. 147-156.

134. Damodharan, S., B.V.R. Kuncharam, and B.A. Wilhite, *Design of cartridge-based ceramic heat-exchanger microchannel reformers for process intensification: Experiments and simulations.* Energy & Fuels, 2013. **27**(8): p. 4411-4422.

135. Deshmukh, S.R. and D.G. Vlachos, *A reduced mechanism for methane and one-step rate expressions for fuel-lean catalytic combustion of small alkanes on noble metals.* Combustion and Flame, 2007. **149**(4): p. 366-383.

136. Butcher, H., C.J.E. Quenzel, L. Breziner, J. Mettes, B..A. Wilhite, et al., *Design of an annular microchannel reactor (AMR) for hydrogen and/or syngas production via methane steam reforming.* International Journal of Hydrogen Energy, 2014. **39**(31): p. 18046-18057.

137. Zhai, X., Y. Cheng, Z. Zhang, Y. Jin, and Y. Cheng, *Steam reforming of methane over Ni catalyst in micro-channel reactor.* International Journal of Hydrogen Energy, 2011. **36**(12): p. 7105-7113.

138. Zhai, X., S. Ding, Z. Liu, Y. Jin, and Y. Cheng, *Catalytic performance of Ni catalysts for steam reforming of methane at high space velocity.* International Journal of Hydrogen Energy, 2011. **36**(1): p. 482-489.

139. Zanfir, M., M. Baldea, and P. Daoutidis, *Optimizing the catalyst distribution for countercurrent methane steam reforming in plate reactors.* Aiche Journal, 2011. **57**(9): p. 2518-2528.

140. Jeon, S.W., W.J. Yoon, C. Baek, and Y. Kim, *Minimization of hot spot in a microchannel reactor for steam reforming of methane with the stripe combustion catalyst layer.* International Journal of Hydrogen Energy, 2013. **38**(32): p. 13982-13990.

141. Thiele, E.W., *Relation between Catalytic Activity and Size of Particle.* Industrial & Engineering Chemistry, 1939. **31**(7): p. 916-920.

142. Aris, R., *On shape factors for irregular particles—I: The steady state problem. Diffusion and reaction.* Chemical Engineering Science, 1957. **6**(6): p. 262-268.

143. Aris, R., *Elementary Chemical Reaction Analysis*. 1969.

144. Carberry, J.J. and A.A. Kulkarni, *Noniosthermal catalytic effectiveness for monolith supported catalysts.* Journal of Catalysis, 1973. **31**(1): p. 41-50.

145. Roberts, G.W. and C.N. Satterfield, *Effectiveness factor for porous catalysts. Langmuir-Hinshelwood kinetic expressions.* Industrial & Engineering Chemistry Fundamentals, 1965. **4**(3): p. 288-293.

146. Carberry, J.J., *The catalytic effectiveness factor under nonisothermal conditions.* AIChE Journal, 1961. **7**(2): p. 350-351.

147. Carberry, J.J., *The micro-macro effectiveness factor for the reversible catalytic reaction.* AIChE Journal, 1962. **8**(4): p. 557-558.

148. Cybulski, A. and J.A. Moulijn, *Monoliths in heterogeneous catalysis.* Reviews-Science and Engineering, 1994. **36**(2): p. 179-270.

149. Bobrova, I.I., V.V. Chesnokov, N.N. Bobrov, V.I. Zaikovskii, and V.N. Parmon, *New data on gas-phase radical reactions in the steam reforming of methane in the presence of catalysts: I. Nickel catalysts.* Kinetics and Catalysis, 2000. **41**(1): p. 19-24.

150. Butcher, H., , C.J.E. Quenzel, L. Breziner, J. Mettes, B..A. Wilhite, et al., *Design of an annular microchannel reactor (AMR) for hydrogen and/or syngas production via methane steam reforming.* International Journal of Hydrogen Energy, 2014. **39**(31): p. 18046-18057.

151. Aris, R., *On shape factors for irregular particles. 1. The steady state problem - Diffusion and reaction.* Chemical Engineering Science, 1957. **6**(6): p. 262-268.

152. Harris, R.A. *Commercializing and deploying microchannel FT reactors for smaller scale GTL facilities*. in *AIChE Process Development Symposium*. 2015. Houston, TX.

153. Westbrook, C.K. and F.L. Dryer, *Simplified reaction mechanisms for the oxidation of hydrocarbon fuels in flames*. 1981, Berkeley, Calif.: Lawrence Livermore Lab.